The Dissertation Committee for Conrad Yuan Yuen Lee
certifies that this is the approved version of the following dissertation:

Direct Numerical Simulation of Microjets for Turbulent Boundary Layer Control

Committee:

David B. Goldstein, Supervisor

David S. Dolling

Graham F. Carey

Kenneth S. Ball

Ronald L. Panton

Direct Numerical Simulation of Microjets for Turbulent Boundary Layer Control

by

Conrad Yuan Yuen Lee, B.S., M.S.

DISSERTATION

Presented to the Faculty of the Graduate School of
The University of Texas at Austin
in Partial Fulfillment
of the Requirements
for the Degree of

DOCTOR OF PHILOSOPHY

THE UNIVERSITY OF TEXAS AT AUSTIN
August 2004

Dedicated to my parents.

Acknowledgments

I would like to thank Dr. David B. Goldstein for his many years of support, guidance and patience during this project. I would also like to thank Dr. David Dolling, Dr. Graham Carey, Dr. Kenneth Ball and Dr. Ronald Panton for reviewing my work and this manuscript and providing important commentary and suggestions. Funding for this project was provided by the Air Force Office of Scientific Research (AFOSR) under grant F49620-98-1-0027 while the Texas Advanced Computing Center (TACC) provided essential computational resources and storage space for the considerable volumes of data I generated.

In addition, during my time at The University of Texas at Austin, I made the acquaintance of many people: colleagues, co-workers and friends whose help were much appreciated. Robert McLay, William Barth, Benjamin Kirk and, more recently, John Peterson provided much needed hardware and technical support through the CFD Lab. Additional technical support came from Scott Messec, Reuben Reyes and other past and present ASE/EM LRC staff. I would like to acknowledge my CFP Lab co-workers, past and present for their contributions, technical or not: Victor Austin, Tai-Chang Tuan, Roberto Roveda, Sidra Silton, Donny Young, Ju Zhang, Chris Moore, Benedicte Largignon, Kevin Marr and L.C. Colmenero. Last, but not least, I would like to thank some of my friends in the ASE/EM department and beyond for their support and occasional insightful discussion: Vincent Liu, John Dunn, Francis França, Jeff Mach, Elizabeth Quintanilla, Michael Tsurikov, Pablo Bueno, Isaac Boxx, Yuto Shinagawa, Romil Doctor, Eduardo Gildin and family, Douglas Migliano and family, and past and present members of TAC, UTKA and AKD.

I must, however, reserve the greatest acknowledgment to the members of my family: my brother Charles, my sister Corina and her family and above all, my parents. Their actions and undying support have shown me, time over time, the true definition of family and the unbreakable bond that exists between its members. It is a fact that I would never have reached this point without their help and this work is therefore dedicated to them.

Direct Numerical Simulation of Microjets for Turbulent Boundary Layer Control

Publication No. __________________

Conrad Yuan Yuen Lee, Ph.D.
The University of Texas at Austin, 2004

Supervisor: David B. Goldstein

A direct numerical simulation approach is used to simulate an array of MEMS slot jets in a turbulent boundary layer for the purposes of flow control. Initial studies were used to first ascertain the correctness of the model and give insight into the performance characteristics of the devices. To this end, a flow and geometric parameter study was conducted on a 2-D simulation of the devices and the results used in the design of 3-D devices. Then, once the performance characteristics of the 3-D devices were determined, a series of parametric studies were conducted involving quasi-steady, periodic and single pulses into a turbulent boundary layer. Results indicate that low *Re* devices can substantially affect the flow but the arbitrary actuation tended to introduce new disturbances in the flow. Hybrid methods involving passive surface texture elements and active devices were briefly examined in an attempt to extract some form of useful flow control from the actuators but the results were still insufficient. Instead, a real-time, adaptive feedback method was selected to calibrate the strength of the actuators. The feedback method was first tested by itself to verify that the numerical approach used here was capable of implementing such control. The feedback method was then modified and used with a single, isolated slot. Subsequent simulations increased the number of slots to form a row of actuators and eventually actuator arrays. Results showed that an actively-controlled actuator array provided a small turbulent drag decrease despite having only a small impact on the turbulence levels in the flow. This result suggested a different mechanism of drag reduction from the original feedback method based on the presence of cavities which are seen as low-shear stress regions by the mean flow.

Table of Contents

List of Tables

List of Figures

Chapter 1

Introduction

Over the years, much attention has been focused on the active control of the boundary layer to reduce both laminar and turbulent viscous drag. Some of the more successful devices capable of manipulating the boundary layer have required, for the most part, auxiliary power sources and substantial modifications to the structure of aerodynamic surfaces. For example, as mentioned in Braslow [1], laminar flow control (LFC) through wall suction and enhanced natural laminar flow (NLF) through surface shaping were combined in a hybrid laminar flow control (HLFC) method. These devices were shown to reduce drag in several aircraft under different flight regimes in tests throughout the 1980's and 1990's by stabilizing the laminar boundary layer and delaying transition. While the general characteristics of laminar and turbulent boundary layers are well known, there are differing theories on the type of devices and the actual physical mechanism needed to achieve flow control. In addition, as pointed out by Coustols and Savill [2], the Reynolds number on aircraft at cruise conditions is such that eventual transition into turbulent flow is unavoidable. Moreover, aircraft manufacturers in recent years have been focusing on the design of larger, high-capacity civil transport aircraft. Such aircraft potentially reduce operating costs per passenger per mile based on their size alone but also present a much increased area over aerodynamic surfaces and the fuselage which would be subjected to turbulent drag. With viscous drag accounting for as much as 48% of the total drag in a civil transport aircraft [2], turbulent flow control and turbulent drag reduction could potentially produce further substantial savings in the operating costs of such aircraft. Although this particular example focused solely on aircraft, the same argument can be made for a variety of systems such as ship/submarine hulls, high-speed trains and pipelines, all of which would benefit from reductions in turbulent drag.

To be of use, flow control and turbulent drag reduction systems must offer clear gains over the alternative un-actuated surfaces. At the most basic level, the energy needed to operate a drag reduction device should not exceed the savings obtained through a drag reduction. The devices should also require minimal structural changes to the mounting surface. Lastly, the design of the devices should be flexible enough so that they can be easily incorporated into multiple applications. Fortunately, advances in micro-machining techniques over the past decade have allowed the construction and testing of several low power Micro Electronic Mechanical Systems (MEMS) for a multitude of applications. In the case of drag reduction, arrays of synthetic jets or flaps may be applied as a “smart skin” on a surface to exert flow control. Several numerical studies have been performed that indicate MEMS can exert useful flow control. However, true adaptive control of an un-separated flow with a global reduction in viscous drag, let alone a net energy savings, has yet to be concretely achieved with such devices.

Parallel to the development of MEMS, improvements in computational power and techniques made it possible to directly simulate turbulent flow within modestly complex boundary geometries using the full Navier-Stokes equations. Such direct numerical simulations have several advantages over experimental work such as the ease with which some parametric studies can be performed, the availability of all flow properties and the pre-existing large database of flows already studied for comparison and validation purposes. Theoretical flow control models involving dampening or filtering of certain flow features have been tested with direct numerical simulations (DNS) and shown to be capable of achieving net drag reductions. However, there are substantial difficulties in translating such control schemes into practical devices. Physical devices must, of course, be manufactured and their performance characterized before any experiment in flow control can be attempted. To facilitate the design of MEMS devices, reasonably realistic *faux-similes* of the internal geometry and driving mechanisms of MEMS devices can be readily modeled in a DNS with immersed or moving boundary techniques. These techniques, incorporated in the DNS of turbulent flow, provide a valuable tool to study the physics of device interaction with the finest structures of a turbulent flow. Data gathered from such simulations would be valuable in the design of practical devices.

In order to better understand the issues relating to the use of MEMS for flow control in a turbulent boundary layer, a brief review of the structure of a turbulent boundary layer and possible control techniques will first be given. It will be followed by a review of studies regarding the physics of a specific MEMS device of present interest – a synthetic slot jet. A summary will then be given of several experiments in which MEMS were used to generate modest levels of flow control. Lastly, the present work will be summarized with a outline of the series of studies conducted towards the developing discrete actuators capable of achieving useful flow control.

1.1 The Physics of Turbulent Boundary Layers

Turbulent boundary layer contains random fluctuations that are the result of intermittent flow features that, when taken altogether, define a turbulent boundary layer. As mentioned in Coustols and Savill [2], some of these features are:

– Low-speed streaks near the wall ($y^+ < 10$);

– Ejections of low-speed fluid away from the wall and sweeps of high-speed fluid towards the wall;

– Near-wall vortical structures of varying type and scale;

– Strong internal shear layers in the inner region ($y^+ < 80$);

– Large scale motions in the outer layer.

The above features are believed to form self-sustaining mechanisms for turbulence generation, although theories differ on the actual process relating turbulent structures to turbulence production. However, as noted in Coustols and Savill [2], near-wall vortical structures, ejection/sweep events and strong internal shear layers are also agreed on as the more energetic features of a boundary layer and, consequently, may play a larger role in turbulence production. Accordingly, Kline [3] describes a possible theory for turbulence production focusing on the near-wall vortical structures and the quasi-periodic fashion in which they arise, evolve and decay. Smith and Walker [4] noted that, within $y^+ < 100$, these vortices form a self-sustaining mechanism in which vortical structures continuously break down and create more structures through interactions with the surface. Central to this self-sustaining chain are the streamwise vortices that often originate from the formation and stretching of symmetric and asymmetric horseshoe vortices. Streamwise vortices usually have core diameters of 10 to 40 wall units, lengths of O(100) wall units and cores 10 to 50 wall units above the wall. Counter-rotating vortex pairs, roughly 50 wall units apart, lead to the formation of low speed streaks about 10 to 40 wall units wide and O(1000) wall units long. Low-speed streaks have been observed to gradually rise from the wall and oscillate before breaking down – a mechanism considered by Coustols and Savill [2] as the starting point of the breakdown and eruption of the wall layer. Experimental studies such as Praturi and Brodkey [5] indicate that energetic wall ejections and eruptions provide the bulk of total turbulence production in a boundary layer, a result confirmed numerically by Kim *et al.* [6]. Further experimental work by Alfredsson and Johansson [7] indicated that ejections are responsible for about 80% of the total shear stress.

Numerical studies by Jiménez and Pinelli [8] sought to better establish the relationship between wall streaks and vortical elements in the boundary layer. By applying dampening filters of different levels and at different heights, Jiménez and Pinelli [8] were able to isolate the interaction of particular flow structures. Results showed that the near-wall turbulence cycle could be reduced to a minimal unit restricted to the region $20 < y^+ < 60$. Detailed mathematical analysis by Waleffe [9] indicated that, outside of this range ($20 < y^+ < 60$), the cycle tended to be disrupted by viscosity near the wall and secondary instabilities in the outer flow. However, Jiménez and Pinelli [8] noted that, within this region, streamwise or quasi-streamwise vortices produced streaks by advecting the mean velocity gradient. Pairs of low and high-speed streaks, in turn, de-stabilized the flow and led to the formation of further vortical structures. Close examination of the streak structure by Jiménez and Simens [10] showed that streaks ejected primarily asymmetric hairpin vortices which went through their own evolution cycle. Bursting events then occurred from the interaction of the hairpin vortices as they rose above the top of the streaks. The self-sustaining capability of the streak cycle meant that other flow mechanisms, such as incoming perturbations from the outer flow and secondary vorticity generation at the wall were contributing but not dominant factors necessary for the maintenance of the cycle. This was confirmed in Jiménez and Pinelli [8] by applying a dampening filter to the source term of the vorticity transport equation. The resulting suppression of the primary vortices responsible for streak formation did not eliminate the streak cycle. Rather the streak cycle became intermittent sugesting that the secondary mechanisms could provide a sufficient amount of activity to maintain turbulent flow.

1.2 Control Methods of Turbulent Boundary Layers

In order to achieve flow control and reduce turbulent shear stress, the turbulence production cycle described in the previous section must be disrupted at some point by passive or active devices. As pointed out in Gad-El-Hak's [11] extensive review of flow control issues, the wall would be a natural location at which control devices could be mounted. In this case, streaks and streamwise vortices made ideal target structures due to their proximity to the surface and the direct role both played in increased shear stress. For example: surface shaping, coating or transpiration were mentioned by Gad-El-Hak [11] as feasible wall-mounted control mechanism.

In the case of transpiration, Gad-El-Hak [11] noted a stabilizing effect of suction on low-speed streaks caused by the removal of inflection points in the streamwise velocity profile. Experimental studies by Antonia *et al.* [12] indicated that small wall suction coefficients of $C_q = 0.003$ were sufficient to stabilize the flow and introduce substantial changes in some turbulent properties. This suction rate was one order of magnitude smaller than needed for flow re-laminarization ($C_q \approx 0.01$). Antonia *et al.* [12] also measured reductions of 48% and 32% in peak streamwise and spanwise velocity fluctuations, respectively. Near the wall, the frequency of burst and sweeps events was further reduced by a factor of 2 with associated reductions in Reynolds shear stress. Using the same suction coefficient, Elena [13] measured a decrease in the frequency of boundary layer events as well as increases in the dissipation length scale and integral scales. Similar results were observed in numerical simulations by Kim *et al.* [14] with a substantial reduction in the number of vortical structures downstream of a spanwise slot subjected to uniform suction. In the case of fluid injection, wall-normal blowing under high-speed streaks can have a direct effect in reducing local skin friction by moving high shear stress regions and their associated flow structures away from the surface. This was observed by Kim *et al.* [14] who also noted that vortical structures lifted over the blowing zone tended to increase in strength further downstream. This suggested that local reductions in shear stress would be more likely to be followed by a local increase downstream.

Alternatively, experiments by Bradshaw and Pontikos [15] indicated a substantial reduction in turbulent activity and shear stress on a near-infinite swept wing subjected to *spanwise* blowing. It was believed that the addition of spanwise blowing induced a spanwise gradient of the spanwise shear that re-aligned larger eddies and shear stress vectors. However, the reduction in shear stress was not only a mere consequence of the re-aligned flow projecting a smaller fraction of shear stress in the streamwise direction. Numerical studies by Moin *et al.* [16] on a channel flow subjected to an oscillating transverse pressure gradient confirmed the results of Bradshaw and Pontikos [15] and also reported a drop in turbulent kinetic energy caused by a combination of decreased turbulence production and increased turbulent dissipation. These results suggested that devices that induced spanwise oscillations in the flow could be used for drag reduction purposes. Experiments by Laadhari *et al.* [17] on an oscillating wall indicated reductions in velocity fluctuations and Reynolds stress throughout a range of oscillation parameters. Laadhari *et al.* [17] performed several experiments at a fixed wave number of $\lambda_z = 160l^*$ and periods ranging from $60T^*$ to $300T^*$ and measured a peak reduction of 50% in Reynolds stress at $T^* = 100$. Further extensive work on oscillating plates conducted by Trujillo [18] linked the reductions in Reynolds stress to increased uniformity on the near-wall fluid brought about by the oscillating motion. As the wall moved, it convected streamwise vortices along with it and broke the streak pattern, stabilizing the flow and reducing the frequency of burst and sweep events. Furthermore, the oscillating motion prevented vortices from re-asserting their influence on the wall and consequently prevented the streak patterns from re-forming after the initial break-up. Trujillo [18] determined that drag decreases were directly proportional to decreasing period of oscillation and increasing wave number. Peak drag reductions of 40% were obtained for a period of $67T^*$ and wave number of $\lambda_z = 360l^*$. However, Trujillo [18] also determined that the power required to oscillate the plate at those levels far exceeded the amount saved through drag reduction. The break-even point, at which the power input to the system matched the power savings corresponded to a 18% drag reduction.

Similar to spanwise oscillations but on a more basic level, Du and Karniadakis [19] made use of a numerical simulation to introduce transverse traveling waves close to the wall. For a fixed wavenumber of $\lambda_z = 840^*$, a drag increase was measured with a period of actuation of $T^* = 100$. Reducing the period to $T^* = 50$ resulted in a substantial drag decrease of 30%. Visualization of the near wall flow structure at this period of oscillation showed that the traveling wave greatly reduced the number of streaks and hairpin vortices present. However, further reducing the period to $T^* = 25$ resulted in a drag decrease of 15%, less than at $T^* = 50$. These results were in contrast with the spanwise wall oscillation experiments of Trujillo [18], which indicated increased drag reductions with decreasing period of oscillation. Du and Karniadakis [19] attributed the different results to the fact that a traveling wave affected the flow in a different manner than wall oscillation. Wall oscillation broke down the streak structure through increased spanwise mixing while traveling waves acted on vortical structures to suppress streak formation. Moreover, Du and Karniadakis [19] determined that the efficiency of the traveling wave was inversely proportional to its amplitude. Waves of period $T^* = 100$ were eventually able to produce drag decreases once the amplitude was halved. Although useful, transverse waves were dependent on an actuator capable of inducing such forces on the flow. While this constraint might limit its applicability, traveling waves could still be used in conductive mediums, like saltwater under forcing by electro-magnetic fields. Du and Karniadakis [19] conducted limited experiments with actuator arrays consisting of magnet and electrode couples on a plate in salt water. When activated, each actuator created a 3-D Lorentz force. Proper modulation of each actuator over the entire array could mimic transverse traveling waves across the plate. Minor drag reductions were obtained for actuators covering 10% of the surface area of the plate. In addition, the ratio of power saved by drag reduction to power delivered to the actuators was estimated at 5 : 1 suggesting that this approach still has potential. Alternatively, Rediniotis *et al.* [20] performed simulations of piezo-ceramic actuators mounted underneath a flexible skin. Results showed that when pulsed in the proper order, the actuators deformed and undulated the skin - forming a traveling wave in a non-conductive medium.

A separate but equally important issue concerned the location and density of sensors and how their data could be used to guide the actuators. Numerical experiments by Lee *et al.* [21] determined that data from 7 shear stress sensors could be used to predict the velocity at a certain point in the flow. Alternatively, data from pressure sensors could also be used to control actuation as shown by Lee *et al.* [22]. Experiments by Rathnasingham and Breuer [23] demonstrated the potential of an adaptive control system involving a single actuator with 3 upstream shear stress sensors and one downstream feedback sensor. Further work by Amonlirdviman and Breuer [24] sought to determine the optimum number and placement of sensors so that the Reynolds stress and fluctuations in streamwise velocity could be accurately predicted at another location. Using the spanwise gradient of the spanwise shear as the sensed variable, Amonlirdviman and Breuer [24] determined that a pair of sensors yielded best results when mounted closest to the point of interest with a spanwise separation of $100l^*$. This suggested that optimum sensor placement would be at the same streamwise locations and in between actuators. This result was also in agreement with statements by Gad-El-Hak [11], who noted that spanwise sensor/actuator placement should be at most equivalent to the average streak spacing of $100l^*$. However, whether devices with sensor/actuator co-location can be manufactured is another issue that needs to be addressed in the experimental side.

The above issues of target structures, sensor placement and control method were all addressed in a numerical simulation by Choi *et al.* [25] to form a feedback-controlled mechanism for flow control. The control scheme made use of internal flow field data to apply blowing or suction on the channel walls of magnitude opposite to the normal or spanwise components of velocity at a detection plane away from the walls. Thus, this control scheme was akin to a virtual "smart skin" uniformly and densely covered with actuators. With this method, an overall drag reduction of 25% was obtained on each wall. The drag reduction remained at a substantial 20% when control was applied to suppress only the strongest events, which corresponded to 25% of the total surface area being controlled at any instant. When the *VOC* method was applied to only one of the walls of the channel, the same drag reduction levels were measured on the one active surface. Close examination of flow structures indicated the presence of secondary vorticity drawn off the wall by pairs of streamwise vortices near the surface. Control in the form of a normal velocity applied at the wall eliminated the lifting of secondary vorticity and tended to separate streamwise vortex pairs producing a stabilizing effect. In contrast, when a spanwise velocity was applied at the wall, stronger secondary vortices would lift the streamwise vortices away from the wall and into the interior of the channel. The net effect for both control methods was a reduction of sweep events and a direct reduction in shear stress. An alternative sensing method was also tested using flow variables at the wall only. Although common flow variables such as pressure and the shear stress were tested, a more efficient quantity derived from the Taylor expansion of the normal component of velocity was used. This quantity, based on the spanwise gradient of the spanwise shear was found to correlate well to large values of the normal velocity above the wall. Using this wall sensor, a drag reduction of only 6% was obtained.

Numerical simulations were also conducted by Koumoutsakos *et al.* [26] with emphasis on the wall normal blowing/suction and sensor plane placement. As tested by Choi *et al.* [25], this opposition control method yielded a drag reduction with sensing at heights of $10l^*$ or lower while a drag increase was observed with sensing at $25l^*$. Koumoutsakos *et al.* [26] determined an optimum height of $15l^*$ at which this normal velocity opposition control yielded a maximum drag reduction. Time averages indicated the formation of a “virtual wall” halfway between the sensing plane and the wall which served to reduce mixing and significantly decrease turbulent energy production. Despite causing a drag reduction, the normal velocity opposition control relied on interior flow field information which is usually not readily available in practical systems. As an alternative, Koumoutsakos *et al.* [26] proposed a control method based on the sensing and manipulation of the vorticity flux from the surface. Such flux was naturally created by the proximity of primary vortical structures inducing secondary vorticity at the wall. For an incompressible flow, the vorticity flux at a stationary wall could be calculated directly from the pressure gradients at the wall – a property readily measurable by wall sensors. Moreover, the no-slip boundary condition could also be replaced with an equivalent vorticity flux boundary condition. This was achieved in a fractional algorithm in which, at each time step, a vortex sheet would be introduced along the surface and allowed to diffuse in the flow with the same effect as a solid boundary. In the case of no actuation, the vortex sheet would be such that the resulting vorticity flux at the wall would match the values calculated from the pressure gradient. Vorticity manipulation was then achieved by assuming the vortex sheet to be a result of a uniform distribution of sources and sinks at the wall. Values of the strength of each source/sink could then be set to either enhance or eliminate the detected vorticity while preserving net zero mass flux across the wall. When applied to enhance the vorticity wall flux sensed through the pressure gradient, the method had a stabilizing effect on the flow. Within the control region, pairs of streamwise vortices were separated and kept near the wall without lifting off. Time averaged results indicated a drag decrease of up to 40% when compared to an unactuated wall. Moreover, Koumoutsakos *et al.* [26] noted that the normal velocity opposition control used by Choi *et al.* [25] was ultimately analogous to the wall vortex flux manipulation method in the manner that both affected boundary layer structures. Close examination of the time-evolution of a streamwise vortex pair under wall-normal blowing/suction also showed an enhancement of secondary vorticity and a suppression of lift-off events. These results gave valuable insight on the flow control mechanisms associated with near-realistic forms of actuation.

The boundary layer control methods described so far involved some form of active control applied at the surface to disrupt turbulence-generating events and reduce drag. However, prior to the advent of MEMS and as mentioned by Coustols and Savill [2], surface texturing had been used in the past to obtain mild drag reductions. The advantage of passive elements were their simplicity and relative ease at which they could be applied to a surface. For this study, riblets or passive elements aligned in the streamwise direction are of particular interest. Square riblet fences were initially studied experimentally by Liu *et al.* [27]. The riblet fences had heights of 1% to 2% of the boundary layer thickness and were placed 30 to $40l^*$ apart, a size on scale with low-speed streaks. Results showed a 3% to 4% drag reduction and a 20% to 25% reduction in the bursting frequency. Alternatively, several riblet configurations with a triangular cross-section were tested based on the fact that reduced turbulent shear stress occurs at the corners of square ducts. Walsh [28] reported that experimental data indicated reduced wall shear stress in the vicinity of the valleys of a triangular riblet but increased shear stress at the peaks. Effects on drag were also dependent on riblet distribution, with drag reductions measured for riblet spacings of approximately $15l^*$ but drag increases occurring for spacings in excess of $30l^*$. Several shapes were tested and optimum drag reductions of 6% to 8% were measured with triangular riblets of sharp peaks whose ratio of height to base width was equal to one. Walsh [28] suggested that drag reductions beyond the values obtained with riblets might be achievable by a combination of riblets and other flow control techniques involving coating or flow injection/suction. For example, Berchert *et al.* [29] combined riblets with surface-mounted slits that would produce streamwise fluid injection and suction based solely on pressure fluctuations of the flow. By careful sizing and placing the devices, drag reductions of nearly 10% were obtained. Walsh [28] suggested that the drag reduction effect of riblets alone was a result of limiting the near-wall spanwise motion of flow structures, a fact later confirmed experimentally by Choi [30]. Numerical simulations by Choi *et al.* [31] reported a weakening of the strength of streamwise vortices above the riblets, suggesting that the sweep and burst events associated with such flow structures were weakened as well. Choi *et al.* [31] also suggested that riblet spacings smaller than the average diameter of a streamwise vortex also exposed a smaller area, namely the riblet crests only, to the effects of a potential sweep resulting in reduced shear stress. Goldstein and Tuan [32] examined the secondary flow associated with riblets and concluded that riblets placed close together shielded each other from cross-flow, dampening spanwise velocity fluctuations and producing drag reductions. However, when placed farther apart, the opposite effect occurred with cross-flow in the valleys being enhanced and resulting in a drag increase. Separate numerical work by Goldstein *et al.* [33] suggested that the natural upward displacement of flow structures provided by a textured surface protruding into the flow also played a role on the drag reduction. Riblets placed close enough could deflect upward the crossflow motion caused by vortices and associated streaks. Local increases in shear stress caused by the vortices occur at their displaced location instead of the wall, further contributing to a local drag reduction.

1.3 The Physics of 2-D Slot Jets

The control mechanisms described in the previous section reflect some of the accumulated understanding on the structure and control of a turbulent boundary layer. However, translating such control schemes into an active, practical device remains an unresolved issue. Control schemes that work well numerically or theoretically may be ineffective when applied by discrete actuators. Conversely, the actuators, by nature of their designs may affect the flow in a manner not entirely desirable or fitting to a particular control method. Therefore, detailed knowledge of a particular actuator and how it affects the flow is needed prior to any flow control study.

Advances in micro-machining techniques have allowed the construction and testing of several low power MEMS (Micro Electronic Mechanical Systems) devices for flow control such as flaps (Sherman *et al.* [34]), surface sensing elements (Liu *et al.* [35]) and synthetic jets (Smith and Glezer [36]). Synthetic jets are of particular interest as sturdy active control devices of zero-net-mass flux requiring no internal fluid supply lines and usable in liquid or gas flow. Synthetic jets, consisting of cavities pressurized by membranes powered by a piezo-electric actuator have been used in flow control experiments and, especially when applied to separation control, have met appreciable success. Smith *et al.* [37] used two adjacent slot jets aligned in the spanwise direction near the point of maximum thickness of an airfoil. When activated, the device produced rolling vortices that were able to maintain attached flow past the stall angle-of-attack and reduce pressure drag by as much as 40%. Similarly, Crook *et al.* [38] used a circular jet mounted near the separation point of a cylinder while Rediniotis *et al.* [39] used slot jets on cylinders and backwards-facing steps to delay separation though enhanced mixing and entrainment of surrounding fluid. Chen and Beeler [40] placed slot jets across an airfoil at several chord locations. When applied to an attached flow, the devices were able to induce changes in the lift coefficient similar to small changes in the angle-of-attack of the airfoil. Peake *et al.* [41] used slot jets mounted diagonally with respect to the freestream direction on the surface of an airfoil. When activated, the slot jets acted as vortex generators to delay separation and provide substantial gains in lift. Despite their success, these studies were conducted at high device Re (O(100) to O(1000)) and relied on the manipulation of the external flow to reduce pressure drag.

The physics of 2-D slot jets were experimentally examined by Smith and Glezer [36] using a single, isolated device. As seen in figure 1.1, the device consisted of a driving a membrane mounted at the bottom of a well and topped with a flat plate containing a rectangular slot of aspect ratio equal to 150. The high aspect ratio of the aperture was used to suppress end-effects on data measured on a plane through the middle of the slot. When driven at the device resonance frequency, ejected fluid separated at the sharp edges of the orifice forming opposing vortex sheets that moved away from the device under self-induced velocity. Each ejected vortex pair translated far enough away so that it was not drawn back into the pumping cavity in the suction phase. This biased vorticity flux accounted for the zero-net mass flux but non-zero momentum flux and impulse of synthetic jets. The jet evolution, as observed in Smith and Glezer [36], was separated into three regions: a laminar near field, a transition region and a turbulent jet region. The near field region was dominated by isolated counter-rotating vortex pairs which quickly became smeared by diffusion within a few slot widths of the orifice. Close examination of the diffused region indicated that the jet underwent transition due to rapidly growing spanwise instabilities within each primary vortex. Following the breakdown of the vortex sheet, the flow in the regions farther from the orifice transitioned to a fully turbulent jet similar to a conventional 2-D jet. Despite such complex jet structure, synthetic jets proved to have similar characteristics to conventional jets. Time average results indicated that the same similarity parameters for conventional jets also applied to the synthetic jets. However, the averaged centerline velocity for the synthetic jet in the region $x/h < 80$ decreased more quickly than for a conventional fully developed 2-D turbulent jet. Consequently, within the same $x/h < 80$ region, the jet width growth rate was also found to be slightly slower than a conventional jet. These discrepancies were considered by Smith and Glezer [36] to be a result of decreased streamwise momentum due to adverse pressure gradients induced during the suction cycles. Despite the oscillatory nature of the jet, integrated net volume flow rates within $x/h < 10$ of the orifice yielded values higher than predicted. Flow visualization suggested that this increase was caused by substantial entrainment of fluid by the counter-rotating vortex pairs. Additional studies by Smith *et al.* [42] placed two synthetic jets adjacent to each other. When pulsed in-phase, both slots formed pairs of counter-rotating vortices. However, the two inner vortices canceled each other so that the net result was still the formation of a single vortex pair. Substantial jet steering was obtained by pulsing the devices out-of-phase – a condition that modified the formation and interaction of the 2 pairs of counter-rotating vortices.

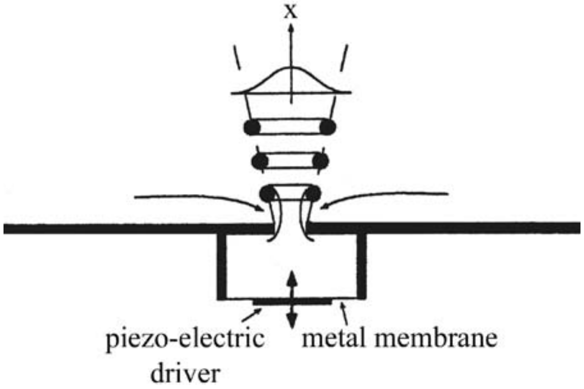

Figure 1.1: Schematic of experimental high aspect ratio slot (taken from Smith *et al.* [42]).

Circular synthetic jets were also examined numerically and experimentally by Mallinson *et al.* [43] with similar results as the slot jets of Smith and

Glezer [36]. Average jet centerline velocity also rose quickly to peak values within a few jet diameters of the exit orifice. The circular jet also had increased volumetric flow rates when compared to a steady turbulent jet due to increased entrainment of surrounding fluid. However, unlike the slot jet of Smith and Glezer [36], the circular jet centerline velocity decay rate was identical to that of steady, axisymmetric turbulent jet. Based on the time-averaged data, Mallinson *et al.* [43] suggested that an average standing vortex ring existed trapped near the exit plane. This standing vortex ring served as a converging-diverging nozzle that quickly accelerated the flow to its peak velocity value. Standing vortices were also inferred in experiments by Schaeffer [44] who linked their existence to the near-field flow evolution. Phase-averaged flow visualization experiments by Schaeffer [44] showed that vortex rings formed in the blowing cycle did not move far enough before the synthetic jet changed phases. As a result, the vortex rings remained near the orifice throughout the suction cycle and were pushed away on the subsequent blowing pulse. Time-averaging the flow data would then result in the standing vortex near the orifice.

Numerically, modeling synthetic jets remains a challenge in some flow regimes. Kral *et al.* [45] solved a boundary value problem for the incompressible, unsteady 2-D Reynolds Averaged Navier-Stokes (RANS) equations with the Spalart-Almaras turbulence model. Initially, the computational domain encompassed only the region external to the jet without the cavity or actuating membrane. The jet presence was simulated by forcing an analytical velocity profile on the boundary region corresponding to the jet orifice. Three velocity distributions were tested: sine, sine^2 and "top hat" with the latter one considered to be closest to the experimental data. Simulations without artificial turbulent dissipation showed that the laminar jet structure of a series of vortex pairs propagating away from the wall persisted far downstream. In comparison, simulations with turbulent dissipation confirmed the experimental observations of Smith and Glezer [36] with vortex cores quickly becoming smeared by turbulent diffusion within a few slot widths of the orifice. Time averaged data also confirmed the experimental results that scaling factors for conventional jets also apply to synthetic jets. Adjacent synthetic jets duplicating the experiments of Smith *et al.* [42] were also examined in Guo *et al.* [46]. For the adjacent jets, in addition to representing the jets by a time varying velocity profile at boundary points, an alternative representation was also used that included the cavity flow. Results found jet steering similar to the experimental results of Smith *et al.* [42]. In addition, it was determined that results from simulations that included the cavity flow were slightly closer to the experimental results. However, the original representation without the cavity was still considered suitable as an initial tool for flow analysis.

Rizzetta *et al.* [47] used a control volume approach with nonlinear artificial dissipation to solve the unsteady, compressible Navier-Stokes equations. The external region, the cavity itself and the throat were calculated on separate grids and linked through a Chimera methodology. Each separate domain contained overlap zones which matched grid points in the adjacent domain to avoid interpolation errors. The membrane motion was represented by varying the position of appropriate boundary points. Although initially limited to a 2-D domain, 3-D simulations were also conducted by assuming symmetry and modeling only one-quarter of the domain. Results confirmed the findings of Kral *et al.* [45] with no jet breakdown observed in 2-D simulations and conventional jets parameters collapsing the velocity data onto single curves. Rizzetta *et al.* [47] also showed that the 2-D internal cavity flow became periodic after several cycles. Therefore, it was considered appropriate to sample and use the velocity profile at the slit plane of the periodic flow as a boundary condition in separate runs involving the external domain only. The fully 3-D simulations also confirmed the experimental results of Smith and Glezer [36]: the external flow breakdown into a turbulent jet was a result of spanwise instabilities in the jet structure.

1.4 Control Methods Involving Realistic Actuators

The numerical studies of Choi *et al.* [25] and Koumoutsakos *et al.* [26] indicated that the dramatic reductions in drag were related to control of vorticity production at the wall. In both studies, flow control was achieved by manipulating streamwise vortices crucial to the near-wall cycle described by Jiménez and Pinelli [8]. For both cases, a continuous distribution of blowing and suctioning at the surface was used to achieve flow control. Such actuation could be seen as an idealized case of a uniform, dense distribution of blowing and suctioning micro-jets. Therefore, although the feedback method described had a potential for application to discrete actuators, it is not physically possible to duplicate the idealized case they modeled. In addition, as pointed out in Gad-El-Hak [11], actuator and sensor placement were also issues that must be addressed as well in any practical attempt at flow control. Several experimental flow control studies have been conducted using synthetic jets or other zero-net-mass flow devices. Despite variations in design and placement, all studies met a certain measure of success.

Tardu [48] made use of a high aspect ratio slot jet mounted in the *span-wise* direction with respect to a channel flow. As shown in the experimental setup of figure 1.2, the device had an aspect ratio of 173 and embedded hot wire sensors downstream measured flow conditions following actuation. The device was also attached to a reservoir so it could be operated as conventional (steady) jet instead of a synthetic (unsteady) one. Shear stress measurements at two stations downstream of the actuator indicated local reductions in drag for both steady and synthetic blowing with the larger reduction for the synthetic jet (40%). In the case of the synthetic jet, temporary partial flow-relaminarization was achieved within a pumping cycle immediately downstream of the slot. Time averaged data showed that unsteady blowing enhanced mixing near the wall to the point where the flow acquired isotropic turbulence characteristics. Consequently, turbulence intensities peaked at a lower height when compared to an un-actuated boundary layer. Mean profiles also showed a doubling in the thickness of the viscous sublayer and, within the viscous sublayer, the devices were able to suppress bursting activity and vortex stretching.

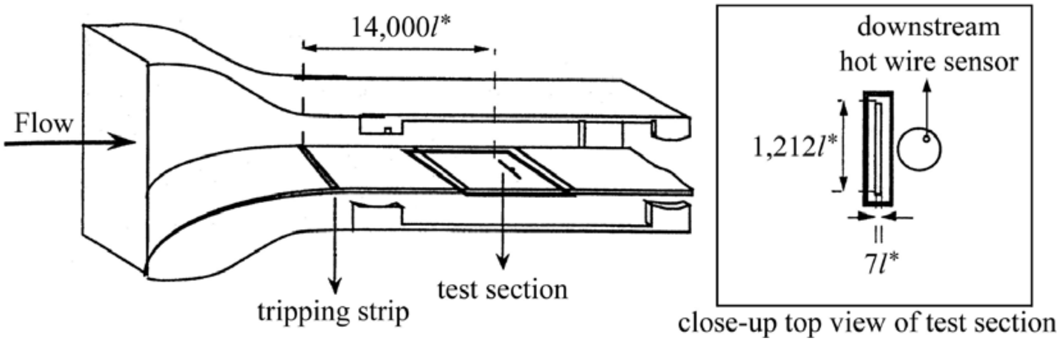

Figure 1.2: Schematic of spanwise slot jet experiment and test section detail (taken from Tardu [48]).

Jacobson and Reynolds [49] used a new actuator design consisting of a high aspect ratio cavity covered with a cantilevered section of the wall. As seen in figure 1.3, when the cantilevered plate oscillated, fluid was drawn in and ejected through the narrow gaps between the cantilevered plate and the side wall to form a jet. The high aspect ratio of the device was such that the surface deflections themselves had a negligible effect on the flow above while the outflow resembled that of a synthetic slot jet. The side gaps were not of equal width so that depending on the combination of geometric and flow parameters, a single vortex pair could be generated over one of the gaps while the other produced only weak disturbances. The devices were mounted aligned with the streamwise direction and with the free end of the cantilevered plate at the downstream edge. Experiments were conducted in laminar flow seeded with artificial disturbances generated upstream of the actuators. In one set of experiments, the actuators were able to substantially delay transition downstream of a vertically-mounted cylinder. Jacobson and Reynolds [49] also looked into possible adaptive feed-forward/feedback control mechanisms. Their control loop was based on shear stress sensors placed upstream and downstream of the actuators. The actuators were set to respond to flow disturbances passing above it so that regions of high shear were pushed away from the wall and regions of low shear were pulled towards the wall. When tested in laminar flow with artificially-generated horseshoe vortices, the control mechanism was successful in attenuating spanwise gradients of streamwise velocity and disturbances near the surface. The actuators were also able to speed up low-speed streaks and slow down high-speed streaks, but only by a few percent. As a result, the actuators did not substantially smooth out the mean spanwise variation of streamwise velocity, which remained distorted by the presence of the horseshoe vortices. This suggested that, if applied to a turbulent flow, the actuators might be too weak to disrupt the breakdown cycle and stabilize the flow.

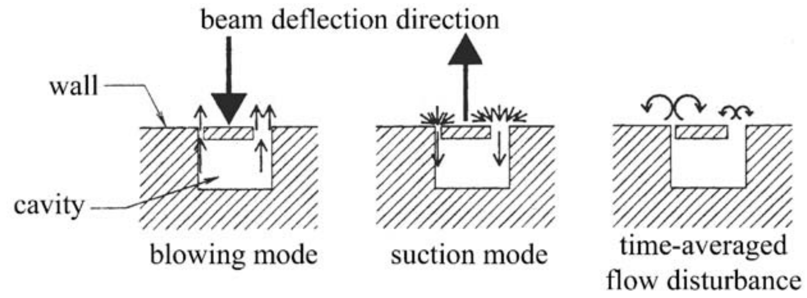

Figure 1.3: Schematic of operation of cantilevered actuator (taken from Jacobson and Reynolds [49]).

Wall sensing, actuation and adaptive feed-forward/feedback control were also tested by Rathnasingham [50]. The devices used were slot jets with an aspect ratio of 15 mounted in the streamwise direction and pulsed at their resonant frequency. As seen in figure 1.4, velocity, shear stress and pressure sensors were mounted upstream of the control location while additional downstream sensors provided feedback for the control mechanism. The control mechanism was set to minimize fluctuations in the streamwise velocity and pressure. Although shear stress was not manipulated directly, it was hoped that actuation on larger flow structures would disrupt enough of the turbulence production chain to produce a positive result. Initially, a single slot/sensor device was tested in a fully turbulent channel flow. Peak reductions in the streamwise velocity fluctuations were roughly of 30% directly over or adjacent to the slot. The slot was found to have an area of effect of approximately 4 slot lengths downstream and 6 slot widths to each side of the actuator. However such effects did not translate into a large reduction in the bursting frequency, which was reduced by over 20% near the slot but quickly returned to un-actuated values away from it. Further examination indicated the presence of two distinct time scales: one associated with the lifespan of the disturbances produced by the actuator and a another, *O(10)* larger than the previous one, associated with the lifespan of the modified structures. This explained the apparent mismatch between the zone of influence of the slot and the lack of a more comprehensive reduction in fluctuations away from the control location. Actuation either enhanced or suppressed bursting events, which in turn became associated themselves with the shorter actuator time scale. Therefore, bursts quickly decayed before being able to affect a larger portion of the flow. In contrast, the zones of influence were created by the flow structures modified by actuation. The longer lifespan of the flow structures allowed them to translate further downstream of the location of the actuators than bursting events and resulted in the large zones of influence. When three actuators were placed in a row four slot widths apart, reductions in the streamwise velocity fluctuations understandably covered a larger area but peak fluctuation reductions were actually lower than for a single actuator. Correlation data, however, indicated that the modified flow structures were more widely spaced and weaker when compared to an un-actuated case and shear stress measurements indicated a 7% reduction across the span of the control area.

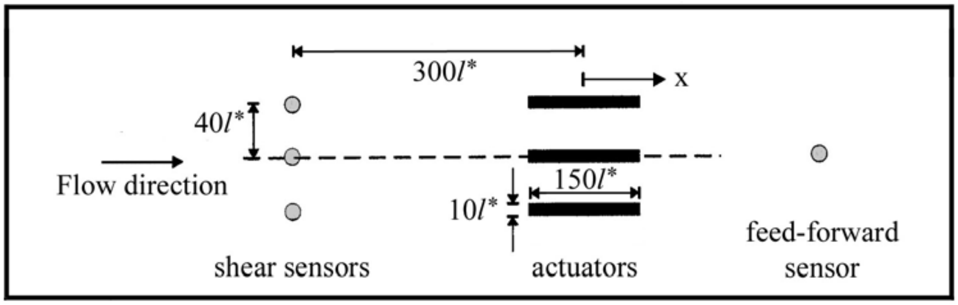

Figure 1.4: Schematic of feed-forward control experiment on a row of slot jets (taken from Rathnasingham [50]).

1.5 Present Work on Control Methods with Slot Jets

Despite the presence of the numerical and experimental work described so far, several questions still remain on the issue of flow control. As shown in the DNS work of Choi *et al.* [25] and Koumoutsakos *et al.* [26], there is considerable understanding behind certain concepts of flow control for turbulent boundary layer drag reduction. But as demonstrated by the experimental work done so far, several issues remain on how to translate such concepts into practical devices. Basic design considerations still remain unresolved regarding the type of actuator needed. Once a design is agreed upon, there are issues regarding its placement to produce the most impact. For example, Tardu [48] chose to mount slot jets across the flow while Rathnasingham [50] preferred to align them in the streamwise direction. Also for each design, there are many geometric and flow parameters that need to be investigated for a better understanding of the devices interaction with the flow. Lastly, as noted in the work of Rathnasingham [50], actuation may lead to a local favorable result, but left unchecked, altered structures in their longer lifespan may cause a negative impact further downstream. Moreover, despite local reductions in shear stress, no experiments have shown a net global drag reduction to date.

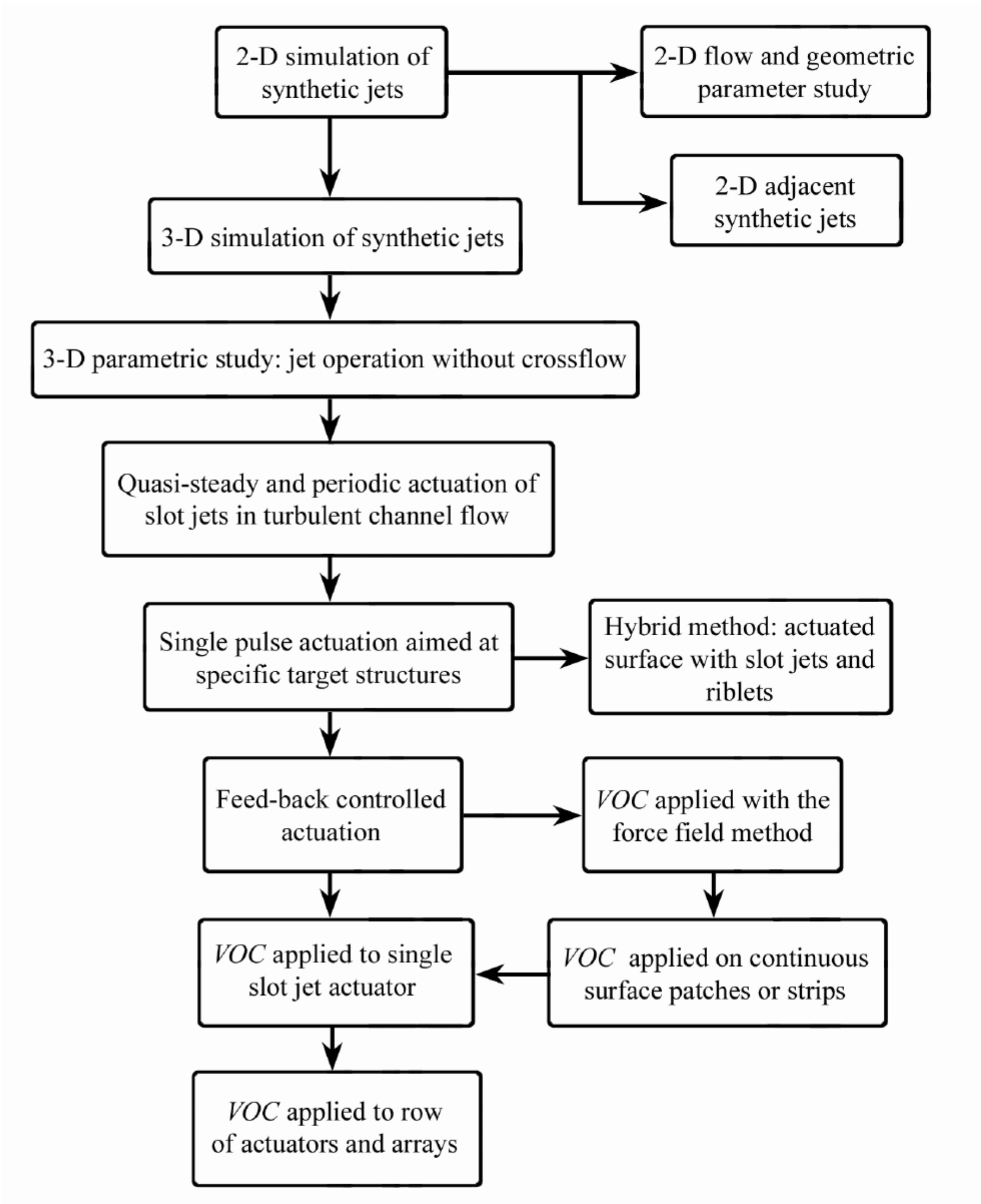

Figure 1.5: Flowchart of cases conducted in this study.

The present study seeks to apply a numerical method to ascertain the potential of flow control for drag reduction using a particular type of actuator: synthetic slot jets aligned in the streamwise direction. This was done systematically as shown in the flowchart of figure 1.5. Each element in the flowchart pertains to a particular objective that was sought and each served as a contributing step towards the overall goal of achieving a global drag reduction with discrete actuators. Each element of the flowchart is briefly dicussed below.

- *Application of the force field numerical method to simulate the driving mechanism of a 2-D slot jet.*

  The numerical method used here incorporates a force field method to simulate the presence of both stationary and moving surfaces within the domain. While this method was validated for simpler geometries, it had not been applied to simulate the internal driving structure and external flow of devices like synthetic jets. Therefore, as a first step, the suitability of the numerical method to simulating synthetic jets was tested in a simplified 2-D domain.

- *Conducting parametric studies on the 2-D slot jet.*

  Parametric studies were conducted on flow parameters such as viscosity and pulsing frequency. Geometric parameters such as slot geometry and domain size were also considered.

- *Full 3-D definition of slot jets and driving mechanism.*

  Once the 2-D actuator model was validated against experiments, a full 3-D definition of the slot jets was incorporated into a channel domain.

- *Conducting parametric studies on the 3-D slot jets.*

  A brief parametric study was conducted on the 3-D actuators in the absence of channel flow to determine the features of the 3-D jets and performance characteristics of the actuators. A separate parametric study was also conducted on the domain with channel flow but with no actuation from the devices to determine the nature and extent of the interaction between the inactive slot geometry and near-wall turbulence.

- *Slot jets coupled with turbulent channel flow and pulsed with time-varying actuation modes of arbitrary strength.*

  Two time-varying forms of actuation were tested: a quasi-steady blowing mode in which the slots were set to operate with a step-like actuation and a continuous sinusoidal pulsing mode. Results showed that modest strength blowing slots generated considerable vorticity and could impact significantly on boundary layer structures.

- *Single pulses for flow control purposes aimed at specific structures or in a hybrid method.*

  Slot jets were used in an attempt to obtain some positive flow control by issuing single blowing pulses aimed at specific turbulent flow target structures or in combination with surface textures in a hybrid method. However, increased mixing from the single pulse prevented either method from achieving useful flow control.

- *Feedback-controlled actuation with Velocity Opposition Control.*

  Results from single pulses indicated that a feedback loop had to be used to calibrate the strength of actuation. The *VOC* method used successfully by Choi *et al.* [25] was selected to control the actuators. This *VOC* method was tested with the present numerical method and progressively discretized down through a sequence of steps in order to be applied to an array of actuators.

- *Discretizing the VOC method: VOC strips*

  The *VOC* method was first applied to strips spanning the width but covering only a portion along the length of the surface. This was done since realistic actuators can be expected to behave as discrete patches of control rather than a uniform control plane as in Choi's *et al.* [25] original formulation of the *VOC* method.

- *Discretizing the VOC method: VOC applied to a single slot.*

  The *VOC* method was then applied to a single slot to determine its performance characteristics. Zones of influence were determined that were used to determine the best spacing of subsequent arrays of actuators.

- *Discretizing the VOC method: VOC applied to a row of actuators.*

Results from a single slot allowed the design of a row of individually powered and individually controlled actuators. The combined effect of multiple actuators placed close together were determined and used for the final step of the study.

- *Feedback-controlled actuation applied to an actuator array.*

  A full array of as many as 18 actuators placed in 3 rows and throughout the surface in both the streamwise and spanwise direction were finally tested as a concept for a practical drag reduction system.

The actuator array was capable of producing a small, global reduction in drag but perhaps through different mechanisms than the *VOC* method. Unlike Choi's *et al.* [25] approach, the actuators were discrete and sparsely distributed as opposed to a uniform distribution of sources and sinks. As a result, the discrete actuators had a limited impact on the boundary layer itself so that no substantial dampening of flow fluctuations was observed. Instead, the drag reduction appeared to be linked to the slots behaving as shallow cavities of reduced shear stress – a result further suggested in laminar runs with the same geometry.

Chapter 2

Numerical Method

2.1 DNS Method and Virtual Surfaces

The DNS method used in these simulations was based on that developed by Kim *et al.* [6] to examine turbulent channel flow. The channel was defined as periodic in the streamwise (x) and spanwise (z) directions and bounded by solid flat surfaces in the normal (y) direction. Following the derivation shown by Kim *et al.* [6], the governing equations were the incompressible Navier-Stokes equations and continuity written as:

$$\frac{\partial \vec{u}}{\partial t} + (\vec{u} \cdot \vec{\nabla})\vec{u} = -\vec{\nabla} p + \frac{1}{Re}\nabla^2 \vec{u} \tag{2.1}$$

$$\vec{\nabla} \cdot \vec{u} = 0 \tag{2.2}$$

where Re denoted the Reynolds number defined according to the channel half-height. By using the following vector identity involving the velocity ($\vec{u}$) and the vorticity ($\vec{\Omega}$) vectors:

$$(\vec{u} \cdot \vec{\nabla})\vec{u} = \vec{\nabla}(\frac{1}{2}\vec{u} \cdot \vec{u}) - \vec{u} \times \vec{\Omega} \tag{2.3}$$

the momentum equation can be converted into:

$$\frac{\partial \vec{u}}{\partial t} = \vec{H} - \vec{\nabla}(P + \frac{1}{2}\vec{u} \cdot \vec{u}) + \frac{1}{Re}\nabla^2 \vec{u} \tag{2.4}$$

where $\vec{H}$ denotes the cross product:

$$\vec{H} = \vec{u} \times \vec{\Omega} \tag{2.5}$$

with the following components in the x, y and z-directions, respectively:

$$H_1 = u\frac{\partial u}{\partial x} + v\frac{\partial u}{\partial y} + w\frac{\partial u}{\partial z} \tag{2.6}$$

$$H_2 = u\frac{\partial v}{\partial x} + v\frac{\partial v}{\partial y} + w\frac{\partial v}{\partial z} \tag{2.7}$$

$$H_3 = u\frac{\partial w}{\partial x} + v\frac{\partial w}{\partial y} + w\frac{\partial w}{\partial z} \tag{2.8}$$

Equation (2.4) can be further manipulated to eliminate the gradient of pressure and magnitude of velocity terms. The final result are a fourth order equation for the wall normal component of velocity, v, and a second order equation for the the vorticity in the y-direction, Ω_y:

$$\frac{\partial}{\partial t}\nabla^2 v = h_v + \frac{1}{Re}\nabla^4 v \tag{2.9}$$

$$\frac{\partial \Omega_y}{\partial t} = h_g + \frac{1}{Re}\nabla^2 \Omega_y \tag{2.10}$$

where:

$$\Omega_y = \frac{\partial u}{\partial z} - \frac{\partial w}{\partial x} \tag{2.11}$$

$$h_v = -\frac{\partial}{\partial y}\left(\frac{\partial H_1}{\partial x} + \frac{\partial H_3}{\partial z}\right) + \left(\frac{\partial^2}{\partial x^2} + \frac{\partial^2}{\partial z^2}\right) H_2 \tag{2.12}$$

$$h_g = \frac{\partial H_1}{\partial z} - \frac{\partial H_3}{\partial x} \tag{2.13}$$

The spatial derivatives were expanded in a spectral method with Fourier series in the streamwise and spanwise directions and Chebyshev polynomials in the normal direction. Time stepping was done with a semi-implicit scheme with an Adams-Bashforth formulation for the non-linear terms and Crank-Nicholson for the viscous terms. A Chebyshev-tau method is employed to solve for the normal component of velocity, v. The streamwise and spanwise velocities, u and w respectively, were obtained from the continuity equation and the definition of Ω_y. Computations were performed in spectral space on a grid expanded by a factor of $^3/_2$ (to avoid aliasing errors) and projected back onto physical space. Spectral representations made this method attractive due to the low computational cost of fast transform methods and for the accuracy of results.

Modifications made to the code allowed the use of virtual surfaces. This method, related to that of Peskin [51] and developed by Goldstein *et al.* [52], imposed a localized body force along desired points in the computational mesh to bring the fluid there to a specified velocity so that the force could have the same effect as a moving or a solid boundary. This combination of DNS and virtual surfaces was validated against experiments for several types of geometries such as riblets [33] [32], cylinders [53], flat plates and wires [52]. As described in Goldstein *et al.* [52], the virtual surface method was applied by incorporating a body force $\vec{F}$ to the right-hand side of equation (2.4) in the form:

$$\vec{F}(\vec{x}_s, t) = \vec{G}(\vec{x}_s, t)\delta(\vec{x} - \vec{x}_s) \tag{2.14}$$

where $\vec{x}_s$ corresponded to gridpoints at which a specified velocity was imposed and $\vec{x}$ corresponded to any location in space. The feedback force vector $\vec{G}(\vec{x}_s, t)$ incorporated an iterative feedback loop to determine the appropriate force to be applied to the local flow field. For example, given a moving boundary with velocity $\vec{U}_{desired}(\vec{x}_s, t)$, the difference between the fluid velocity and the desired velocity is:

$$\Delta\vec{U}_s = \vec{U}_s(\vec{x}_s, t) - \vec{U}_{desired}(\vec{x}_s, t) \tag{2.15}$$

A suitable expression for $\vec{G}(\vec{x}, t)$ on the grid is:

$$\vec{G}(\vec{x}_s, t) = \alpha \int_0^t (\Delta\vec{U}_s)dt' + \beta(\Delta\vec{U}_s) \tag{2.16}$$

and if the boundary is stationary, $\vec{U}_{desired}$ is zero. The constants α and β were negative with dimensions of $M/(L^3T^2)$ and $M/(L^3T)$, respectively.

In order to ensure a degree of smoothness to any surface constructed with the virtual surface method, Goldstein *et al.* [52] smoothed the force field vector, $\vec{F}(\vec{x}_s, t)$, with a narrow Gaussian distribution. Since the program looped through y-planes one index at a time, data were available one xz-plane at a time. Consequently, the Gaussian spatial smoothing was applied to the periodic x and z directions only in the form:

$$\vec{F}(\vec{x}, t) = \sum_{all\vec{x}_s} \vec{F}(\vec{x}_s, t) e^{-\epsilon[(i-i_s)^2+(k-k_s)^2]} \tag{2.17}$$

where i_s and k_s are xz-plane grid coordinates of $\vec{x}_s$ and i and k are grid coordinates of $\vec{x}$. Despite smoothing, such pointwise application of the force field still produced oscillations in the spectral method which, left unchecked, would remain at a constant amplitude throughout the runs. In order to reduce such phenomena, Goldstein *et al.* [52] also applied a low pass filter, K, in spectral space to the coefficients of the quantity $\vec{u} \times \vec{\Omega} + \vec{F}$ in the form:

$$K = e^{\ \xi_2 (n_x/N_x)^{\xi_1}} e^{\ \xi_2 (n_y/N_y)^{\xi_1}} e^{\ \xi_2 (n_z/N_z)^{\xi_1}} \tag{2.18}$$

where n_x, n_y and n_z were the spectral mode indices in the x, y and z directions, respectively. N_x, N_y and N_z were the total number of modes in the same directions and ξ_1 and ξ_2 were constants. Since the greatest oscillations occurred at the highest wave numbers, a $\xi_2 = -1$ was used to reduce the highest spectral coefficient by a factor of $1/e$. Using a $\xi_1 = 20$ also ensured a sharp cutoff of the highest modes.

2.2 2-D Computational Domain

Since this study sought to accurately simulate the flow produced by slot jets, such simulations had to include a certain amount of the internal structure necessary for the operation of the devices. Consequently, the suitability of the spectral-DNS and virtual force method had to be assessed prior to a full 3-D simulation with turbulent flow. To this end, several 2-D simulations were conducted first, both for validation purposes and to give some insight into the multitude of flow and geometric parameters that could affect the performance of the devices.

2.2.1 2-D Baseline Domain

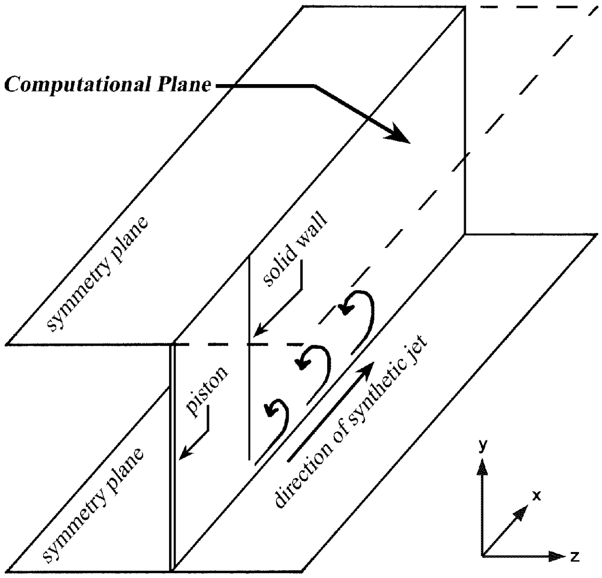

Figure 2.1: Schematic of 2-D simulation plane.

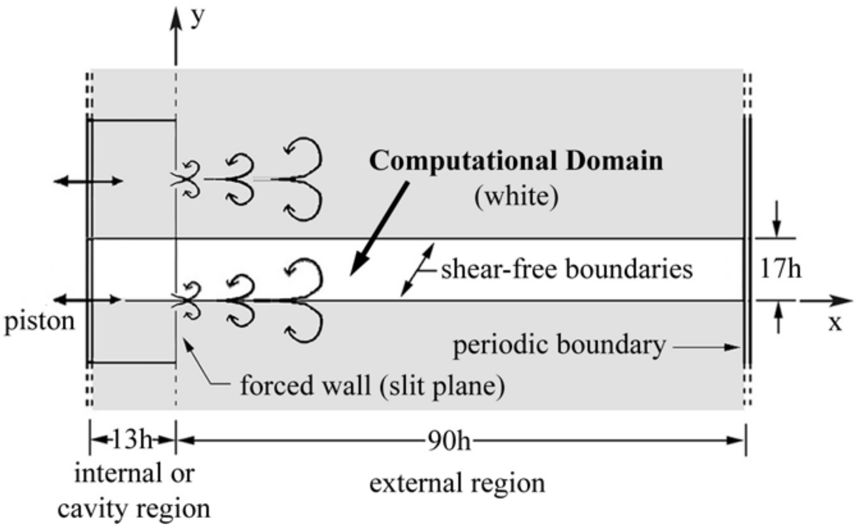

Figure 2.2: Plane view of computational domain showing the periodicity of the pulsing jet arrays formed the symmetry boundaries.

A simpler, separate 2-D code was used to test the adequacy of the force field method for simulating the driving mechanism of the jets and to examine the flow of 2-D slot jets. As seen in figure 2.1, the 2-D domain was created by applying the numerical method on a single xy-plane of the channel simulation. The computational domain contained half of a synthetic jet set to blow in the x-direction. The physical interpretation of the computational domain is shown in figure 2.2. The upper and lower boundaries are defined as shear-free or slip surfaces, so that the simulation corresponds to an infinite periodic array of jets. The baseline grid measured 512×128 gridcells in the x and y directions, respectively. The x-direction remained Fourier periodic while the Chebyshev y-direction was bounded by shear-free surfaces to represent the symmetry of planes. Taking the slot width h as a scale factor, a moving piston of thickness

$0.6h$ created with the force field was placed on the left side of the domain while a solid wall $0.2h$ thick was placed $13h$ from the piston to separate the internal from the external flow. Since the flow was periodic in the x-direction, the piston on the left side of the domain was also present on the right side of the domain. However, due to the sizable aspect ratio between the piston span and the slot, small displacements of the piston were enough to create a substantial jet out of the cavity while causing a negligible effect on the far field. As a matter of fact, the baseline velocity amplitude applied to the piston section translated into an actual displacement of ± 1.82 gridcells in the x-direction ($\pm 0.37h$) to either side of the domain.

For the slot jets, the parameters of interest are the Reynolds number and Strouhal number defined according to the slot half-width, $h_{1/2}$, and peak average blowing velocity, $\overline{u}_{peak}$, as:

$$Re_{jet} = \frac{\overline{u}_{peak} h_{1/2}}{\nu} \tag{2.19}$$

$$St_{jet} = \frac{2\pi f h_{1/2}}{\overline{u}_{peak}} \tag{2.20}$$

where f was the frequency of the piston motion. The piston motion was emulated with the force field method by imposing a sinusoidal velocity ($U_{piston}(t) = Asin(2\pi ft)$) along the x-direction of the piston region of the domain while maintaining the vertical v-velocity at zero. Thus, for an incompressible fluid, the mean jet velocity at the orifice at any instant ($\overline{u}_0(t)$) and the peak average blowing jet velocity ($\overline{u}_{peak}$) could then be determined simply from the area ratio between the piston and jet aperture:

$$\overline{u}_0(t) = U_{piston}(t)\frac{h_{piston}}{h} \qquad and \qquad \overline{u}_{peak} = A\frac{h_{piston}}{h} \tag{2.21}$$

Also of interest were the stroke length L_0 and the average impulse per unit width I_0 given as:

$$L_0 = \int_0^{T/2} u_0(t)dt \qquad and \qquad I_0 = \rho h \int_0^{T/2} u_0^2(t)dt \tag{2.22}$$

where $T/2$ corresponds to half a period in which the slot goes through a blowing and suctioning cycle and ρ is the fluid density. From the definitions of $u_0(t)$ and u_{peak}, it can be shown that for this study, St_{jet} was exactly $2h_{1/2}/L_0$.

2.2.2 Modifications to 2-D Domains

The above baseline domain was used in the initial part of the study. As the study progressed, modifications were made to the initial domains to observe the effect of different geometric parameters or to better isolate a certain factor for further investigation. These modified domains are described here.

2-D Lip Shapes

The 2-D baseline case was modified in order to conduct a parameter study of how different geometric factors influenced the slot jet flow. While changing the size of the domain was rather straightforward, variations on the thickness and geometry of the lips of the slot jets required redefining the location of solid boundary points. The different types of lips tested are shown schematically in figure 2.3.

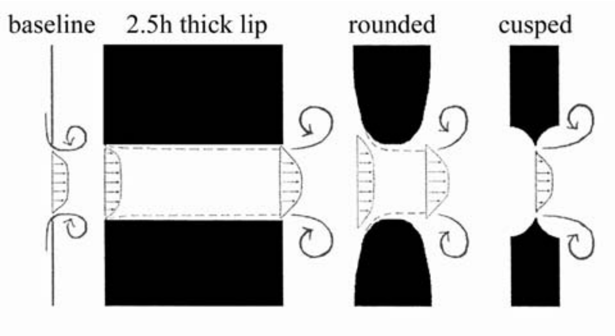

Figure 2.3: Schematic of types of lips tested.

A thicker, flat lip was obtained by increasing the number of grid columns that made up the dividing wall between the cavity and the external domain. Starting from the baseline thickness of $0.4h$, the lip was progressively thickened up to $2.5h$. The $1h$ thick lip was further modified into a smooth, roughly parabolic lip and a sharp, cusped lip. Both modifications were obtained by appropriate selection of grid points representing solid boundaries.

2-D Adjacent Jets

An additional geometry with adjacent synthetic jets was also used in an attempt to replicate the experimental results of Smith *et al.* [42]. Experiments showed that, when pulsed in-phase, the jet structure from adjacent slot jets was similar to the one of a single slot but substantial jet steering could be achieved by pulsing out-of-phase. The 2-D computational domain was modified as in figure 2.4 to contain two slot jets with independent pumping membranes. Similar to the experiments, this new geometry was created by placing a horizontal wall 2.3h thick along the centerline to separate the cavity into two chambers of approximately the same size. The vertical walls separating the chambers from the external domain were set to be 2.5h thick.

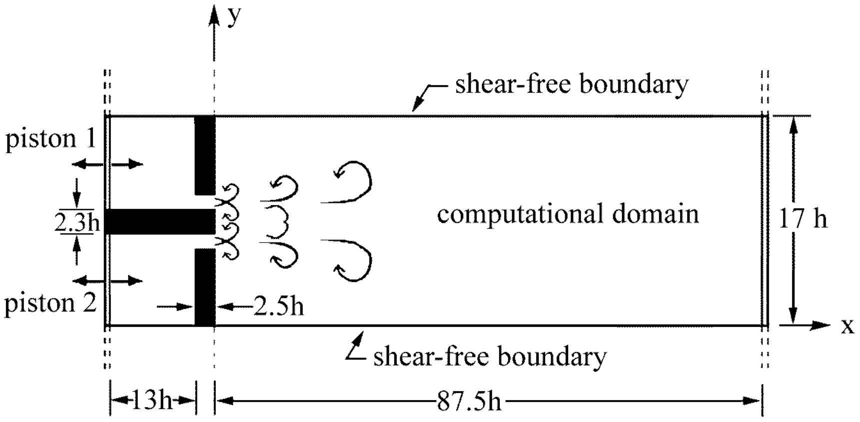

Figure 2.4: Schematic of periodic array of 2-D adjacent jets.

2.3 3-D Computational Domain

Once 2-D simulations were studied in detail, the actuator design was translated into fully 3-D simulations. The baseline as well as modifed domains used in this part of the study are described in this section.

2.3.1 3-D Simulation Baseline Domain

Results from the 2-D study gave some insight into the geometric parameters that affected the performance of the slot jets. These results will

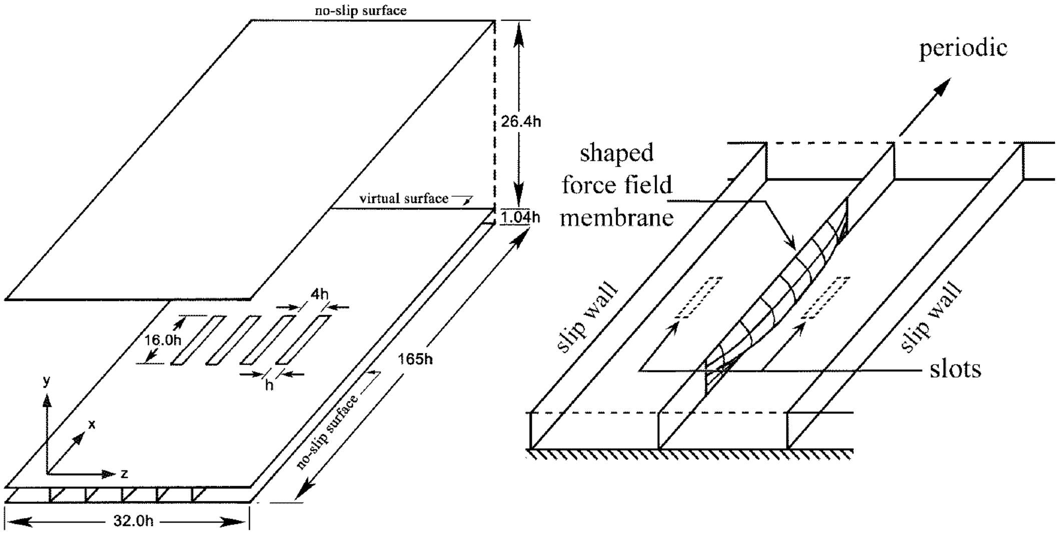

(a) (b)

Figure 2.5: (a) Schematic of channel and 3-D slot jets and (b) sub-surface actuator detail.

be discussed in detail in Chapter 3. For the present, it suffices to say that these results were incorporated in the design of the slot jets for the 3-D domain. As for the domain used in the original study by Kim *et al.* [6], the channel was covered with a grid $128 \times 64 \times 128$ cells in the x, y, z directions, respectively. The grid spacing was regular in the streamwise and spanwise x and z-directions, respectively while grid clustering was applied in the normal y-direction to better resolve the boundary layer flow.

The basic 3-D domain used initially is schematically shown in figure 2.5(a). The domain consisted of a channel with the jets mounted at the bottom and set to blow into the normal direction into the cross flow of the channel. The apertures for the slot jets were created by placing a raised plate containing the four slots 8 grid planes above the bottom of the channel. Flow down the channel along the streamwise x-direction was driven by a constant gravitational force imposed with the virtual surface method. Each slot was 6 grid cells wide with an aspect ratio of 16. The raised plate was made of 2 grid planes for a thickness of $0.54h$. A finite plate thickness was needed since, as demonstrated later, the device performance is influenced by the thickness of the aperture. In addition, most slots used in real experiments have flat thick lips.

As seen in figure 2.5(b), the internal geometry needed to power the actuators was created by placing dividing walls spanning the length of the domain between the plate and the channel. While each slot had its own cavity, each pair shared a driving membrane, twice as long as the slots themselves, mounted on the dividing wall. Each actuator was thus made up of two slot jets coupled 180^o out of phase. Such coupled design allowed the specification of a desired jet strength while satisfying continuity over the entire domain. The divider walls were defined as shear-free walls that allowed fluid motion in the x and y-direction but no penetration in the z-direction. These shear-free conditions were necessary to reduce Gibbs phenomena that created "ghost" impressions of the internal geometry above the plate. To better simulate the membrane motion, the magnitude of the z-velocity specified along the driver section of the divider wall was shaped with a sine distribution surface. Since the fluid was incompressible and the domain periodic in the x-direction, the spanwise sub-surface mass fluxes through the membrane alone were sufficient to create net mass fluxes through the slots.

The parameters of interest for the 2-D simulation are also important to the 3-D simulation. In addition to the device Reynolds and Strouhal numbers (Re_{jet} and St_{jet}, respectively), the channel simulation also made use of a channel Reynolds number and a friction Reynolds number defined as:

$$Re_{channel} = \frac{\overline{u}_{channel} h_{channel}}{\nu} \qquad and \qquad R^* = \frac{u^* h_{channel}}{\nu} \tag{2.23}$$

where $\overline{u}_{channel}$ was the average channel centerline velocity, $h_{channel}$ was the domain half-height and u^* was the friction velocity.

2.3.2 Modifications to 3-D Domains

The baseline domain described above was useful for an initial analysis of discrete actuators in fully turbulent flow. However, design restrictions such as coupled actuation and large reservoir cavities limited their application. In this case, new designs more suitable for flow control purposes were formulated and are described here. These modified domains are later discussed in more detail along with results in their respective chapters.

3-D Single Actuator

In the fully 3-D channel flow, the baseline domain was modified to contain a single actuator comprised of two coupled slots as seen in figure 2.6. This was a necessary design modification to test the effectiveness of control algorithms on a nearly isolated slot. The slots were scaled up to have a surface area 3 times larger than the initial design in order to enhance flow features. As seen in figure 2.6, the slot width measures $18.2l^*$ with an aspect ratio of 12.4. The flat plate containing the slots was moved up to cover grid planes 11 and 12 for an overall thickness of $3l^*$ so that a larger membrane could be used to drive the flow. The increased size of the driving membrane was needed to reduce the amplitude of the driving signal and decrease the amount of Gibbs phenomena that would leak through the plate onto the channel.

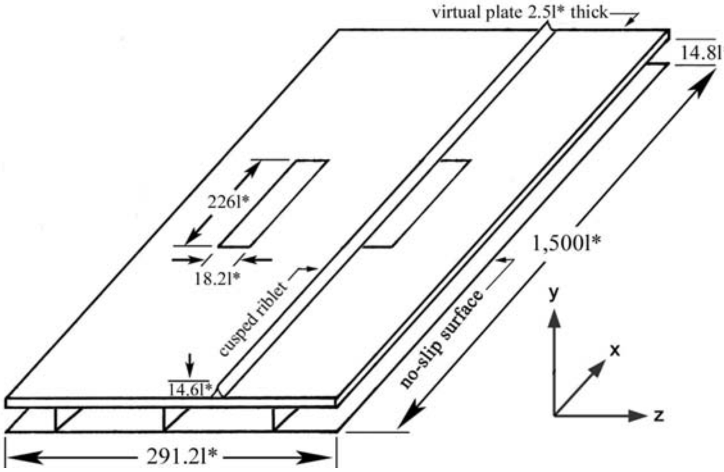

Figure 2.6: Schematic of 3-D single actuator domain with longitudinal riblet.

This design was also used to study the effect of combining a passive element with a slot jet to form a hybrid surface. To this end, cusped streamwise riblets spanning the length of the domain were placed next to a slot as shown schematically in figure 2.6. The riblet crested at grid plane 16 for an overall height of $14.6l^*$ above the plate – in scale with riblets used on experiments by Walsh [28] and Coustols and Savill [2].

3-D Multiple Actuators

The coupled nature of the previous actuator designs, although convenient, also limited the amount of flow control that could be imposed. For each slot acting to control the flow above it, there was a corresponding “breather” slot whose behavior would be mostly detrimental. If a feedback control scheme was to be used, a new type of actuator was needed to ensure that all slots would be working together to reduce drag.

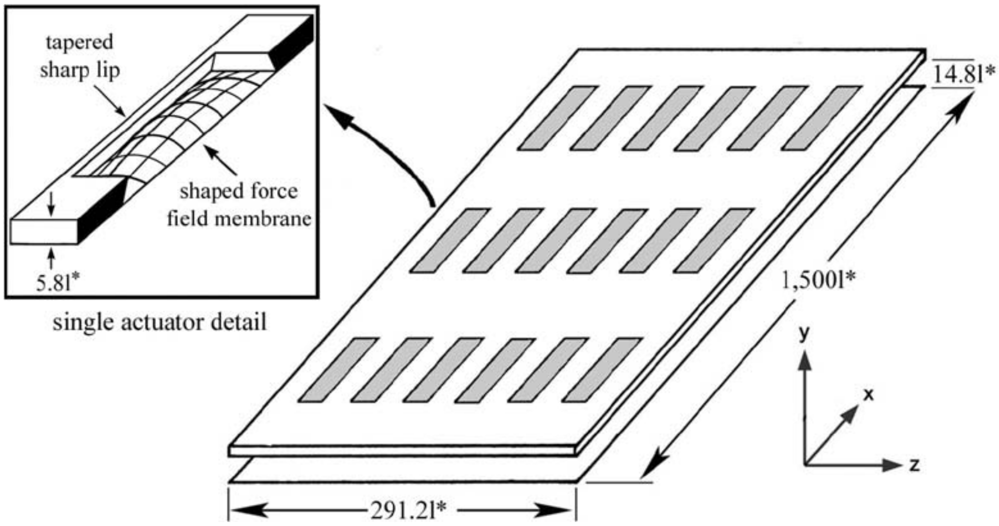

Figure 2.7: Schematic of 3-D multiple actuator domain and single actuator detail.

The new actuator design is shown schematically in figure 2.7 as multiple rows of actuators. The subsurface structure was replaced with individual membranes mounted flushed at the bottom of a raised plate covering grid planes 10 through 12 for a corresponding thickness of $5.8l^*$. The lips of each slot were also tapered being wider at the membrane location and narrower at the exit plane. While each slot had its own driving mechanism, all slots shared a common sub-surface cavity that supplied fluid for the pumping action. This design made use of particular advantages of the virtual surface technique for applying boundary conditions. With a shared cavity and the conservation of mass in an incompressible flow, all slots can not actuate in the same direction at the same time (*i.e.* all slots cannot be blowing). Generally, with a large number of slots, this would not occur. But, if all slots were directed to produce the same net flow condition, the force field implementation of eq. 2.14 would allow the slots to compete with each other. Slots in need of the greatest mass flow would automatically obtain it at the expense of the other slots. Obviously, the amount of competition should decrease as the number of slots increased. Several geometries were used and it was determined that as few as 4 slots were able to adequately operate without compromising the integrity of the numerical method. The use of the integral and direct feedback of velocity in the force field method thus provided a simple and flexible solution to a problem which might otherwise have been difficult to solve.

2.4 Convergence Issues

The stability characteristics of the force field method were addressed in Goldstein *et al.* [52] and discussed in detail more recently in Lee [54]. For the second-order Adams-Bashforth formulation used, Goldstein *et al.* [52] conducted a parametric study on the force field parameters α and β of equation (2.16) to determine the following relationship for the stability of the time step:

$$\Delta t < \frac{-\beta - (\beta^2 - 2\alpha k)^{1/2}}{\alpha} \tag{2.24}$$

where k is a problem-dependent constant of order one.

Alternatively, Lee [54] performed a detailed analytical stability analysis to determine the following expression for the stability of the time step:

$$-\frac{\alpha \Delta t^2}{2^{D-1}} - \frac{2\beta \Delta t}{2^{D-1}} \leq 2 \tag{2.25}$$

where D is the dimension of the simulation. Let AB denote the expression on the left of the inequality (2.25) so that values of $AB \leq 2$ were required to maintain stability.

As formulated in this section, the numerical method and the stability limit proposed by Goldstein *et al.* [52] were considered by Fadlun *et al.* [55] as being too rigid. Application of the force field method to 3-D curvilinear surfaces were reported to require very small time steps and resulted in CFL numbers of O(10^{-2}). Consequently, Fadlun *et al.* [55] proposed a modified method in which the force field was applied on a separate grid and then projected onto boundary points of the computational grid. Further modifications by Kim *et al.* [56] added mass sources/sinks to satisfy continuity over each computational cell. However, the geometries used in the present study were mostly rectangular and consequently did not have the same time stepping restrictions encountered by Fadlun *et al.* [55]. As it will be later demonstrated in this section, the previously described domains had no restrictive stability limits associated with the application of the force field formulation. The time steps used were consistent with the limits dictated by both Goldstein *et al.* [52] and Lee [54] and solutions were found to converge within expected parameters.

2.4.1 2-D Convergence Issues

For 2-D studies, the force field parameters of equation (2.16) were kept at $\alpha = -500,000$ and $\beta = -300$. For such parameters, the limiting time step according to the Goldstein *et al.* [52] expression is $\Delta t < 0.0015$ for a corresponding Lee [54] parameter of $AB = 0.5$.

Convergence studies on the 2-D simulation were performed and compared to experimental results of Smith and Glezer [36]. Experiments were conducted at a $Re_{jet} = 416.6$ and $St_{jet} = 0.0628$ on an isolated slot jet with square lips $2.5h$ thick. Consequently, in addition to matching flow parameters, the baseline domain was modified accordingly to contain the same lip geometry as the experiments. Flow through the modified slots contained high gradients of velocity, requiring time steps of O(0.0001), well within the time step limit of Goldstein *et al.* [52] and for a Lee [54] parameter AB of O(0.1). Despite a time step one order of magnitude below the stability limit, CFL numbers were not excessively small and remained of O(0.1). In subsequent runs, the time step was adjusted so that each period of actuation corresponded to at least $3,000$ time steps with similar CFL numbers.

Grid independence was verified by using the difference between time-averaged vorticity fields for increasing grid densities as an indication of the convergence of the solution. Results are shown in figures 2.8 and 2.9. For all grid sizes, data were taken over the last 5 cycles of a 20-cycle run and mirror-imaged across the horizontal to make up the full geometry of the 2-D slot jet. Consequently, although the baseline grid contained 512 cells in the streamwise $x-$direction and 128 cells in the vertical $y-$direction, the figure captions present the actual gridsize of the figures, namely 512×256 elements.

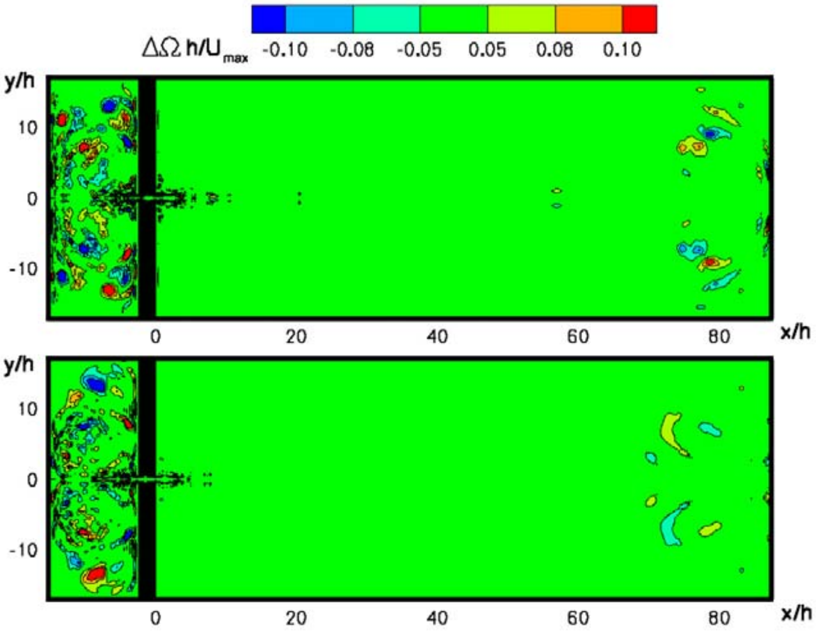

Figure 2.8: Contours of normalized vorticity difference ($[\Delta\Omega\mid_{grid1}$ - $\Delta\Omega\mid_{grid2}$ $]h/u_{peak}$) between grid sizes (top = 512×256 and 512×512, bottom = 512×512 and 512×1024) at $Re_{jet} = 416.6$.

Figure 2.8 compares the baseline grid of 512×256 cells with a medium grid containing 512×512 cells (fig. 2.8, top) and the medium grid of 512×512 cells with a fine grid of 512×1024 cells (fig. 2.8, bottom). The grid was doubled only in the vertical direction since this direction contained the largest gradients. The figure shows considerable noise in the cavity and toward the right hand side of the domain for the baseline grid. Doubling the grid (i.e., halving the mesh size) somewhat reduced the noise in the right of the domain but not much in the cavity. As explained later, the flows at these locations and at this high Re_{jet} were fairly chaotic which caused the discrepancy and made local grid convergence difficult to attain with the amount of data accumulated. However, between the two chaotic regions, there was a broad band from $x/h = 0$ to $x/h \approx 60$ where the flow was nearly periodic in time and the vorticity difference between grids was minimal to non-existent. Since data used to compare the simulation to the experiments were taken from $0 \leq x/h \leq 40$, it was reasonable to assume the solution to be grid independent in this region of interest even on the lower resolution 512×256 grid.

An identical study was performed for a (four times lower) Re_{jet} of 104.2, at which the geometric parameters study was performed. Results are shown in figure 2.9 for the baseline grid of 512×256 against the medium grid of 512×512 (fig. 2.9, top) and the medium grid of 512×512 against the fine grid of 512×1024 (fig. 2.9, bottom). Unlike the higher Re_{jet} results of figure 2.8, stable periodic cells formed at both ends of the domain for this lower Re_{jet}. Differences between grids are minimal throughout the entire domain even for the baseline grid. Further increasing the resolution in the vertical direction further confirmed this result with essentially no difference between the medium and fine grids. Therefore, at this lower Re_{jet}, it was safe to assume the baseline

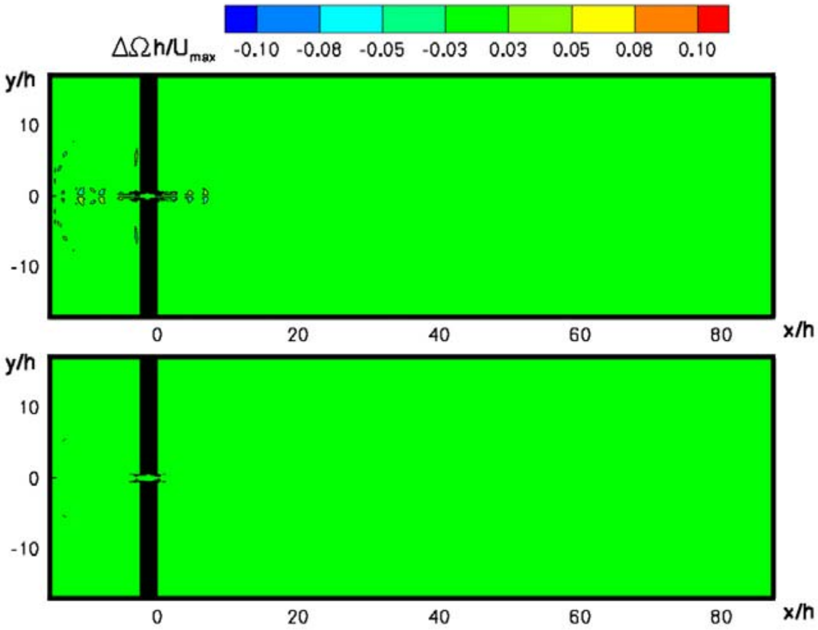

Figure 2.9: Contours of normalized vorticity difference ($[\Delta\Omega\mid_{grid1}$ - $\Delta\Omega\mid_{grid2}$ $]h/u_{peak}$) between grid sizes (top = 512×256 and 512×512, bottom = 512×512 and 512 × 1024) at $Re_{jet} = 104.2$.

grid to be converged over the entire domain.

2.4.2 3-D Convergence Issues

For 3-D studies, the force field parameters of equation (2.16) were kept at $\alpha = -50$ and $\beta = -50$. For such values, the limiting time step according to Goldstein *et al.* [52] was $\Delta t < 0.02$ for a corresponding Lee [54] parameter of $AB = 0.5$. For the 2-D simulations, time steps were ultimately limited by the jet actuation, with time steps held smaller than $1/3000^{th}$ of the period of actuation. However, periods of actuation for the 3-D simulations varied from quasi-steady to periodic and feed-back loop dependent. Although optimizing the time step for each type of actuation would have been desirable to speed up computational runs, a single time step of 0.0075 was chosen for simplicity. This time step corresponded to $1/1000^{th}$ of the period of actuation of jets under periodic pulsing. The corresponding Lee [54] parameter was then $AB = 0.19$, well within stability limits. Similar to the 2-D simulations, the resulting CFL numbers were also O(0.1).

An initial fully developed turbulent channel flow was used as the starting point of the simulations. For the studies on the baseline domain, $Re_{channel}$ was about $1,900$ while R^* was about 119. For consistency, the friction velocity u^*, viscous length scale l^* and viscous time scale t^* were obtained at the opposing top wall of the channel that contained no actuators. Those values were taken as constants and used throughout the study whenever friction properties were needed to normalize 3-D data or figures. The channel dimensions, in wall units, were then $1,500l^* \times 238l^* \times 290l^*$ in the x, y, z directions, respectively. The narrowest slot width used was $9.1l^*$, similar to the size of the devices used in experiments by Rathnasingham [50] while the plate thickness amounted to $2.5l^*$.

With the above normalization factors, the grid spacing in the streamwise and spanwise directions were, respectively, $\Delta x^* = 11.7$ and $\Delta z^* = 2.3$. Such grid resolution was comparable to that of the original study by Kim *et al.* [6] with $\Delta x^* = 12$ and $\Delta z^* = 7$. Here, the finer scale grid was used in the spanwise z-direction to better resolve high spanwise flow gradients near the slots. Goldstein and Tuan [32] and Goldstein *et al.* [33] showed that the combination of turbulent channel DNS and virtual force method, on the same or coarser grids than used here was converged for flow over riblets and wires at the above values of $Re_{channel}$ and R^*. Moreover, Goldstein, *et al.* [52] simulated turbulent flow over a virtual flat plate placed at 15 gridcells or $28.4l^*$ above the bottom of the channel, and found excellent agreement with simulations done without virtual surfaces. Consequently, the near-wall normal cell spacing used (Δy) should also be adequate in the present simulations.

Thus, by comparison to these earlier studies using essentially the same computational code, the present spatial resolution should be adequate (even conservative) to model a turbulent boundary layer. The current virtual force method applied to 2-D slot jets has also been shown in Sec. 2.2.2 to converge for Re_{jet} at least up to 416. Consequently it was reasonable to assume that the present results converge as well since Re_{jet} for 3-D slots was never larger than 34. Comparison of the cell Reynold's number in the direction of highest gradient in the region of the slots (vertical for 2-D, spanwise for 3-D) further indicate convergence. Despite the 3-D slots having only 6 gridcells of width compared to 15 gridcells for the 2-D simulation, the 3-D cell Reynolds number was three times smaller than for the 2-D simulations. Finally, when normalized with wall units, the time step Δt^* corresponded to $0.03t^*$ or less – a conservative value for turbulent boundary layer simulations.

2.5 Drag Calculation

As mentioned previously, the 3-D channel flow was driven by a body force applied to the fluid in the streamwise direction. For assessment of flow control devices, it was necessary to be able to compute the drag on the actuated surface. However, the spectral force-field method used in this study prevented the use of the same drag calculation methods used in the original numerical method described in Kim *et al.* [6].

The original turbulent channel simulation by Kim *et al.* [6] was driven by a pressure gradient in the streamwise direction. Later flow control studies by Choi *et al.* [25] made use of the pressure gradient to calculate the drag on a particular actuated surface. In this case [25], the flow was assumed to have a fixed mass flow rate. Therefore the pressure gradient required to maintain such constant mass flow rate was proportional to the drag on the channel. Such a drag calculation method is not possible for the current simulation method since there is no driving time-varying pressure gradient. Rather, the driving gravitational force G_{force} is kept constant and applied everywhere between the actuated surface and the opposite boundary. No gravitational force is applied at locations specified as a solid, either stationary or moving. Alternatively, drag calculation on an actuated surface could be based on momentum flux through the wall but this method is not pheasible either with the force field method. The force field method applies force vectors to each gridcell marked as solid so that their net, global effext simulates the presence of a solid body. However, because it is still a body force, the exact location where the fluid ends and the solid begins within the cell is unclear. Consequently, the force field method prevents an accurate determination of gradients of the simulated wall. Taking the actual net forcefield over the simulated plate to calculate a drag is also not recommended since the forces themselves depend on the presence of further sub-surface structures. Therefore, the drag on the actuated surface was calculated by conducting a force balance on the *channel flow* itself.

Following Goldstein *et al.* [52] and [33], the gravitational driving force, G_{force} must be balanced by the acceleration of the bulkflow and the shear stresses on the top boundary and actuated surface, namely:

$$G_{force} = F_{bulk} + D_{top} + D_{actuated} \tag{2.26}$$

where the bulk fluid force and the drag on the top boundary can be written as:

$$F_{bulk} = \frac{\partial}{\partial t}\rho \iiint\limits_{V} u\, dx\, dy\, dz \tag{2.27}$$

and

$$D_{top} = \iint\limits_{S} \mu \frac{\partial u}{\partial y}\Big|_{topwall} dx\, dz \tag{2.28}$$

Numerically, F_{bulk}, is determined from the mean mass acceleration within the channel. At each time step, a u_{mean} value is calculated over regions of the domain wherever the gravitational force is applied: fluid in the channel itself and within a slot's cavity but not beneath the simulated plate. This value of u_{mean} is differenced with the value from the previous time step to approximate the mean mass acceleration. Similarly, D_{top} is obtained from an average $\partial u/\partial y$ at the top wall at that particular time step. Since the drag on the actuated surface is the only unknown left in the momentum balance of equation (2.26), it can be determined and used to calculate a drag ratio between the bottom actuated surface and the top boundary:

$$Ratio = \frac{D_{actuated}}{D_{top}} = \frac{G_{force} - F_{bulk} - D_{top}}{D_{top}} \tag{2.29}$$

The above drag ratio calculation differs from the drag calculation in Choi *et al.* [25] in that the drag values calculated at both surfaces in the current study may not be completely independent. For example, due to the conservation of momentum, drag reductions on the actuated surface must be balanced out by an acceleration of the bulk flow, which should induce an increase in shear stress on the top boundary. In the particular extreme case of complete re-laminarization of the flow over the entire channel, the drag ratio between both surfaces would be equal to 1. However, if the actuated surface only changes the near wall flow in a modest way, the drag ratio gives a fair comparison between the effects of actuation and a smooth surface when both are subjected to the same centerline channel flow. A possible method to obtain independent drag calculations would be to apply a particular configuration to both boundaries of the domain and run two parallel simulations: one with the devices operational and another with the devices in passive mode. Unfortunately this would have increased computational time and storage requirements and, oddly enough, might not necessarily be the most suitable form of calculating drag for this study. Consider a feedback-controlled actuation method similar to Choi *et al.* [25] efficient enough to re-laminarize the flow. In this case, the feedback actuation values would effectively go to zero and apart from the initial interaction with a turbulent flow, the devices would be mostly operating on transitional and laminar flow. Thus, while valuable as a tool for instability control, the devices would not yield as much information on turbulence control and flow interactions as they would have if they were subjected to constant turbulence impingement from the opposing wall.

Throughout this study, drag ratio averages for particular 3-D cases are calculated with a 90% confidence interval. This was done by first determing the number of independent realizations in a particular run from the auto-correlation of the drag trace in time. Starting from a full correlation of 1.0 at time step zero, the period of the drag ratio was estimated as the first instance in time where the auto-correlation reached a value of zero. The number of independent realizations varied considerably between runs according to the particular geometry tested or the mode of actuation. The average run of $150,000$ time steps resulted in as many as 28 or as little as 5 independent realizations. Once the number of independent realizations were determined, drag was selectively sampled at the same time interval within each realization to calculate the sample average. The number of independent realizations was also used to obtain the appropriate value for Student's distribution at a 90% confidence interval which was multipled to the final sample average.

Chapter 3

2-D Simulation Results

As noted in Chapter 1, there have been several previous numerical studies of slot jet actuators. The *RANS* method used by Kral *et al.* [45] and the Chimera methodology used by Rizzetta *et al.* [47] were more suitable to the study of isolated jets similar to the experiments of Smith and Glezer [36]. However, those previous studies were not concerned with merging the slot jet actuator with a turbulent boundary layer simulation, a task for which the spectral method used here was quite well suited. Yet, although validated for several turbulent simulations, the current spectral/immersed boundary method was unproven when dealing with slot jets and their internal mechanism. Consequently, the numerical formulation was first tested on a 2-D domain without any cross flow. The goals of this part of the study were thus twofold: to make use the flexibility of a numerical method to conduct studies on both flow and geometric parameters, and to compare the results to experimental synthetic jets for validation purposes.

As indicated in figure 2.2, the 2-D domain orientation is such that streamwise x-direction corresponds to the direction of blowing of the jet while the vertical y-direction is perpendicular to the jet axis. While the simulation domain consisted of an array of periodic jets, experimental data for comparison from Smith and Glezer [36] were obtained on an isolated jet at a Re_{jet} and a St_{jet} of 416.6 and 0.0628, respectively. Initial 2-D simulation results at those flow parameters produced a rather complex flow field. Therefore, a lower $Re_{jet} = 104.2$ with a simpler flow field was used for the flow and geometric parameter studies in order to better isolate the effect of a single variable. Later, the simulation parameters were matched against experimental conditions for validation purposes.

3.1 Baseline Case

Analytically, slot jets have been modeled with surface-normal suction and blowing with no spanwise v-velocity associated with the jet. Such method was used by Kral *et al.* [45] in the form of sine and sine^2 streamwise u-velocity profiles. Further studies including cavity flow, as in Kral and Guo [57], noted an increase in the accuracy the solution but found the results from boundary blowing/suction to be generally adequate. That was not the case with the current simulation method. The present numerical domain (fig. 2.2) included sharp, thin lips and a pumping membrane which combined to produce markedly different results from Kral *et al.* [45] for the flow velocities and vorticity. As seen in figure 3.1(a), the u-velocity profile at peak blowing is “horned” at the edges with peaks around $\pm 0.3h$ and does not resemble the parabolic, top hat, sine or sine^2 expressions previously used to approximate the jet profile. This “horned profile” conformed to distortions common to oscillatory flows as the low momentum boundary layer accelerated more quickly than the core bulk flow. As fluid exited the cavity, separation occurred at the sharp, thin lips and the flow rolled up into a pair of counter-rotating vortices. As a result, the the spanwise v-velocity (fig. 3.1(b)) contains a substantial non-zero component of as high as $\pm 0.24 u_{peak}$ peaking off the centerline of the jet at $\pm 0.32h$. Similarly, the roll up from the lips created vorticity peaks (fig. 3.1(c)) away from the centerline at of the jet at $\pm 0.41h$.

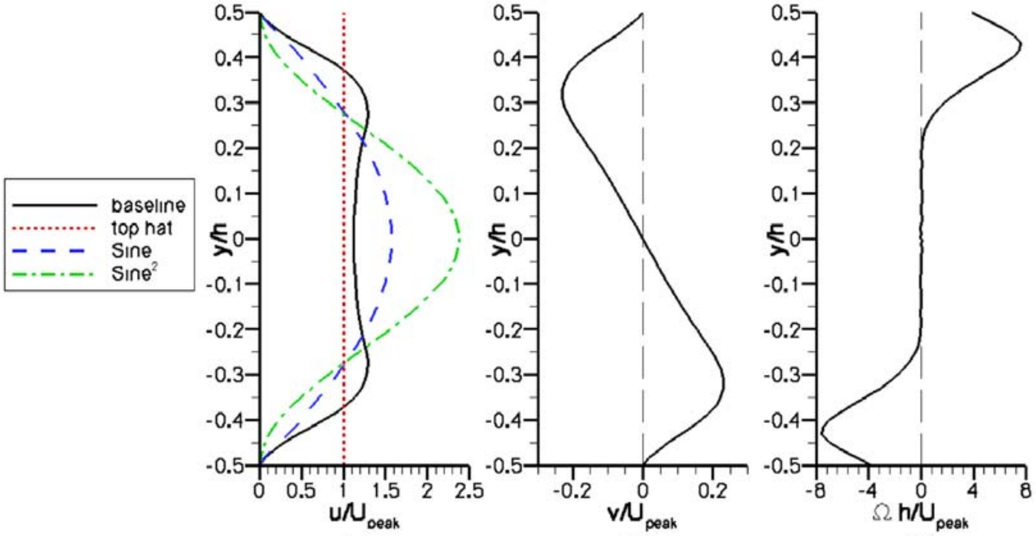

(a) (b) (c)

Figure 3.1: Streamline velocity, spanwise velocity and vorticity at external slot plane for 2-D baseline case ($Re_{jet} = 104.2, St_{jet} = 0.0628$) at peak blowing.

A vorticity contour plot of the baseline case after 10.5 cycles is shown in figure 3.2. Besides the previously mentioned roll-up of fluid at the lips, the external flow presented a phenomena not noted in previous numerical simulations: continuous vortex pairing of the leading vortices of the developing plume. Vortex pairing was not observed in the experiments by Smith and Glezer [36] because the vortices broke down into turbulence within several h of the jet aperture. Pairing in the present simulation is believed to be a consequence of the closed periodic domain of the simulation: lead vortices face a counterflow caused by the far wall and consequently slow down, allowing subsequent vortices to catch up to their position. The merged large vortical structure gradually translated downstream and reached the far right wall. Thereafter, the vortices gradually traveled back upstream (to the left) along the upper and lower walls, the condition shown in figure 3.2, as fluid was drawn upstream along the edges to balance out the fluid entrained by the centerline jet. The pairing events were initially observed at regular intervals. However, after 16 cycles and as the larger merged vortices reach the far wall, a situation approaching a steady state was reached: vortices formed by the fluid ejected through the slit diffused as they translated downstream and became too smeared to be distinguished around $x/h = 55$ so that the location of pairing could no longer be determined. This diffused vorticity eventually merged with the large end vortical structures that slowly translated back toward the left side of the domain. The internal cavity or plenum flow is also seen in figure 3.2. As found by Rizzetta *et al.* [47], a single main circulation cell developed in the cavity. However, while Rizzetta *et al.* [47] reported that the circulation cell became stable after a few cycles, the current circulation cell continued to grow and seemed to reach a quasi-steady state only after about 25 cycles.

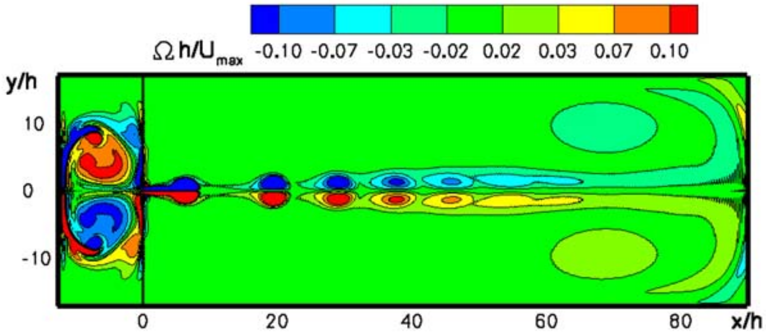

Figure 3.2: Contours of vorticity for 2-D baseline case after 20 cycles ($Re_{jet} = 104.2, St_{jet} = 0.0628$).

3.2 Re_{jet} and St_{jet} Study

The effects of the flow parameters Re_{jet} and St_{jet} were examined by independently varying them about the baseline values. The Reynolds number dependence was examined by maintaining $St_{jet} = 0.0628$ while increasing or decreasing the Reynolds number by factors of four to 26.38 and 416.6 through variations of the kinematic viscosity.

Jet plane properties at different Re_{jet} are shown in figure 3.3(a). At a low Re_{jet}, the edge "horns" of the u velocity disappeared and the profile resembled a flattened parabola. This was a natural consequence of higher viscosity flow dampening the oscillations that induced the distortions in the first place. Conversely, the "horns" were more pronounced for a higher Re_{jet} as the lower viscosity allowed the initial distortions to grow even further. Although not shown, weaker effects were also observed in the spanwise v velocity and vorticity: both profiles showed a slight decrease in the magnitude and the location of peak values moved closer to the centerline of the jet as Re_{jet} decreased.

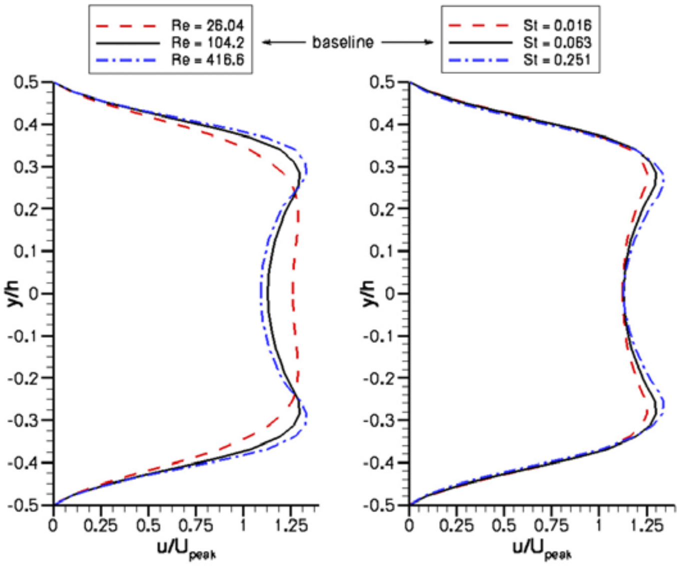

Figure 3.3: Flow streamline velocity at slot plane for ranges of Re_{jet} and St_{jet} at peak blowing.

Reynolds number effects on the external flow are shown in figure 3.4. At very low $Re_{jet} = 26.38$, the vortices formed by ejected fluid dissipated within $20h$ of the aperture without pairing (fig. 3.4(a)). Increasing to $Re_{jet} = 416.6$ allowed the ejected vortices to remain coherent long enough to impact against the far right wall (fig. 3.4(b)) and flow back toward the slit. However, unlike the single, diffuse plume structure of the baseline case, the high Re_{jet} backflow consisted of several pairs of vortices which orbited each other due to mutual induction. These distinct back-flowing vortices also remained strong enough to affect the translational speed (celerity) of nearby centerline vortex pairs. Pairing events between primary centerline vortices were also observed in this simulation but the pairing occurred between individual vortices, rather than through continuous merging of the lead pair. No discernible pattern in the time or location of the pairing was observed throughout 37 full cycles of the force field. The lack of periodicity may be due to the influence of the backflow vortices or to the chaotic nature of the flow in the cavity, which occasionally caused blobs of internal vorticity to be ejected with the fluid. The vortices produced with extra blobs have stronger vorticity and higher celerity.

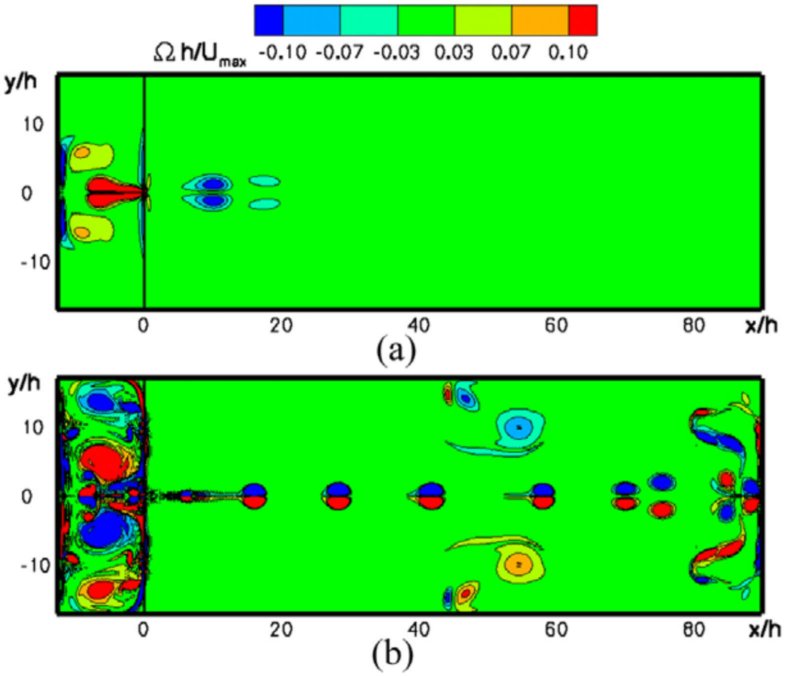

Figure 3.4: Vorticity contours for (a) $Re_{jet} = 28.38$ and (b) $Re_{jet} = 416.6$ after 10 cycles.

Flow within the cavity at the low $Re_{jet} = 26.38$ did not form a circulation cell as vorticity quickly dissipated (fig. 3.4(a)) upon impacting on the piston face. However, at $Re_{jet} = 416.6$, there was complex activity within the cavity (fig. 3.4(b)) which did not appear to become fully periodic even after 37 cycles – the extent of runs performed. Fluid impacting against the piston shed extra vorticity which scooped off more vortices from the solid walls. Those secondary vortices did not dissipate quickly enough and thus continuously added to the complicated picture.

Strouhal number dependency was examined by holding Re_{jet} fixed at 104.2 while varying St_{jet} by factors of four to 0.0157 and 0.2512. A decrease in St_{jet} was obtained by a decrease in frequency with a corresponding increase in period and stroke length L_0. Consequently, as St_{jet} decreased, there was a corresponding increase in the amount of mass ejected through the slot in each half-cycle. In this case, the driving phase of the piston corresponded to an actual displacement of 7.3 gridcells in the x-direction ($1.5h$) or approximately 10% of the cavity depth. In this case, the initial assumption of small piston displacements stated in Chapter 2 may not be applicable here. However, results are still useful in determining quantitative effects of low St_{jet}. Comparisons of the u velocity at the jet plane for different St_{jet} are shown in fig. 3.3(b). Unlike the Re_{jet} study, the flow oscillations were fairly unperturbed by changes in the pulsing frequency and consequently the overall shape of the u-profile at the slit remained largely unchanged. There was only a slight observable tendency to increase the u-velocity magnitude as St_{jet} decreased. Similar small variations were observed in the v-velocity while the vorticity remained mostly unchanged.

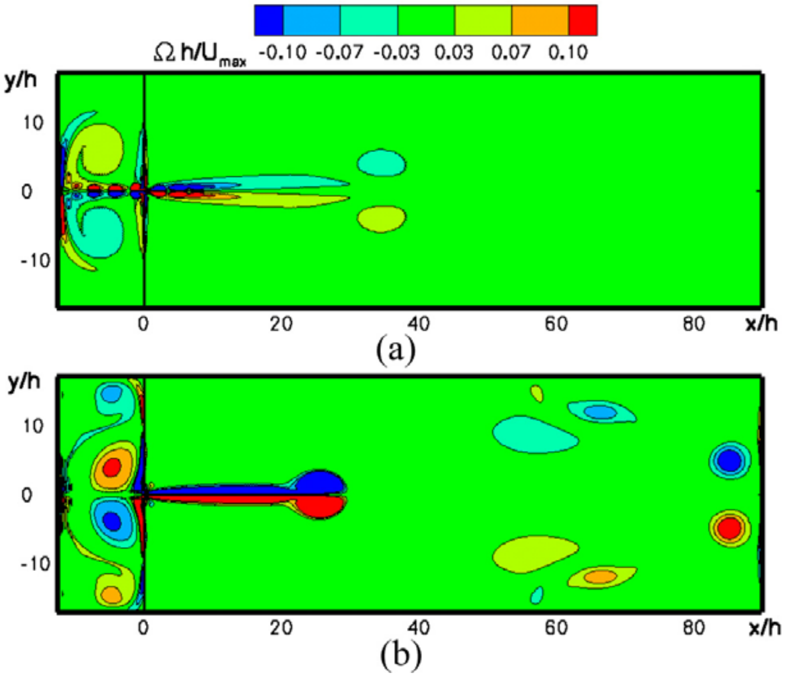

Figure 3.5: Vorticity contours for (a) $St_{jet} = 0.2512$ after 40 cycles and (b) $St_{jet} = 0.0157$ after 10 cycles.

The external flow in figure 3.5 shows that, for a high St_{jet} case (fig. 3.5(a)), a much smaller amount of fluid was ejected per half-pulse. As a result, the ejected vortices continually merged within $O(1h)$ of the jet aperture into a pair of vortex sheets. The vortex sheets dissipated quickly but still feed a faint jet head at $x \approx 40h$ after 40 cycles. The low St case presented the opposite physical effect: the long stroke caused large amounts of fluid to be ejected. As seen in fig. 3.5(b), after 10.5 cycles, the vortex pairs are spaced far apart so that there was no pairing. Individual ejected vortex pairs reached the far wall with little dissipation and flowed back toward the jet aperture while remaining fairly strong and distinct.

Internal to the plenum chamber, the high St_{jet} produced a faint circulation cell. The low St_{jet} case established a circulation cell that, unlike the baseline case, moved in a rough circular orbit and distorted according to the piston motion. As the circulation cell moved about the plenum, extra vorticity was shed by boundaries forming weak secondary circulation cells near the top and bottom of the cavity.

3.3 Geometric Parameters Study

While the flow parameters of interest were mainly the Re_{jet} and St_{jet}, there were many geometric parameters that could be varied in such devices. In this section, the effects of the lip thickness and shape are briefly noted. All studies were performed on the baseline flow parameters of $Re_{jet} = 104.2$ and $St_{jet} = 0.0628$. As seen in the schematic of figure 2.3, lip thicknesses were increased from the thin baseline value up to a throat $2.5h$ thick. For lips $1h$ thick, two additional shapes were tested: a smooth, rounded lip and a cusped lip with sharp edges.

3.3.1 Lip Thickness

A parametric study on the effects of lip thickness was performed by progressively thickening the plate separating the external and internal domains. Figure 3.6(a) shows the effect of thickening the wall on the u-velocity at the outer slit plane. Compared to the baseline case, the "horns" of the profile disappeared for a $1h$ thick wall and the profile was insensitive to walls thicker than $2h$. Thicker walls allowed a boundary layer to develop within the slit, effectively dampening the oscillations that created the profile distortions. The effect was similar to an entry region of a pipe and the overall effect of the boundary layers was to reduce the effective throat height at the exit plane. This increased the peak streamwise velocity, but, since the flow still separated at the sharp corner edge of the lip, there was little change in the v-velocity or vorticity (not shown).

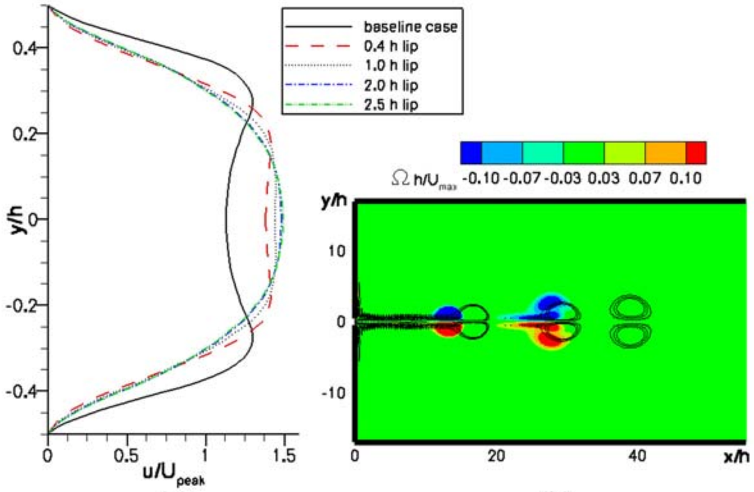

(a) (b)

Figure 3.6: Effect of increasing lip thickness on (a) peak streamwise velocity and (b) vorticity contours after 3 cycles for both the baseline case (color) and *2.5h* thick flat lips (lines).

Vorticity contours of the external flow for the baseline case and $2.5h$ thick lip are shown in fig. 3.6(b). Lines represent vorticity contours for the thick flat lip while colors represent the baseline case at the same instant in time. The thicker lip caused an increase in the celerity of the ejected vortices due to the effectively narrower slit. As a result, vortex pairs generated at the same Strouhal number travel further downstream for the thick lip case as seen in the figure. Pairing events also occurred later and further downstream than for the baseline case. Although not shown, the internal cavity flow was similarly affected by the thicker lips: the vortex pair generated at the first suction cycle had a higher celerity and impacted earlier against the piston face. As a result, the circulation cell created in subsequent cycles was slightly out of phase compared to the baseline case. There was no change, however, in the period or size of the circulation cell since those parameters were set by the period of oscillation of the piston and cavity depth.

3.3.2 Lip Geometry

In order examine the effect of the lip geometry on the flow, two other types of lips are used as seen in fig. 2.3: a smooth, rounded lip and a sharp, cusp-shaped lip. Flow properties at the outer slit plane are shown in fig. 3.7 for the $1h$ thick rounded lip and flat lip. The rounded lip u-velocity profile showed a reduction in the peak distortion and a 20% peak increase when compared to the flat lip. The v-velocity profile was substantially reduced and the peak values occurred closer to the centerline for the rounded lip. Similarly, the peak vorticity for the rounded lip also moved closer to the centerline while presenting a 30% reduction compared to the flat lip. This result was not entirely surprising: the smooth opening of the jet lip partially canceled out the

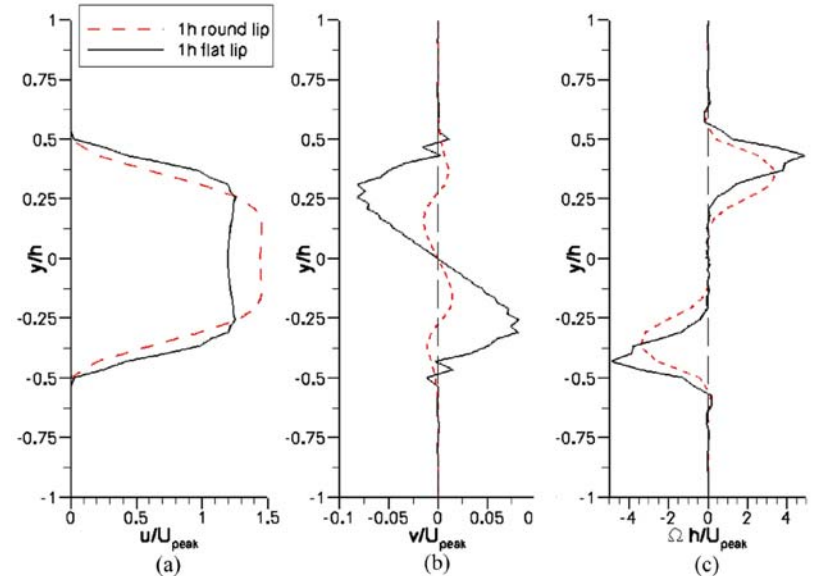

Figure 3.7: Flow properties at outer slot plane for rounded lip and flat lip at peak blowing.

narrowing effect of the growing boundary layer, as seen in the close up vorticity contour and vector plot of figure 3.8. The smooth shape of the lip also explained the decrease in the peak spanwise v-velocity and vorticity. The further absence of “horns” in the u-velocity profile also indicated that such distortions were more affected by lip geometry than thickness, although both geometric parameters contribute to alleviate it. Close examination of the flow near the outer exit plane in figure 3.8 showed a noticeable change in the direction of the velocity vectors. For the flat lip, flow separated and wrapped around the exterior corner of the flat lip (fig. 3.8(a)) resulting on flow deflection and a substantial v-velocity component at the exit plane. In contrast, separation on the smooth lip occurred near the narrowest point of the throat and the gradual opening of the lip allowed the flow to exit the cavity with only a slight flow deflection (fig. 3.8(b)).

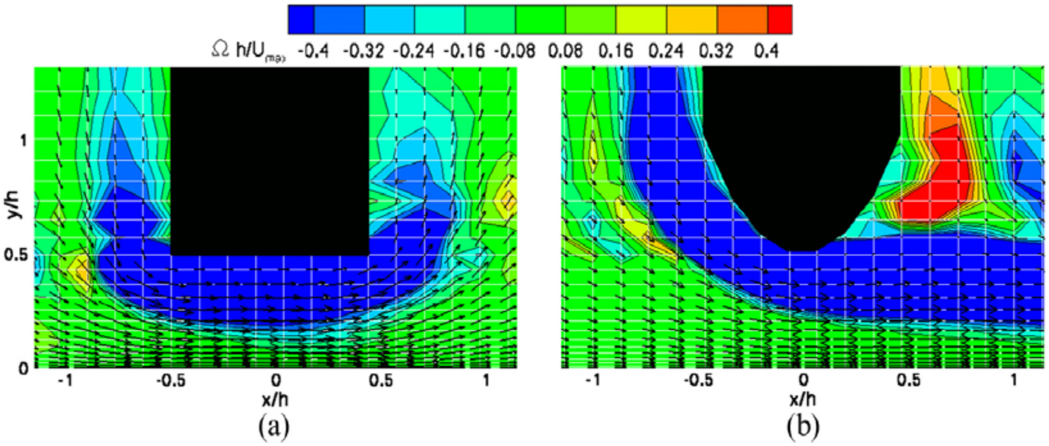

Figure 3.8: Vorticity contours, velocity vectors (black) and computational grid (white) around *1h* thick flat lip and rounded lip at peak blowing.

Although not shown, the cusped lip had a slight increase in the u-velocity compared to the baseline case while the the v-velocity and vorticity were virtually unchanged. This similarity was a result of the cusp providing a sharp edge to induce flow separation much like the original thin walls. As a matter of fact, results for the cusped lip were almost identical to the original thin-walled baseline case, further proving that the horn-like distortions on the u-velocity profile were a result of the particular geometry used. Overall, despite the variations in the u-velocity, different lip shapes did not substantially affect the celerity of the ejected vortices and consequently there were no substantial changes in the external or internal flows.

3.3.3 Size of Domain

Sensitivity of the results to the size of the external domain was studied while keeping the cavity depth at $13h$. Doubling the external domain produced no changes in the jet formation or pairing events for the first several cycles. The same was observed for reductions in the length of the external domain unless an extreme configuration was used. Close inspection of the vorticity near the far wall showed that impacting vorticity blobs did not start to suffer distortion in their shape until within about $5h$ of the wall.

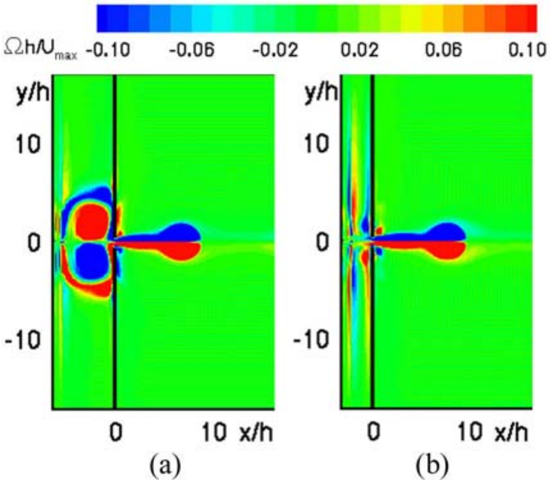

Figure 3.9: Effect of cavity size on cavity circulation cell for (a) half-cavity and (b) quarter cavity at peak blowing.

Sensitivity of the flow to the size of the internal cavity was studied by halving the size of the internal cavity to $^1/_2$ and then to $^1/_4$ of the original baseline case. As the cavity became shallower, the lead pairing event moved further downstream. This result may be understood by examining the cavity flows of figure 3.9. Compared to the baseline case (fig. 3.2), the internal flow of the half-cavity case (fig. 3.9(a)) shows a smaller circulation cell and as the simulation progressed, part of the vorticity was ejected through the slit in each cycle. In contrast, the quarter-cavity case (fig. 3.9(b)) did not even form a circulation cell. Instead, all of the vorticity produced in one cycle was ejected at the following one. The result on the external flow then was similar to the high Re_{jet} case, where the external vortices produced with extra cavity vorticity had higher celerity, which in turn delayed the pairing events.

3.4 Comparison to Experiments

The above flow and geometric parameter studies were next compared to experimental data of Smith and Glezer [36]. Those experiments were performed on a continuously running isolated jet with $2.5h$ thick flat lips and deep, narrow cavities. Flow parameters corresponded to a Re_{jet} of 416.6 and St_{jet} of 0.0628. For comparison, simulation data with the same lip geometry and at the same flow parameters, were accumulated over the last 5 cycles of a 35 cycle run.

Figure 3.10 shows a plot of mean streamwise $\overline{u}$-velocity with respect to spanwise distance y from the centerline at several locations downstream of the jet slit. Also included were experimental data points at approximately the same locations. Normalization factors were the centerline velocity $\overline{U}_{cl}$ and the jet half-maximum width b. As seen in fig. 3.10 and previous numerical studies, all $\overline{u}$-velocity data collapsed well on a single curve showing that the similarity parameters for conventional jets also applied to pulsing jets. However, the current simulation $\overline{u}$ velocity became negative beyond a $y/b \approx \pm 2$. An explanation can be deduced from the averaged streamline plot of fig. 3.11. While the experiments were on a single isolated jet, the present study simulated the effect of an array of jets spaced $17h$ apart. The narrow, 2-D domain caused fluid feeding the centerline jet to be drawn in from above and below so that a mean backflow was created outside of the jet.

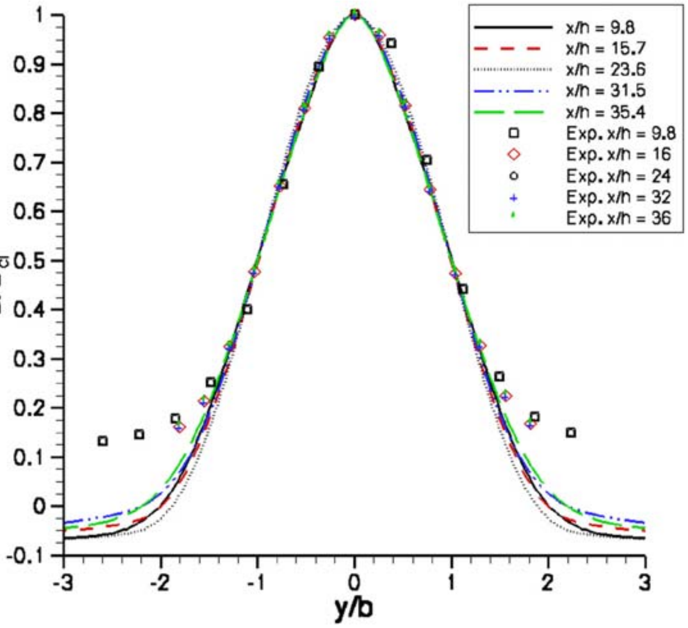

Figure 3.10: Comparison of experimental and 2-D simulation results for mean u velocity vs. spanwise direction ($Re_{jet} = 416.6, St_{jet} = 0.0628$).

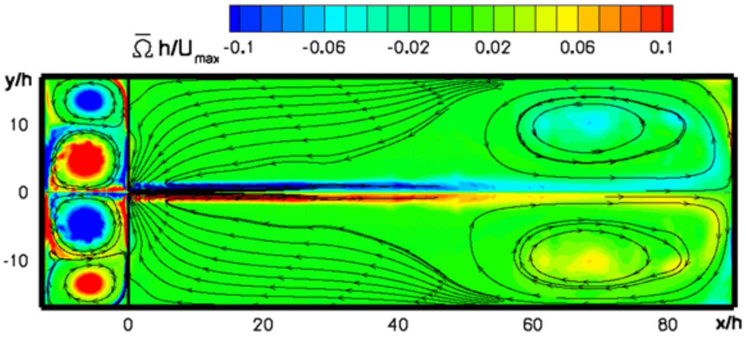

Figure 3.11: Mean vorticity contour and streamlines over 37 cycles for $Re_{jet} = 416.6, St_{jet} = 0.0628$.

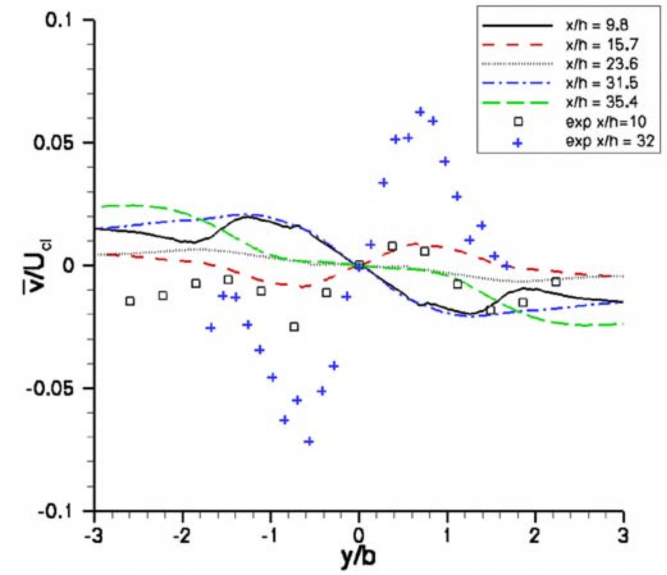

Figure 3.12: Comparison of experimental and 2-D simulation results for mean v velocity vs. spanwise direction ($Re_{jet} = 416.6, St_{jet} = 0.0628$).

Figure 3.12 plots the mean spanwise $\overline{v}$-velocity with the same normalization and against the same variables as fig. 3.10. The $\overline{v}$-velocity values did

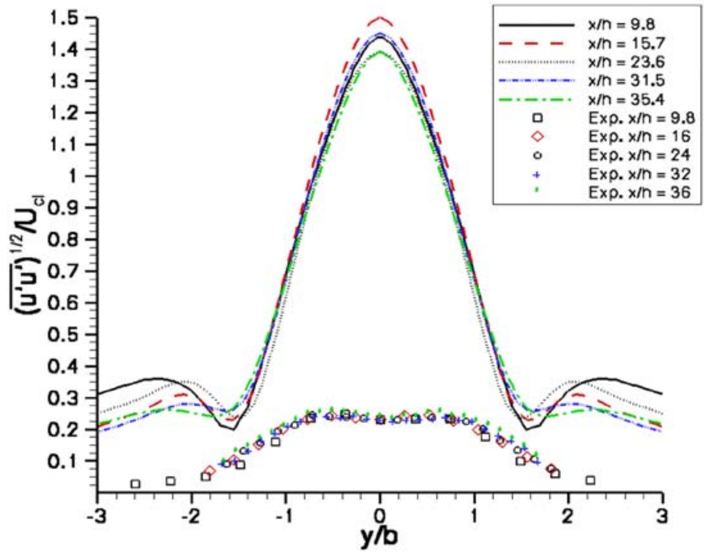

Figure 3.13: Comparison of experimental and 2-D simulation results for streamwise stress vs. spanwise direction ($Re_{jet} = 416.6, St_{jet} = 0.0628$).

not match the experimental data in trend nor magnitude. While the experiments indicated a $\overline{v}/U_{cl}$ variation of as much as 8%, the simulation data were contained in a narrow band of ±2.5%. This can be explained again by fig. 3.11: the periodic nature of the simulation confined the jet to a narrow central band and limited the $\overline{v}$ variation.

Figure 3.13 shows a plot of the normalized mean auto-correlation of the fluctuating u-velocity ($\overline{u'u'}$). Data from the simulation showed fluctuations O(10) times larger than the experimental values. However, this numerical result agreed with the numerical results of Rizzetta *et al.* [47] and was a consequence of the 2-D nature of the simulation, which did not model a breakdown into a 3-D turbulent jet.

Figure 3.14 shows the trajectory of a vortex blob after 26 cycles from both the thin sharp lips and the 2.5h thick flat lips compared to experimental values. The x position was normalized by h and the time by the period of oscillation T. The computational and experimental vortex trajectories diverged far from the jet orifice but agreed for a region $x/h < 8$, before the experimental breakdown into a turbulent jet. Figure 3.15 shows the centerline velocity normalized by U_0 against the position x/h. Again, there was fair agreement between the simulation and the experimental data for a region $x/h < 8$. This further confirmed that although limited to such a small region, the results from this simulation were comparable to experiments.

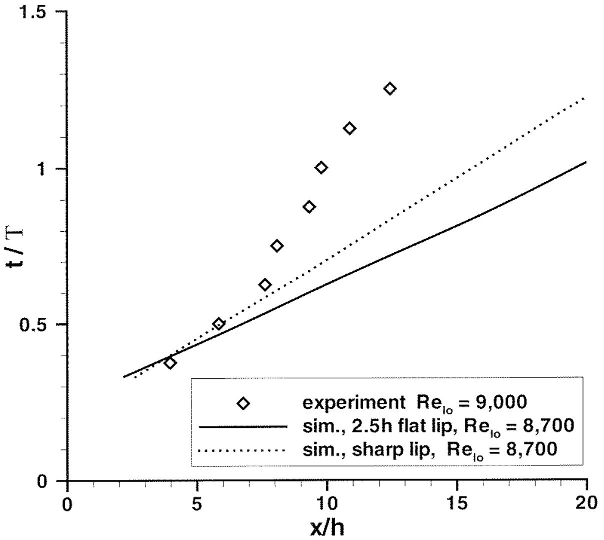

Figure 3.14: Comparison of experimental and 2-D simulation results for vortex trajectories ($Re_{jet} = 416.6, St_{jet} = 0.0628$).

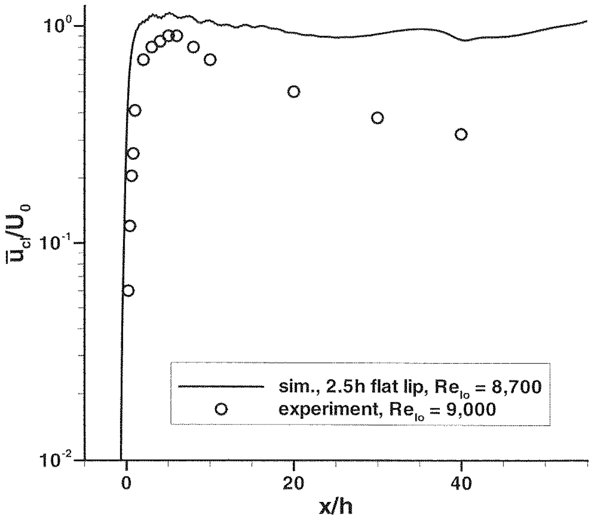

Figure 3.15: Comparison of experimental and 2-D simulation results for centerline velocity ($Re_{jet} = 416.6, St_{jet} = 0.0628$).

3.5 Adjacent 2-D Synthetic Jets

Smith *et al.* [42] also examined the flow of adjacent synthetic jets. In experiments, pulsed jets with the same phase formed two pairs of counter-rotating vortices. However, the two adjacent interior vortices were found to cancel each other so that the overall result was still the formation of a single jet. Out-of-phase pulsed jets resulted in considerable jet steering with the jet becoming attached to the surface for phases higher than 110^o. These results were also confirmed numerically by Kral and Guo [57]. The experiments were performed over a range of Re_{jet} greater than $2,000$ but such values were not possible to replicate with acceptable accuracy with the present method. Therefore, sample calculations were performed at the lower baseline $Re_{jet} = 104.2$ and $St_{jet} = 0.0628$ to examine the capabilities of the current method to model such configurations. As mentioned in the previous chapter, the 2-D domain was modified in a manner similar to the experiments of Smith *et al.* [42] (figure 2.4).

In-phase pulsing is shown in figure 3.17. Similar to experiments, a single vortex pair emerges but as a result of complex interactions between several pulses. However, subsequent vortex pairs were deflected away from the centerline of the domain. This result was caused by a slight asymmetry in the domain geometry due to the even-to-odd ratio of the computational grid and the solid surfaces. Also, the narrow height and the induced backflow of the closed domain noted in fig. 3.11 worked to keep secondary vorticity in the vicinity of the aperture, which further amplified the asymmetry effect. Applying the numerical method to only the top half of the domain with an imposed symmetry plain at the centerline was successful in preventing the resulting jets from drifting off course. This symmetry test confirmed the earlier observation that at this Re_{jet} and St_{jet}, a single vortex pair emerges but only after a complex set of interactions between several pulses. However, since this configuration was unable to produce out-of-phase blowing, the domain of figure 2.4 continued to be used.

Pulsing the jets 60^o out of phase did not produce any expected jet steering as shown in figure 3.17 after 4 cycles. The narrowness of the domain and the periodic nature of the simulation created a complex system of mirror vortices from the onset that severely affected the flow. Subsequent pulses simply added more vorticity within the near slot region so that a coherent picture of motion did not emerge even after 10 pumping cycles.

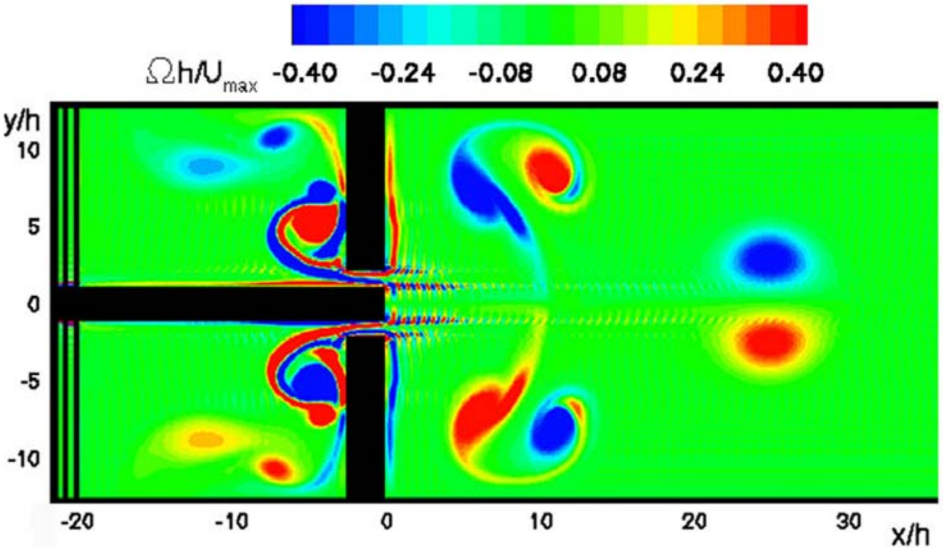

Figure 3.16: Contours of vorticity for adjacent jets pulsed in-phase after 4 pumping cycles ($Re_{jet} = 104.2, St_{jet} = 0.0628$).

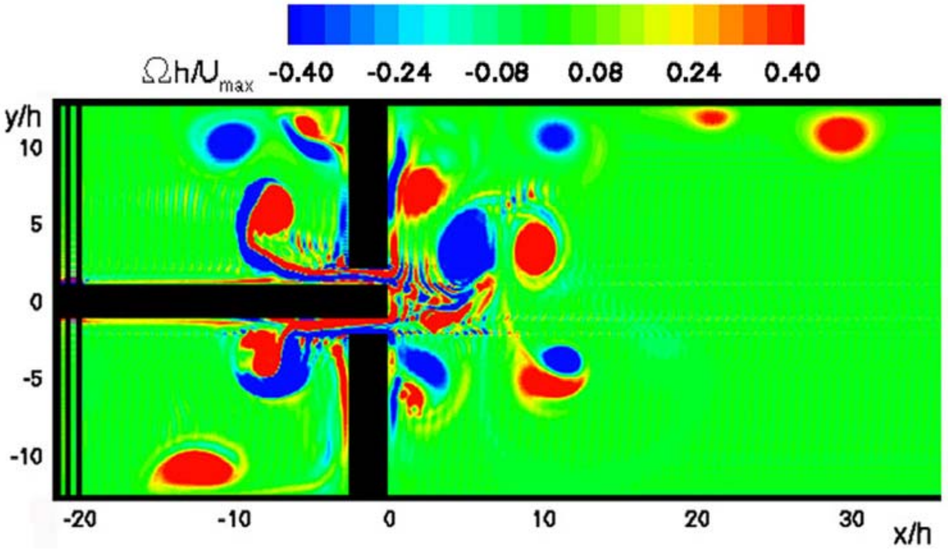

Figure 3.17: Contours of vorticity for adjacent jets pulsed 60^o out-of-phase after 4 pumping cycles ($Re_{jet} = 104.2, St_{jet} = 0.0628$).

Chapter 4

3-D Simulation Results

The results from the 2-D simulations showed that the virtual force field method was capable of simulating the internal structure of synthetic jets with moderate Re_{jet} and St_{jet} similar to the devices used by Smith *et al.* [37], Crook *et al.* [38] and others for flow separation suppression on bluff bodies. For our flow conditions, the simulations were validated against experiments in the near field region within 8 slot widths from the jet aperture. Those results were of particular importance for the 3-D simulations conducted in this chapter. Boundary layer flow control experiments by Rathnasingham [50] operated actuators at low Re_{jet} and a resonant St_{jet} which fell within the range of parameters tested in the 2-D study. Furthermore, as pointed out by Gad-El-Hak [11], streaks and streamwise vortices, which usually remain within $y < 50l^*$ of the surface, ought to be the primary targets of actuation. These structures lie at a distance within the validation region of the 2-D simulations and thus, the same modeling method used in the 2-D study can be applied to accurately create the internal structure and near flow field of 3-D slot jets embedded in a channel.

As described in Chapter 2, the 3-D domain of figure 2.5 has a different orientation than the 2-D simulations of figure 2.2. The $x-$streamwise direction in the 3-D simulations is the direction of mean channel flow and the jets blow in the $y-$direction, normal to the walls of the channel. Figure 4.1 illustrates the type of structures encountered in turbulent channel flow which can be targeted for actuation. Enstrophy iso-surfaces ($\mid \vec{\Omega} \mid$) are shown in orange while streamwise vorticity (Ω_x) contours are shown as red/blue "worms." Both quantities are normalized by a viscous time equal to the viscous length scale divided by the friction velocity ($t^* = l^*/u^*$). As the Ω_x "worms" translate over the surface, lower speed flow is brought up on the upwash side of the vortex while higher speed flow is brought down on the downwash side. As noted by Smith and Walker [4] and in Jiménez and Pinelli [8], this mechanism was responsible for creating low and high-speed streaks on the surface, respectively. In terms of enstrophy contours, figure 4.1 shows that the downwash of higher speed fluid, i.e. a high shear stress region, appears as flat "pancake" structures sliding over the wall. Time evolution of the flow also showed that some "pancake" structures developed lifting tendrils which dissipated and left behind new "pancake" structures. Thus "pancake" structures also signaled the locations of a bursting event of wall-layer fluid and subsequent formation of secondary vorticity at the wall. This demonstrated that "pancakes" could also be considered adequate targets for actuation in addition to the streamwise vortices and streaks.

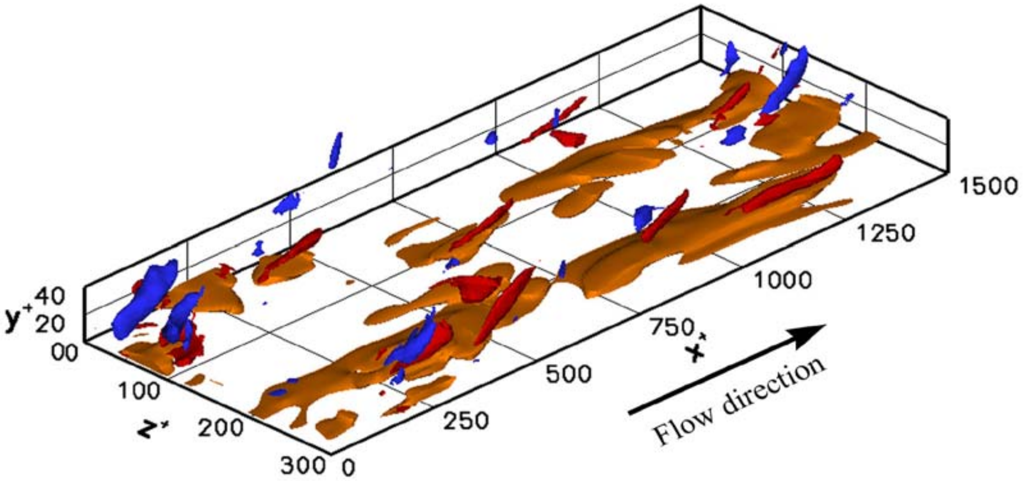

Figure 4.1: Channel flow with orange iso-surfaces of enstrophy and red/blue streamwise vorticity worms ($\Omega_x l^*/u^* = \pm 0.4$, $\mid \vec{\Omega} \mid l^*/u^* = 2$).

4.1 Effect of the Inactive Devices

The new geometry of a plate with four slots first had to be tested with the devices inactive to determine the extent and nature of possible interactions of the configuration with the channel flow. For example, compared to the rest of the surface, inactive slots are essentially holes on the plate and should behave as low-shear zones. Also the square lips of the slots provided sharp corners which might either generate flow structures or affect pre-existing ones as they translate over the devices. To study the extent and nature of the interactions between the slots and the channel flow, a previous turbulent channel flow was used as the starting condition of the simulation. The new geometry as seen in figure 2.5 with the virtual plate and internal structure for four slots was inserted abruptly and the simulation allowed to run for $85,000$ $(2,500t^*)$

time steps to stabilize once more. The $Re_{channel}$ and R^* of the 3-D domain were then approximately $2,000$ and 110, respectively. Although the slots and their internal structure were present, no time-varying force was applied at the membranes. Instead, the membranes were defined as solid, no penetration walls underneath the surface and the slots were left to behave simply as holes cut in the plate.

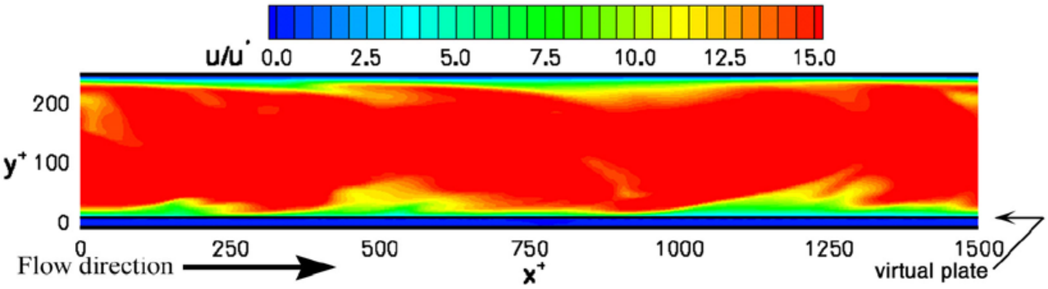

Figure 4.2: Instantaneous contours of u-velocity on a $xy-$plane through the center of the channel.

Instantaneous contours of streamwise velocity (u) on an $xy-$plane through the channel in figure 4.2 show that a new boundary layer develops over the virtual plate. The presence of the slots is suggested on contours of normal velocity (v) on an $xz-$plane $4l^*$ above the virtual plate (fig. 4.3). These velocity traces directly over the slots are likely a result of the interaction of buffer layer vortices with the sharp edges of the slots creating weak eddies in the slots.

Despite such occasional instantaneous interactions, flow properties averaged over the next $60,000$ time steps ($1,760t^*$) showed no mean effects of the presence of the slots. The calculated ratio of drag on the slotted plate divided

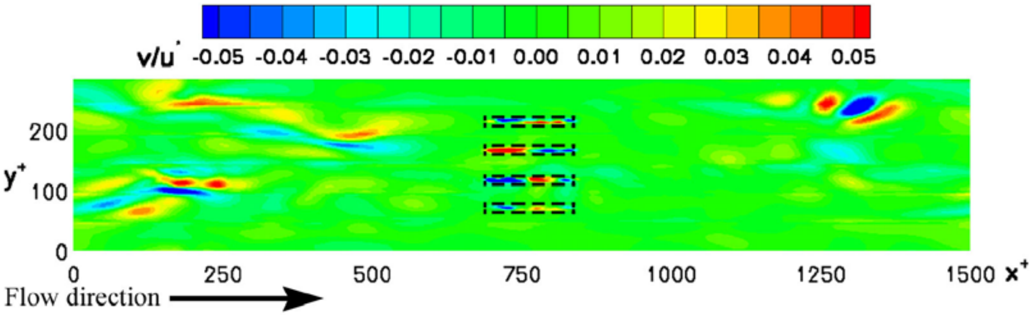

Figure 4.3: Instantaneous contours of v-velocity $4l^*$ above the virtual surface. Note weak interaction of flow with slots at the center as flow dips slightly in and out of the slots.

by the drag on the opposing boundary was of 1.004 ± 0.06 over 5 independent realizations with a 90% confidence interval. This result suggested that the narrow, high aspect ratio slots were low profile and, when inactive, would not impact the flow negatively.

4.2 Pulsed Jet Operation in the Absence of Channel Flow

In addition to determining the effect of the inactive devices on the channel flow, another important element of the parametric study was to examine the 3-D performance characteristics of the slot jets when operating without the bulk flow. Similar to the flow parameter studies of the 2-D jets, detailed knowledge of the jet structure was important to determine which types of actuation could have a positive effect on the boundary layer, i.e. stabilization of low speed streaks or lifting of high shear stress areas. To this end, a simulation was run with no mean gravity force acting down the channel and an initially quiescent flow. A smooth periodic sinusoid was applied as the normal velocity of the membrane as indicated by the schematic on figure 4.4 (top). Given the construction of the devices, which coupled each pair of jets 180^o out-of-phase, two modes of actuation were tested: "-++-," in which the jets were initially operated with in-phase blowing out of the two center slots and "-+-+" with alternating blowing and suctioning slots. In both modes, the jet area-averaged velocity at peak blowing was $7.5u^*$ and the period of actuation was $T = 30t^*$. The corresponding Re_{jet} for this case was 34, considerably larger than what was considered likely necessary for boundary layer control. For example, flow control experiments by Rathnasingham [50] made use of slot jets with average blowing velocities of $O(1u^*)$ and corresponding device Re_{jet} of O(10). The larger Re_{jet} in this part of the present study was used to make obvious the jet structure; later runs involved jet strengths of lower magnitudes closer to those of turbulent boundary layer fluctuations (1 to $3u^*$).

Results for the "-++-" mode are shown in figure 4.4(a) and (b) at two instants 180^o out of phase. Figure 4.4(a) shows contours of normalized Ω_x vorticity on a $zy-$plane through the center of the slots after 4.5 pumping cycles. Half a cycle later, the contours have evolved to those shown in figure 4.4(b). Even though there is no mean channel flow, data are normalized according to the slot width and the centerline channel velocity taken from the baseline case to match the contours of previous figures. Black lines represent stationary solid boundaries while white lines represent the moving virtual membrane. The col-

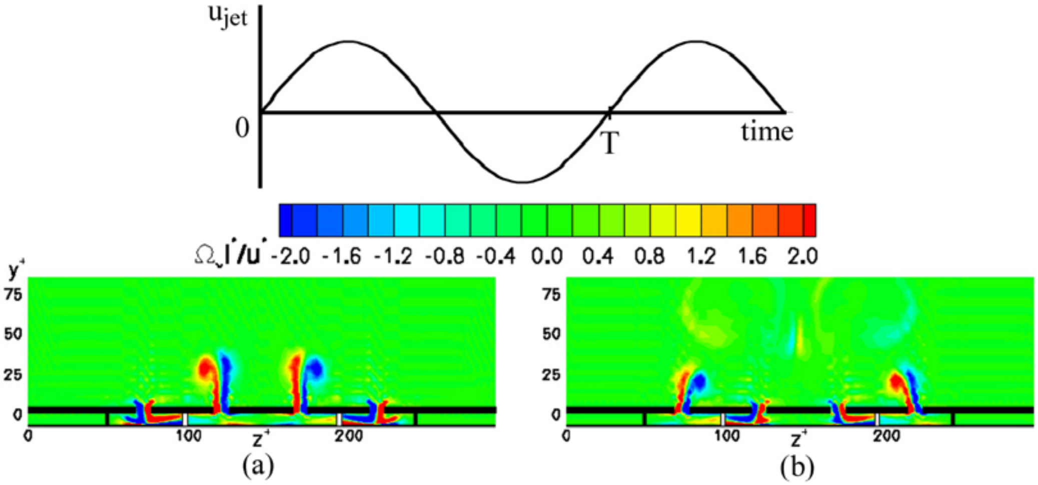

Figure 4.4: Schematic of jet actuation cycle and contours of enstrophy on a $zy-$plane through slots and actuators at (a) peak blowing of center slots and (b) peak blowing of outer slots.

ors are saturated to enhance contrast and, as a result, Gibbs phenomena from large flow gradients around the slot lips are highlighted as well. Similar to the 2-D results, the blowing jets are still comprised of two counter-rotating vortices which propagate to a considerable height upward before dissipating. However, the 3-D slot jets are closely spaced and the $zy-$plane contours reflect that proximity. For central blowing (fig. 4.4(a)), the jets have a tendency to move apart due to the proximity of the two sets of similar vortical structures and the outboard suction. As the jets continue to operate and reverse direction, the outward blowing jets are, in response, also drawn slightly toward the center (fig. 4.4(b)). Vorticity generated during the inflow, as fluid is drawn into the cavity, quickly dissipates against the internal walls of the cavity and the pumping membrane without forming quasi-steady circulation cells. The evolution of the jet structure away from the plate was affected by the start condition of the jets. Blowing jets produced in the first half of the pumping cycle ($t = 0$ to $T/2$) remained coherent up to about $150l^*$ above the plate. As the microjets continued to operate through later cycles ($t > T/2$), subsequent vortex cores tended to be confined to, or diffused away, within $100l^*$ above the plate. This difference was believed to be a result of the starting condition of the simulation: while the first pulse discharged into quiescent fluid and was free to translate upward under self-induced motion, subsequent pulses encountered leftover vorticity from previous cycles that affected their trajectory and dissipation rate.

Figure 4.5 shows iso-surface contours of enstrophy ($| \vec{\Omega} |$) in the channel below $y^+ = 40$ after 0.5 pumping cycles (a) and half a period later (b). The coordinates are shifted so that the virtual plate containing the four slots corresponds to the bottom plane of the figure ($y^+ = 0$). A previous numerical study by Rizzetta *et al.* [47] determined that the 3-D slot jet begins as a rectangular ring vortex composed of the vortex sheets created by fluid separating at the outer edges of the slot. As the jet evolved, Rizzetta *et al.* [47] noted that the 3-D jet evolved in to a form resembling a "bread loaf." Here, however, figure 4.5(a) shows that the evolved jet structure has thick, bulbous ends. This enhanced outflow near the slot ends was likely a result of the shallow cavity and elongated driving membrane: since the membrane was longer than the slot, more fluid was squeezed out near the ends of the slot resulting in the distorted jet shape whether the slots are in center blowing (a) or outer blowing mode (b). Although not shown, similar end distortions were also observed in the "-+-+" operating mode.

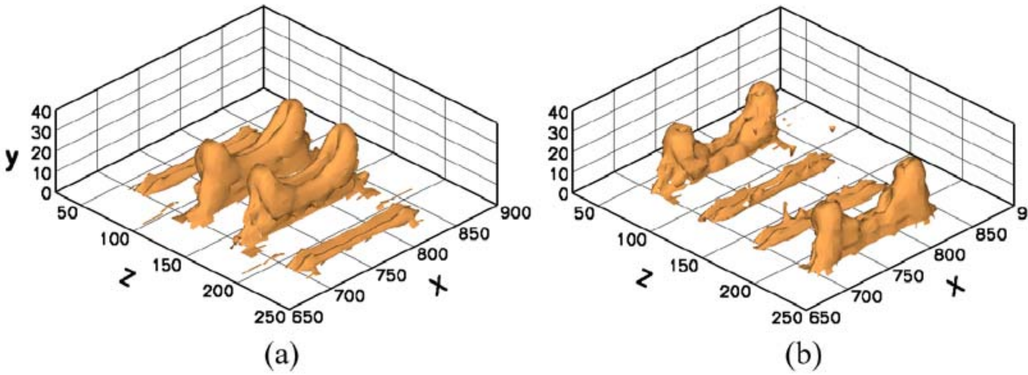

Figure 4.5: Iso-surfaces of enstrophy at (a) peak blowing of center slots and (b) peak blowing of outer slots.

4.3 Quasi-Steady Actuation into a Turbulent Boundary Layer

Next, the simulations of the "-++-" mode and its opposite, "+−−+," were combined with a mean channel flow and a fully developed turbulent boundary layer over the virtual plate. The membranes were set to undergo motion having a half-square wave amplitude so the jets would only blow in one direction as shown schematically in figure 4.6(a). The jet had an area averaged normal velocity of $1.8u^*$ at the slot plane during membrane motion for a corresponding Re_{jet} of 8.2. This blowing strength was four times weaker than in the previous section but was on the same scale as in the experiments of Rathnasingham [50]. The period of oscillation (T) was 176 times larger than the viscous time scale t^*, giving a St_{jet} of 0.11 and making the actuation quasi-steady at any given point in the cycle.

Figure 4.6(b) shows contours of instantaneous streamwise u-velocity on a $zy-$plane through the slots while the slots are blowing in "$+--+$" mode. It can be seen that fluid sucked into the cavity retains some streamwise momentum even below the surface while ejected fluid comes out with negligible streamwise momentum. This suggests that modeling real actuators for turbulent boundary layer control with simple wall-normal boundary suction/blowing, such as in Kral *et al.* [45], is not an adequate representation of the performance of the devices.

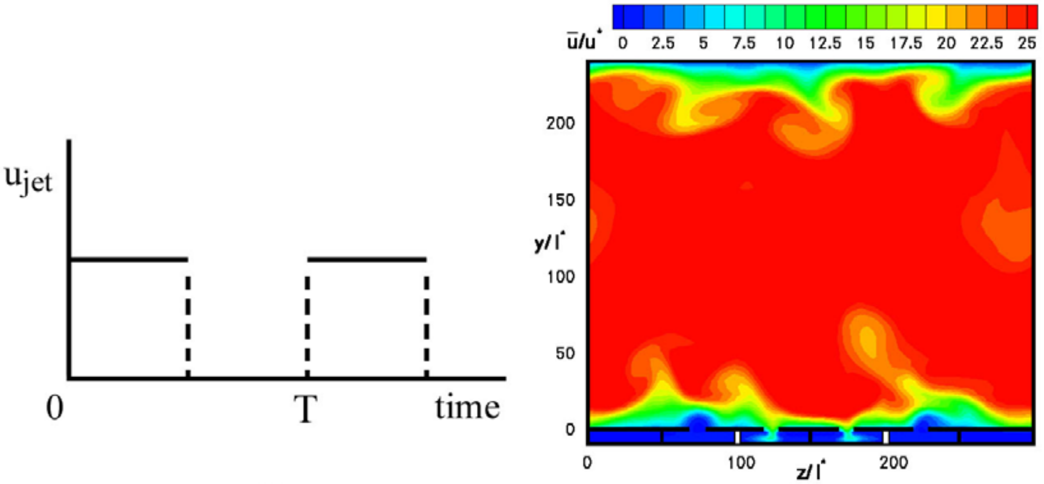

(a) (b)

Figure 4.6: (a) Schematic of jet actuation cycle and (b) instantaneous contours of streamwise u-velocity on a zy-plane through the slots in "$+--+$" mode (flow direction into the figure).

Figure 4.7 shows iso-surfaces of red/blue Ω_x "worms" $352t^*$ (2 cycles) after activation of the slots in "-++-" mode. The abrupt start of the devices just before the instant in time depicted in the figure generated a fair amount of vorticity, seen as the large rising plumes of Ω_x. However, as the jets continued to operate through the long activation period, vorticity production decreased and settled at a lower, steady value with the jets themselves became confined to the viscous sublayer. While the initial vorticity production may be a result of the initial blow up of fluid issuing from the slots, it may also be a result of oscillations in the force field method due to the step-like function used to drive the flow.

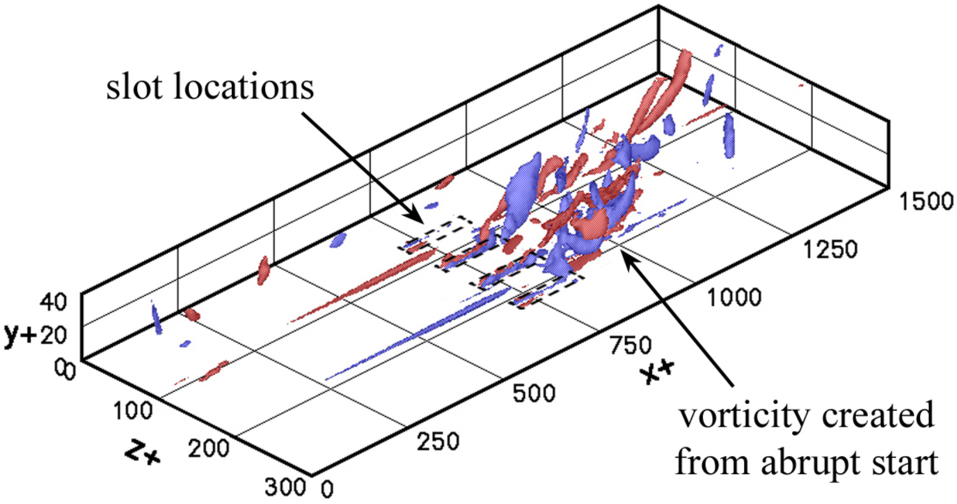

Figure 4.7: Iso-surfaces of $\Omega_x l^*/u^* = \pm 0.4$ for "-++-" mode after $352t^*$ (2 cycles).

Time averaged results of the streamwise velocity over a total time of $8T$ for both the "-++-" and "$+--+$" modes are shown in figures 4.8 and 4.9, respectively. Data are time averaged and mirror averaged over the center $xy-$plane of the channel. Contours of $\overline{u}/u^*$ are shown on an $xz-$plane $4l^*$ above the surface and on $zy-$planes through the middle of the slots at $x = 750l^*$ and at two stations downstream ($x = 1,000l^*$ and $x = 1,250l^*$). As seen on the $xz-$plane of figure 4.8 the quasi-steady operation of the "-++-" mode led to the formation of low-speed streaks directly over the blowing slots while high-speed streaks formed over the suctioning slots. A similar pattern can be seen for the "$+--+$" in figure 4.9. The $zy-$plane contours at $x = 750l^*$ show that, for both actuation modes, the blowing jets are confined to a height of $y < 20l^*$ while the suctioning jets removed most of the slowest moving (blue) fluid near the plate. Further downstream at $x = 1,000l^*$ and $x = 1,250l^*$, the jet structures have mostly dissipated but small fluctuations in the thickness of the viscous sub-layer still remain. The blue, slow moving layer of fluid near the plate is thicker over spanwise locations corresponding to the blowing slots and vice-versa. Such effects of actuation can also be seen in the buffer layer as yellow "ridges" and "valleys" of streamwise velocity centered around heights of approximately $25l^*$ at both $x = 1,000l^*$ and $x = 1,250l^*$. The vector field, also shown on the $zy-$planes of figures 4.8 (a-c) and 4.9 (a-c), indicate the presence of two persistent pairs of streamwise vortices with cores at heights varying from $25l^*$ to $50l^*$ above the plate. The vortex pairs are a result of the quasi-steady modes of actuation as fluid ejected from one slot is displaced in the spanwise direction and drawn into a neighboring, suctioning slot. The vortices' upwash and downwash regions correlate to the location of the "ridges" and "valleys" of streamwise velocity on the $zy-$planes, respectively. Moreover, the locations of the vortex pairs are also consistent with the streak locations on the $xz-$plane, suggesting that the vortices produced by the quasi-steady actuation can persist throughout much of the $1,500l^*$ length of the domain.

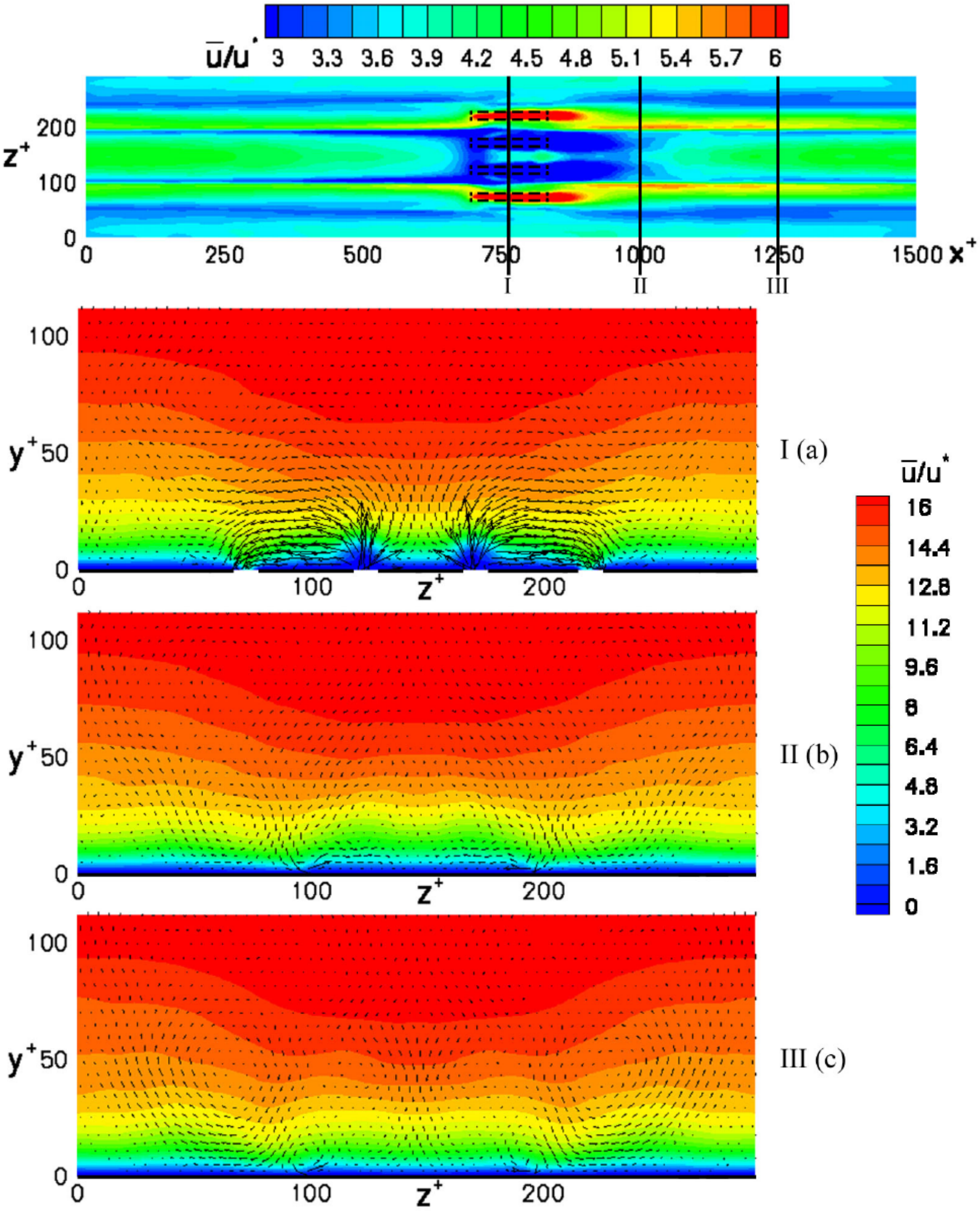

Figure 4.8: Time-averaged contours of u velocity for "-++- mode on xz-plane $4l^*$ above the virtual surface and on zy-planes at: (a) $x = 750l^*$, (b) $x = 1,000l^*$ and (c) $x = 1,250l^*$ (note different color bars).

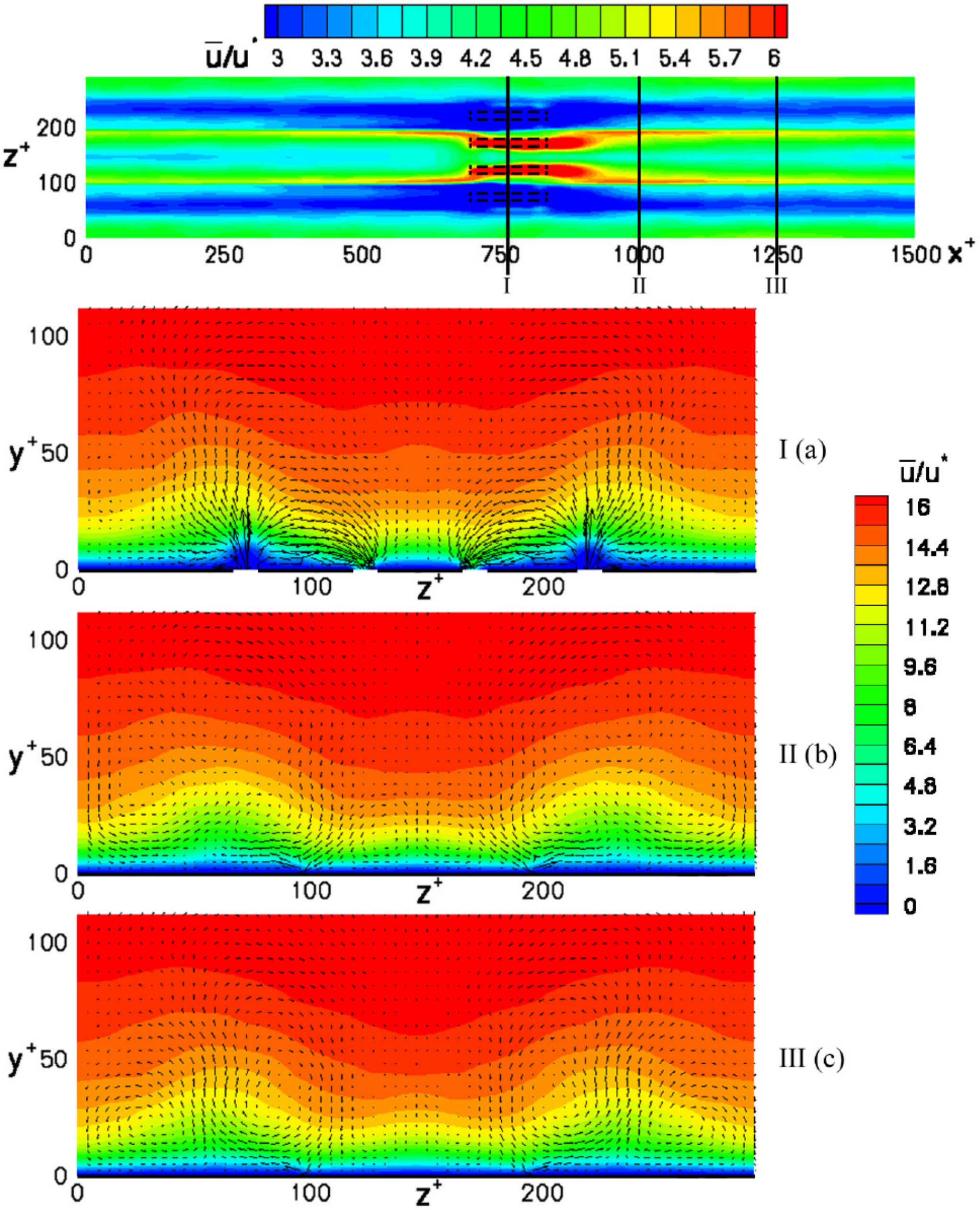

Figure 4.9: Time-averaged contours of u velocity for "$+--+$" mode on xz-plane $4l^*$ above the virtual surface and on zy-planes at: (a) $x = 750l^*$, (b) $x = 1,000l^*$ and (c) $x = 1,250l^*$ (note different color bars).

4.4 Periodic Pulsed Actuation

As noted by Gad-El-Hak [11], flow control potential is related to the ability to manipulate turbulent boundary structures near the wall that are directly or indirectly responsible for higher levels of shear stress. The quasi-steady operation of the previous section indicated that such type of open-loop actuation could alter the streak pattern on the surface. It is possible then, that the same high aspect ratio MEMS devices could also be used to directly or indirectly manipulate other near-wall structures such as streamwise vortices. For example, in-depth analysis by Koumoutsakos *et al.* [26] reported large drag reductions associated with the manipulation of streamwise vortices. Flow structures such as streamwise vortices in close proximity to the wall induced a natural vorticity flux normal to the surface. By using a continuous distribution of sources and sinks, Koumoutsakos *et al.* [26] enhanced the vorticity flux at the wall, leading to the separation of pairs of streamwise vortices near the surface and an overall stabilization effect on the boundary layer. If such a method is to be duplicated with discrete actuators, the devices themselves must be able to generate vorticity through their operation in order to produce a vorticity flux coming off the wall. Obviously, jet strength has a direct effect on the vorticity production. But results from the quasi-steady actuation also showed that more vorticity was produced at the start of pulses rather than with steady operation. Thus, operating the jets at a higher device Re_{jet} and with higher frequency pulses should yield both an increased vorticity production and further insight into how such devices may be used for control of streamwise vortices.

Studies of the effect of smooth periodic actuation on a turbulent boundary layer were performed by imposing a time-varying sinusoidal velocity on the driving membranes of the actuators. The actuation modes tested were the "-++-" and "-+-+." The period of oscillation (T), in which a given slot went through a full cycle of blowing and suctioning, corresponded to approximately $30t^*$. The pulses were not expected to be fully independent of each other since the channel flow-through times at the centerline of the channel or even at the height of streamwise vortices ($y^+ \approx 15$) were only $90t^*$ and $150t^*$, respectively. The pumping membrane was set to generate a modestly strong jet of area-averaged peak normal velocity corresponding to $3u^*$ for a Re_{jet} of 13.6 and a St_{jet} of 0.33. These values were at the upper limit of jet strength expected to be useful for turbulent boundary layer control.

Instantaneous results are illustrated with iso-surfaces of enstrophy for the "-++-" mode in figure 4.10, half of a period after actuation started. As seen in the figure, blowing jets appear as billowing enstrophy structures in contrast to the large, elongated natural "pancake" structures of the boundary layer. The suctioning outer slots are seen as rough rectangular gaps of enstrophy outlined by the vortex layer created by strong shear along the slot lips. As the jet plume rises into a higher momentum flow and is subjected to shearing forces, the end distortions roll up into hairpin vortices, as illustrated in the inset figure where the effect is particularly evident on the leading edge portion of the jet. As the simulation was allowed to continue, the lead hair-

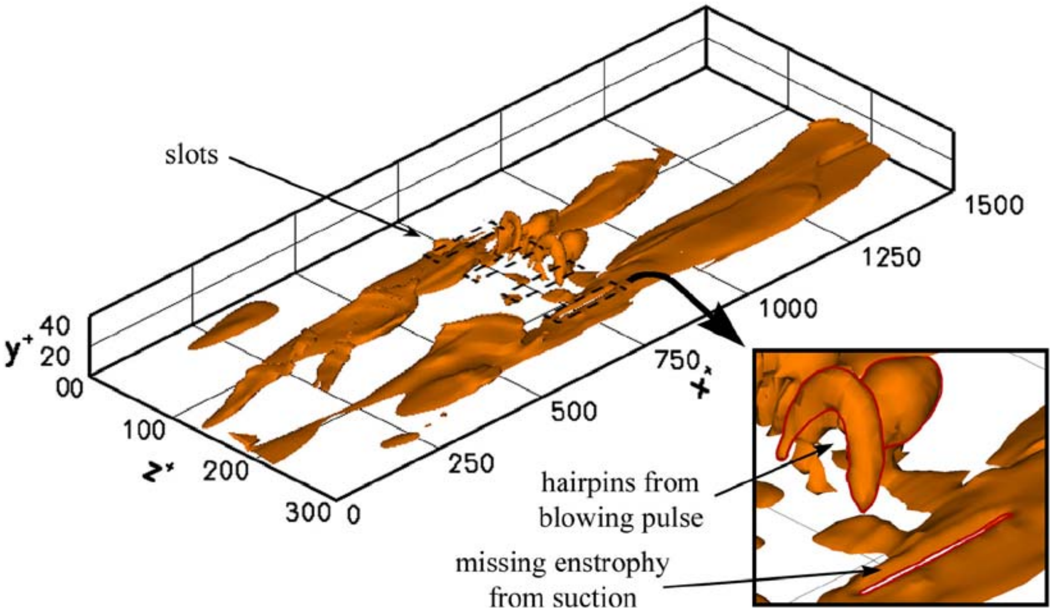

Figure 4.10: Contours of enstrophy for periodic "-++-" actuation and close-up of flow near a blowing/suction slot pair.

pin appeared flatter and more stretched than the shielded trailing hairpins. Subsequent observations of this mode and the "-+-+" mode showed that the leading edge hairpin dominated, sometimes overtaking and swallowing weaker hairpins or leap-frogging over the trailing edge hairpin. Regardless of its evolution, the leading edge hairpin interacted with the boundary layer structures and spawned several other pancake structures and occasional lifting tendrils. This is illustrated in figure 4.11 and its inset, two periods ($60t^*$) after the time frame shown in figure 4.10. The jets themselves only remained coherent up to $50l^*$ above the virtual plate and $200l^*$ downstream of the location of the slots before breaking down into other structures. While the jets dissipated quickly,

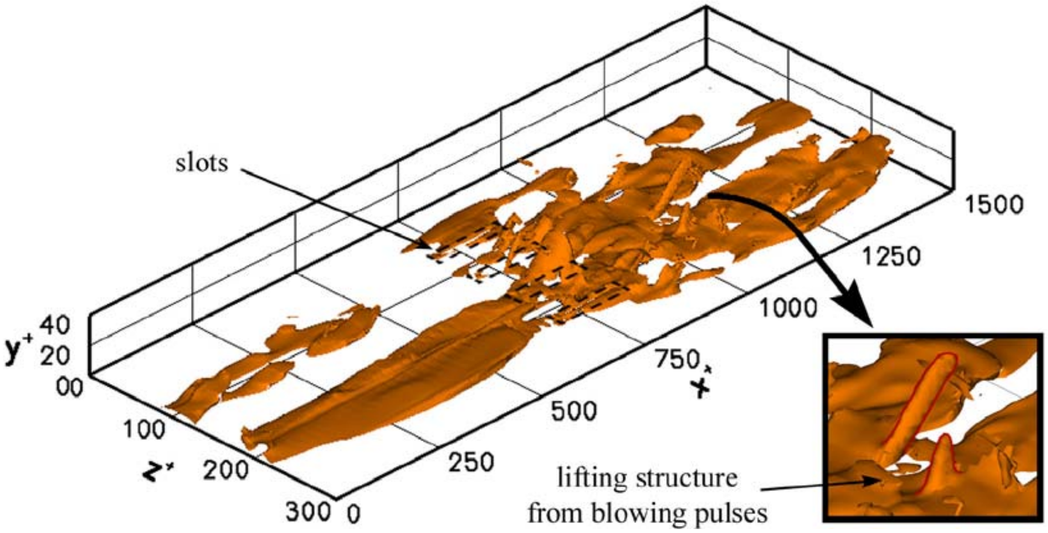

Figure 4.11: Contours of enstrophy for periodic "-++-" actuation and close-up of downstream flow structures 2 cycles after the time frame of fig. 4.10.

their effects remained in the altered evolution of the pancake boundary layer structures as far as $1,000l^*$ downstream.

Data were time averaged over $80,000$ time steps (80 full pumping cycles) and the results are shown in figures 4.12 and 4.13 for the "-++-" and "-+-+ modes, respectively. Both figures show contours of streamwise velocity on a $xz-$plane $4l^*$ above the surface as well as $zy-$planes through the middle of the slots at $x = 750l^*$, and further downstream at $x = 1,000l^*$ and $x = 1,250l^*$. Results were also averaged over the center plane of the channel for the "-++-" mode but not for the '-+-+ mode since it lacked the same convenient symmetry. For both actuation modes (fig. 4.12 and 4.13), the $xz-$plane shows low-speed streaks developing ahead of the two center slots and to the outside of the outer slots. Considerable flow mixing can be seen over the slots as the streak pattern is disrupted. This disruption extends $300l^*$ downstream of the actuators as indicated by the elongated spots of higher speed fluid. However, for the "-+-+" mode, the center low-speed streak does not clearly reform downstream of the actuators. In contrast, for the "-++-" mode, the low speed streak quickly reappears a few slot widths downstream of the actuators. The $zy-$plane through the slots at $x = 750l^*$ shows a pattern of "ridges" in the streamwise velocity over each slot location. These "ridges" are consistent with the characteristics of synthetic jets having zero-net mass flux but non-zero momentum and impulse along the line of actuation. Alternatively, since the jets draw in high streamwise momentum fluid and eject low momentum fluid, they simply may be acting as small protrusions off the surface or as drag-producing devices. At $x = 1,000l^*$, the effect of actuation has mostly coalesced into two wide "valleys" corresponding to the spots of higher speed fluid seen downstream of the actuators. Further downstream at $x = 1,250l^*$, the flow has mostly re-equilibrated to reflect the overall streak pattern seen on the $xz-$plane. Examination of the vector field for the "-++-" case at $x = 1,000l^*$ show several mean pairs of streamwise vortices over the slots. In particular, there is a strong vortex pair over the center slots which is likely responsible for re-forming the centerline low-speed streak shortly downstream of the actuators. A secondary vortex pair can also be seen to the outside of the outer slots and is associated with the second low-speed streak at edge of the domain. The "-+-+" mode at $x = 1,000l^*$ show a similar pair of mean streamwise vortices at the edges of the domain, where a strong low-speed streak is clearly seen. Elsewhere, the "-+-+" mode shows several individual vortices with cores at heights varying from $15l^*$ to $50l^*$. The lack of clearly delineated vortex pairs is likely responsible for preventing the center low-speed streak from quickly reforming.

Regardless of the actuation mode, it is clear that periodic pulsing of the actuators resulted in strong vertical mixing. This result ultimately affected the average drag ratio calculated over the same time interval as the figures. The "-++-" mode resulted in a drag increase of 16% ± 5.1% with a 90% confidence interval over 7 independent realizations. The "-+-+" had a similar drag increase of 16%±2.0% with a 90% confidence interval over 18 independent realizations.

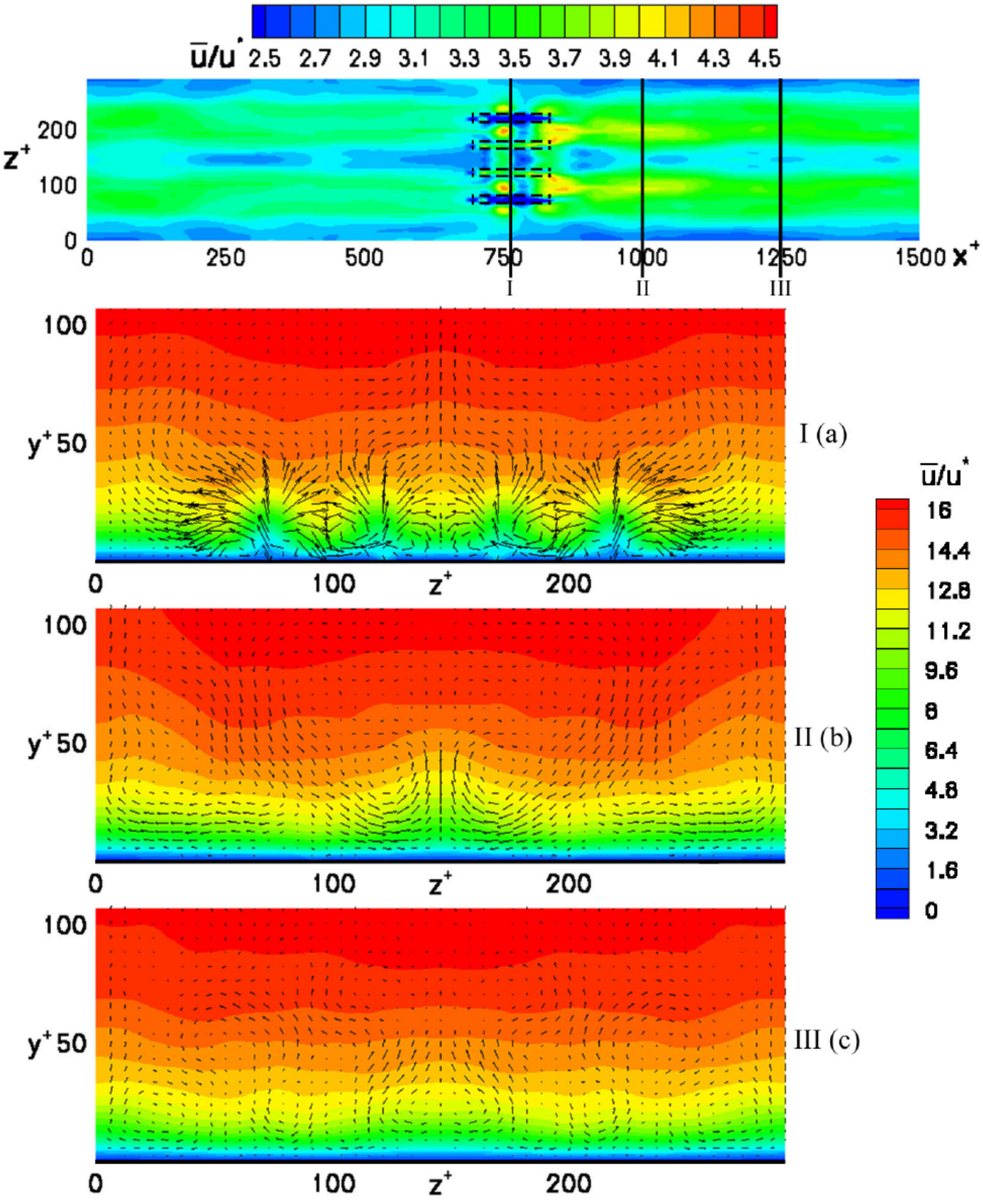

Figure 4.12: Time-averaged contours of u velocity on $xz-$plane $4l^*$ above the virtual surface for "-++-" mode and on $zy-$planes at: (a) $x = 750l^*$, (b) $x = 1,000l^*$ and (c) $x = 1,250l^*$ (note different color bars).

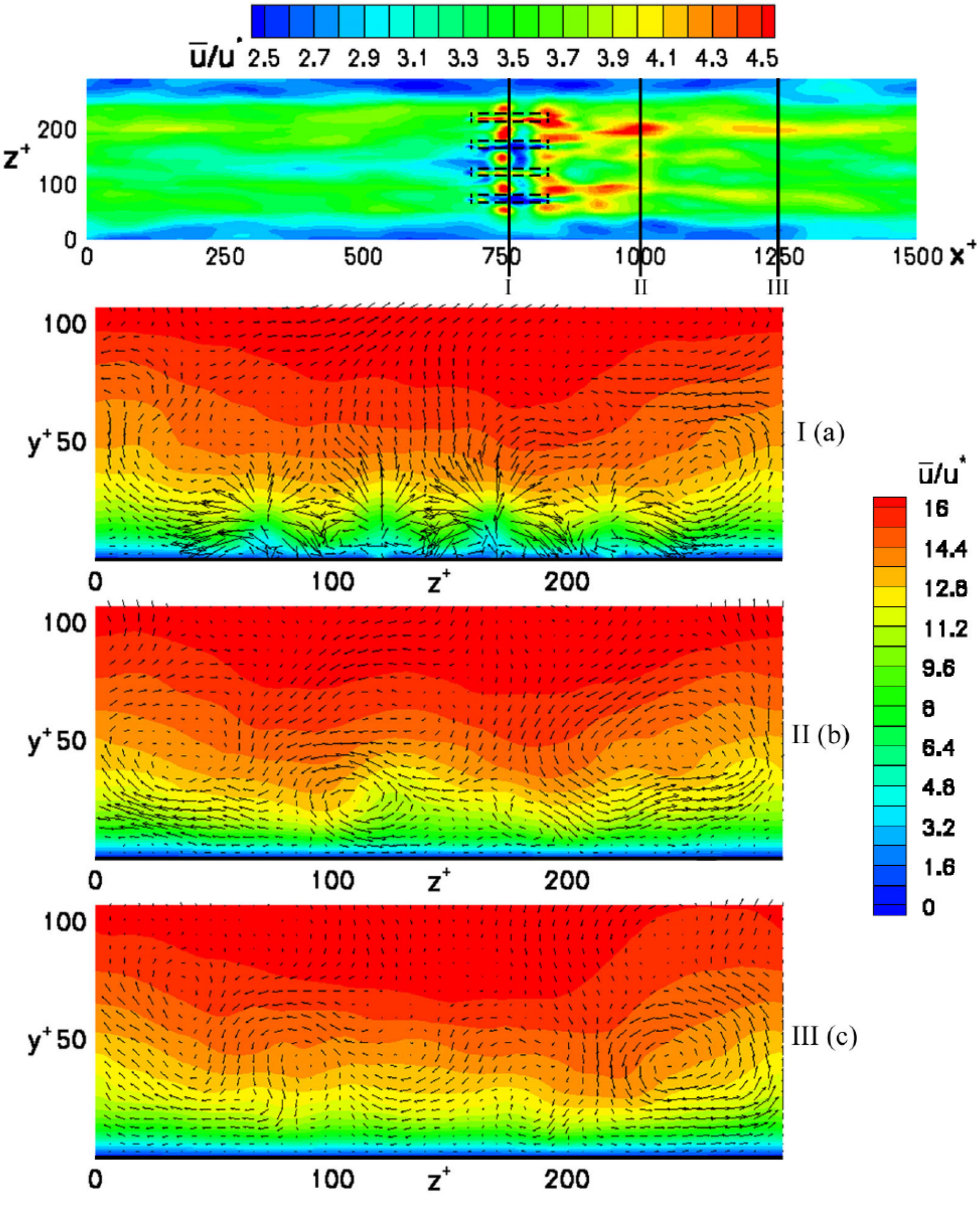

Figure 4.13: Time-averaged contours of u velocity on $xz-$plane $4l^*$ above the virtual surface for "-+-+" mode and on $zy-$planes at: (a) $x = 750l^*$, (b) $x = 1,000l^*$ and (c) $x = 1,250l^*$ (note different color bars).

4.5 Single Pulse Actuation

The periodic actuation of the previous section showed that moderate strength jets could affect the streak pattern near the surface. In contrast to the quasi-steady actuation of Section 4.4, vorticity produced by the periodic pulsing slots was a result of ejexted fluid rolling up into hairpins from shearing of the mean flow. While the jets themselves were quick to dissipate, the complex interaction between a blowing pulse and the boundary layer produced effects that far outlasted the pulses themselves. However, it would be unrealistic to expect a positive result in drag reduction simply with the quasi-steady and periodic actuations used above. As shown in the previous section, continuous periodic pulsing of the devices increased flow mixing and net drag. For effective drag reduction, the actuators must act in a way to eliminate or suppress flow structures responsible for high shear stress but not otherwise cause large mixing in the channel. Clearly, arbitrary blowing/suction pulses were unable to achieve this but selective actuation may provide a better measure of flow control. Such a method would rely on detecting particular structures and selectively activating one or more actuators to eliminate or disrupt the target. As noted by Gad-El-Hak [11], streamwise vortices were considered to be ideal targets for actuation due to their role in streak formation and in the breakdown of the shear layer. However, as pointed out at the beginning of this chapter, enstrophy "pancake" structures were also potential target structures due to their correlation with regions of high shear stress. Since the previous section showed that the blowing jet structure consisted of hairpin vortices, it may be possible to make such hairpin interact with a particular flow structure in a positive fashion.

The effect of single actuator pulses on turbulent boundary layer structures were studied by selecting appropriate instances in which a particular "pancake" boundary layer structure would pass over one of the slot jets. The simulation was then rewound and the devices set to blow a single pulse to disrupt the evolution of the structure. Two types of single actuation were tested: a steered jet and a strong jet. The steered jet, as seen in figure 4.14(a), was created by shaping the slots to produce a central blowing jet tilted approximately 45 degrees from the normal direction toward the corresponding suctioning slot. This tilted jet design was used so that fluid from a blowing slot was more likely to be suctioned through the corresponding slot, inducing a spanwise movement in the flow. As seen in the instantaneous contours of streamwise vorticity through the center of the tilted slot (fig. 4.14(b)), a single blowing pulse in the absence of channel flow is indeed drawn towards its suctioning neighbor and the resulting jet should not have as much upward momentum as a straight jet. Hairpins from the blowing jet structure would remain closer to the surface and allow for the study of the interaction of the hairpins with a particular target. The steered jet pulse length, during which the slot went through a blowing pulse only, was $T/2 = 15t^*$ while the peak average blowing velocity was $3u^*$. In contrast, the strong jets used the preexisting geometry in a combination of single or paired blowing in attempts to eliminate or lift structures away from the surface. The strong jet pulses were shorter and intense, lasting $T/4 = 7.5t^*$ and with twice the strength, $6u^*$. In both cases, a blowing pulse or pulses were created and their subsequent interaction with the boundary layer structures was followed over several thousand time steps. Flow events and their evolution were compared to an un-actuated case starting from the same initial condition and spanning the same time interval.

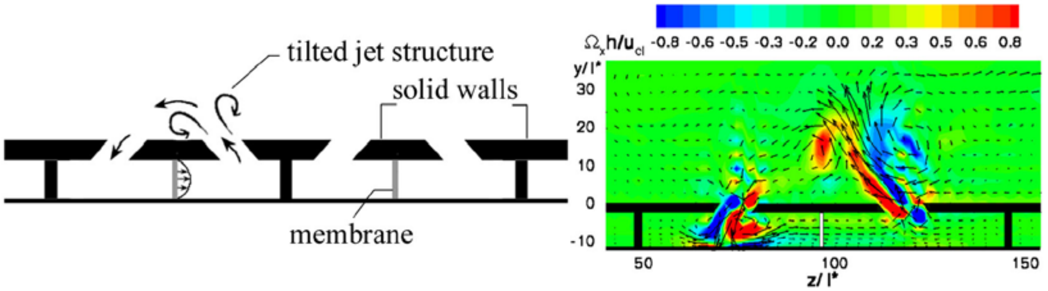

(a) (b)

Figure 4.14: (a) Schematic slice of tilted actuation domain with tilted jet flow structure and flow direction arrows and (b) sample instantaneous contours of streamwise vorticity and velocity vectors on zy-plane through the tilted slots.

In the case of the steered jet, the target structure was a sliver-shaped "pancake" associated with a pair of streamwise vorticity "worms." As seen in figure 4.15(a), the target structure lies upstream of the second slot from the left. A tilted jet pulse was used in an attempt to either disrupt or displace the target structure in the spanwise direction. In this case, the single pulse was issued ahead of the target structure. As seen in figure 4.15(b), the jet structure rises to meet the incoming target structure as it rolls up into hairpin vortices. The jet hairpin vortices were observed to engulf and disrupt the

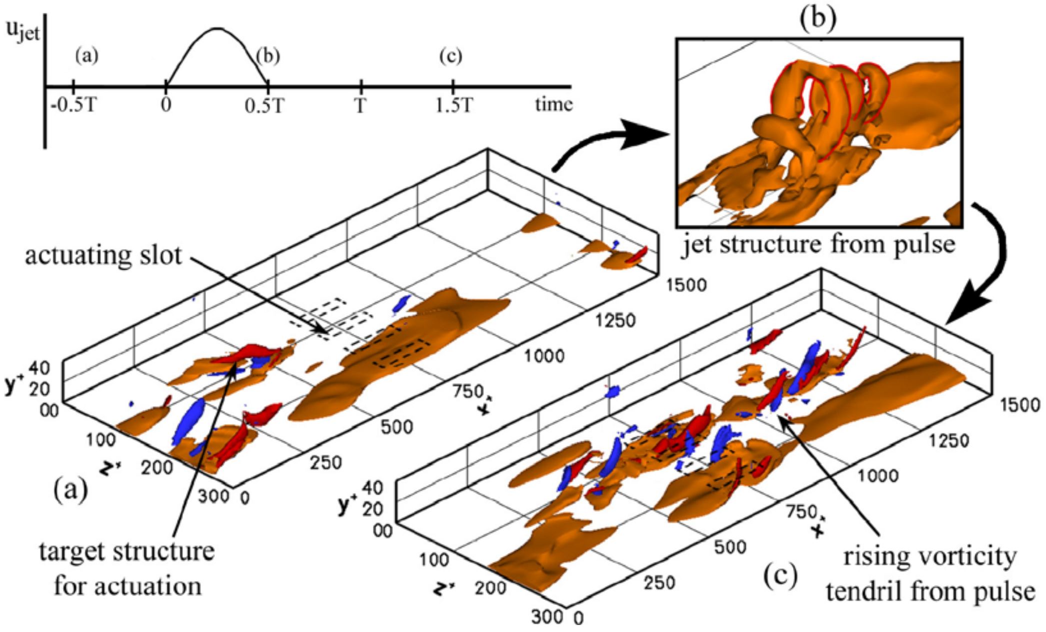

Figure 4.15: Schematic of jet actuation and contours of enstrophy of tilted jet single pulse: (a) $0.5T$ prior to actuation, (b) close up at the end of the pulse and (c) $1.5T$ after the pulse.

evolution of the original pancake boundary layer structure. However, as seen on figure 4.15(c), resulting structures do not appear to have shifted in the spanwise direction. Moreover, the blowing pulse leaves behind several rising tendrils of vorticity and also creates new pancake structures of similar size as the original target. Comparison between the drag for the undisturbed flow and the tilt-jet-activated flow over a short period of time equivalent to 4 pulses ($60t^*$) indicated a 2% increase due to the pulse. No error bars were calculated since there was only a single realization.

In the case of a strong jet, the target structure was a large pancake

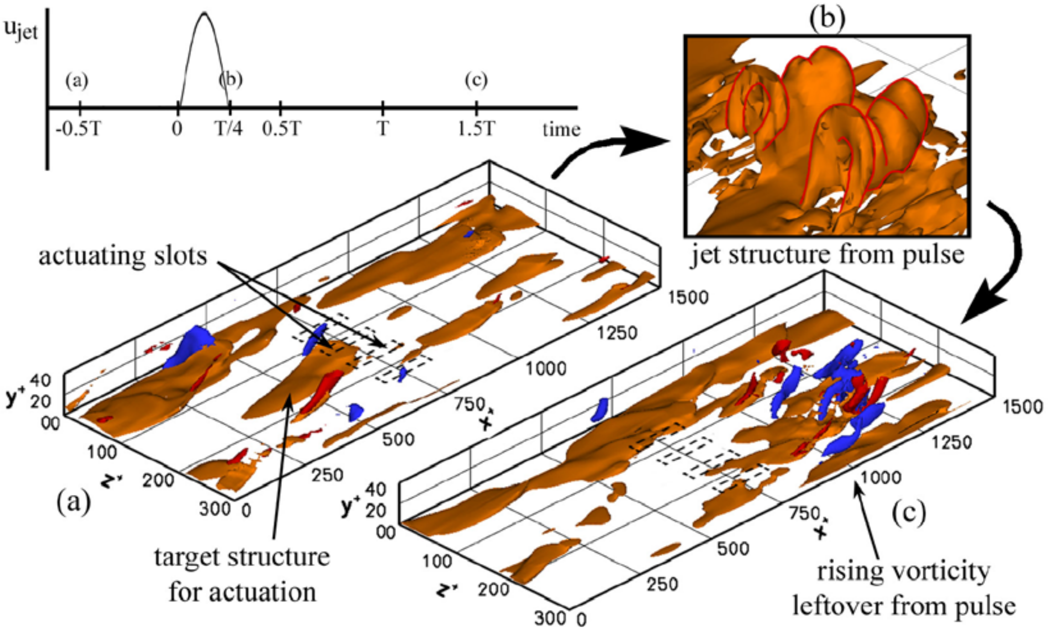

Figure 4.16: Schematic of jet actuation and contours of enstrophy of strong pulses: (a) $0.5T$ prior to actuation, (b) close up at the end of the pulse and (c) $1.5T$ after the pulse.

structure approaching the two center slots. As seen in figure 4.16(a), the target structure could be actuated on by a single blowing pulse from either one or both slots. In the case shown in figure 4.16(b), both center slots issue single blowing pulses directly underneath the pancake structure. The resulting large pair of hairpins completely obliterated the pancake structure. However, as seen on figure 4.16(c), the strong pulse also creates more pancake structures and again, as the jets quickly rise, several rising tendrils of vorticity are left in the wake. For this case, the calculated drag over 4 periods ($30t^*$) after the pulse indicated a 1.4% rise when compared to the undisturbed flow over the same period of time. A separate run was also attempted with only one of the center slots active. Although not shown, time evolution showed that the solitary pulse simply pierced through the pancake structure without canceling much of the large structure. In addition, the solitary pulse also resulted in several downstream vorticity tendrils similar to the combined pulse.

4.6 Hybrid Surfaces

While only a few of the above single pulses were tested, they did show that slot jets can be made to interact with specific turbulent boundary layer structures. However, as reported in the previous section, achieving useful control of boundary layer structures was hampered by the tendency of the jets to introduce new vorticity or at least cause greater vertical mixing of the flow. Despite detailed knowledge of the approaching flow structures and convenient placement of the devices, targeted pulses did not provide useful flow control. Changing the jet strength to calibrate the pulse might result in some measure of flow control, as seen later in Section 4.7. Uncalibrated, weak actuation, as in the quasi-steady actuation of Section 4.3, was able to induce changes in the boundary layer over time. However, the resulting jet structures were too small to interact with targeted boundary layers structures in the manner desired. As an alternative, hybrid surfaces combining passive elements and active devices might provide some flow control while still being able to take advantage of the hairpin structure of stronger jets. The chosen passive elements were triangular riblets with cusped tips aligned in the streamwise direction. The riblets had a ratio of height to base width of 1.07 with a height of $14.6l^*$, taller than any configuration used in Goldstein and Tuan [32] but on par with experiments cited in Walsh [28].

The computational domain was modified to contain a single actuator unit with two coupled slots as seen in figure 2.6. The slots were larger than used in the previous sections and placed $145l^*$ apart to reduce the effect each slot would have on its neighbor. Streamwise riblets spanning the length of the channel were placed adjacent to each slot. The separation distance between the rib crests was $100l^*$, twice the approximate separation distance between a pair of counter-rotating streamwise vortices. No drag reduction was expected from the riblets since, according to the experiments of Walsh [28], separation distances above $30l^*$ caused drag increases. However, this configuration would be useful to isolate and allow the study of a single slot jet/riblet unit. For the purposes of this study, the streamwise riblets might be able to re-orient and re-organize turbulent structures prior to actuation. Actuation itself could perhaps then be done with a weak to moderate jet strength to attempt to reduce the spanwise movement of fluid in the region immediately above the slots.

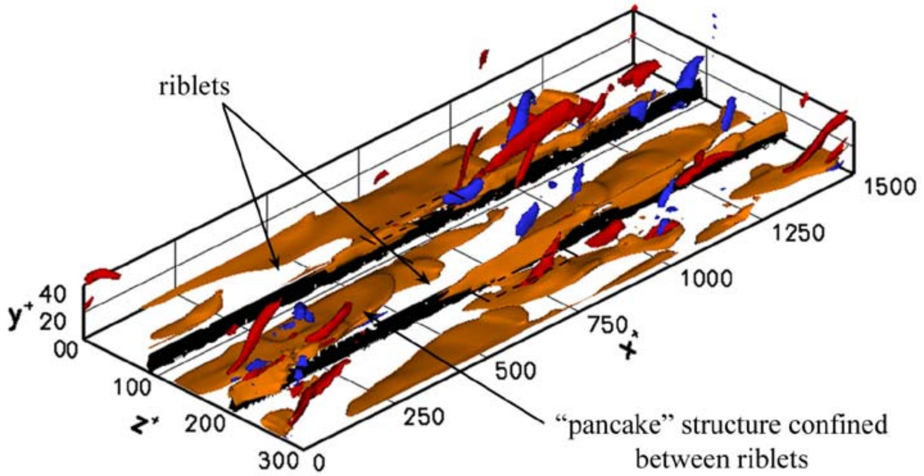

Figure 4.17: Iso-surfaces of enstrophy and red/blue streamwise vorticity worms for channel with 2 riblets.

Initial runs had the actuators inactive in order to examine the effects of only the riblets on the flow. As seen in figure 4.17, a pair of riblets is able to contain the "pancake" boundary layer structures between them. This "combing" of the flow may be beneficial in concentrating high-shear structures onto specific regions of the surface where actuators can be mounted. In addition to "combing" the flow, enstrophy structures are also seen sliding along the crest of the riblets. Such crest structures are generated by riblets protruding into a higher momentum flow at the edge of the viscous sublayer. This presents a potential drag increase not only due to the increase in surface area of the riblets but by also placing them in contact with a higher shear stress flow. Consequently, for a potential drag reduction, both the "pancake" structures between riblets and the crest structures would have to be actuated on.

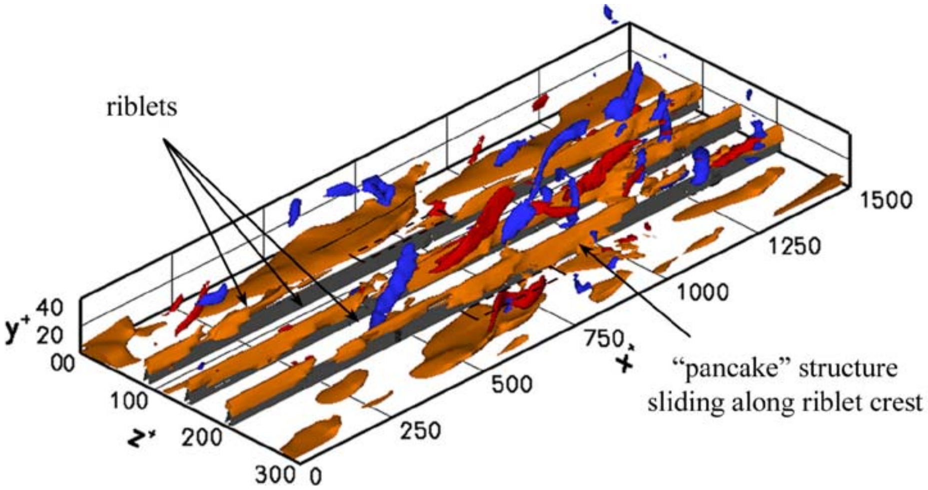

Figure 4.18: Iso-surfaces of enstrophy and red/blue streamwise vorticity worms for channel with 3 riblets.

Further runs were made with an additional riblet placed between the original pair. The riblet spacing was then equivalent to the accepted streamwise vortex pair separation of $50l^*$. The net effect as seen in figure 4.18 is to essentially eliminate the "pancake" boundary layer structures from the surface between the ribs so that only the crest structures remained. The drag for this configuration of three riblets and no actuation through the slots was averaged over $2,500t^*$. As expected, there was a drag increase for the configuration, measuring $6.7 \pm 3.2\%$ higher than the opposing flat surface over 16 independent realizations. Experiments on triangular riblets of height $15l^*$ placed $45l^*$ apart cited in Walsh [28] yielded a drag increase of approximately 2.5%. The larger drag increase seen here was likely related to the increase in wetted area and the protrusion of the riblets into a higher shear flow.

Since the most apparent flow structures were riding on the riblet crests, single blowing pulses were issued from a slot adjacent to a riblet in an attempt to eliminate or dislodge them. The pulse was of the same length as in Section 4.5, lasting $T = 15t^*$ and operating in blowing mode only. Peak average jet strengths of $3u^*$, $4.5u^*$ and $6u^*$ were tested. With a jet strength of $6u^*$, the familiar pattern described in Section 4.4 occurred, with the jet rolling into a family of hairpin vortices. It was expected that a blowing pulse beside a riblet would be turned by the Coanda effect, conducting the jet fluid along the riblet face to the crest where the target structure was located. A sequence of images depicting the time evolution of a $4.5u^*$ jet is shown in figure 4.19. The Coanda effect is seen as the main hairpin vortex shifts in the spanwise direction toward the riblet so that the legs of the hairpin straddle the riblet before dissipating. However, the pulse does not obviously dislodge or eliminate the enstrophy structures sliding along the riblet crests. Moreover, at this jet strength, the resulting jet hairpin rises above the riblet crest and as it dissipates, leaves behind considerable vorticity in a manner similar to the single pulses of Sec. 4.5. Not surprisingly, comparison between the drag with and without the single $6u^*$ pulse over a short period of time equivalent to 4 pulses ($60t^*$) showed a 4% increase with respect to the baseline drag of the configuration. Reducing the jet strength to $4.5u^*$ showed an identical jet evolution as for the $6u^*$ jet with a drag increase of 6% instead. Further reducing the jet strength to $3u^*$ produced a much smaller hairpin which rose to a height of $30l^*$, around twice the height of the riblet. The hairpin itself dissipated quickly within a slot length leaving behind little identifiable leftover vorticity. The weak jet was also not strongly turned by the Coanda effect so there was minimal shift in its position in the spanwise direction. Overall, the $3u^*$ blowing pulse had minimal interaction with the target crest structure and consequently had little effect on the drag. The calculated drag showed only a marginal increase of 0.8% when compared to the baseline flow.

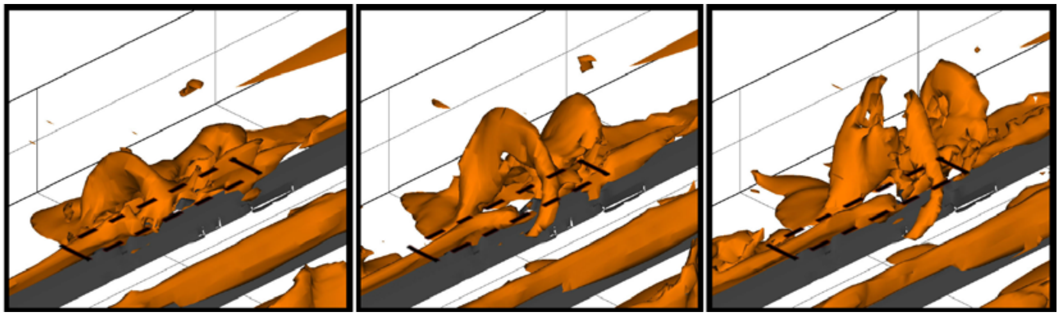

Figure 4.19: Time-evolution of blowing pulse of peak average strength $4.5u^*$ beside a streamwise riblet. Note the shift of the hairpin toward the riblet.

4.7 v-Opposition Control (*VOC*)

The control method attempted up to this point relied on the hairpin vortex structure produced by a blowing pulse to interact with pre-existing flow structures. This simplistic approach allowed the use of jets of arbitrary strength but also imposed a lower limit below which the jets would be too weak to generate the hairpins. However, periodic and selective actuation with this method, despite being able to appreciably affect the boundary layer, did not result in useful control. Attempts at using hybrid surfaces to aid the actuators had mixed results. Passive structures were able to organize the boundary layer structures but seemed to cause drag increases on their own. Combining actuators with the passive structures showed that even in a hybrid configuration, pulses of arbitrary strength were still unable to positively manipulate flow structures.

The inability to reduce drag so far clearly indicated that a different control method had to be considered: a feed-back control loop to carefully calibrate the actuator strength. In this manner, flow control would be attempted by allowing the actuators to continuously introduce small changes to the flow. This would be in contrast to the previous method which relied on selective actuation of moderate strength producing flow structures on the same scale as the targets. Feed-back control methods have been very successful in reducing drag as shown in the studies of Choi *et al.* [25] and Koumoutsakos *et al.* [26]. The difficulty here lies in whether these control algorithms can be applied to discrete actuators or whether their results can be replicated with more realistic devices. To this end, a control algorithm will be examined and tested, first on its own with the current numerical method and then it will be applied to slot jets in an attempt to determine its suitability for realistic flow control.

The chosen feedback control algorithm for the final part of this study, known as velocity opposition control, was the same as in Choi *et al.* [25]. As described in Chapter 1, opposition control sought to stabilize the boundary layer by applying a velocity boundary condition at the wall of opposite magnitude to values sensed at a height $10l^*$ above it. The detected velocity values at each instant in time were applied on the wall in the opposite direction without adjustment to their magnitude. This method took advantage of the full flow field knowledge available in numerical simulations to make up a simple feedback control algorithm capable of substantial drag reduction. While the original Choi *et al.* [25] study tested normal (v) and spanwise (w) blowing at the wall, Koumoutsakos *et al.* [26] focused on the $v-$velocity only since it was more similar to the effect of realistic actuators. Parametric studies on the height of the detection plane showed drag reductions for detection planes at heights from $10l^* - 15l^*$ while detection at a height of $y = 25l^*$ led to a drag increase. Optimal drag reduction was found to occur for a sensing plane $15l^*$ above the surface. Those results were taken into consideration when the $v-$velocity opposition control method (from here on referred to as VOC) was applied to the current force field simulation method.

4.7.1 Modified *VOC*

Since the *VOC* scheme described above relied on uniform blowing/suction at the wall, it could be seen as an idealized case of a uniform, dense distribution of + and - micro jets. But practical actuators are discrete and of finite size. Moreover, as the studies of Sec. 4.3 proved, there can be tangential flow on the actuator orifice exit plane – a factor that is not represented on the original *VOC* formulation. Therefore, a gradual, systematic testing approach was chosen in which the first step consisted of applying *VOC* with the current force field simulation method.

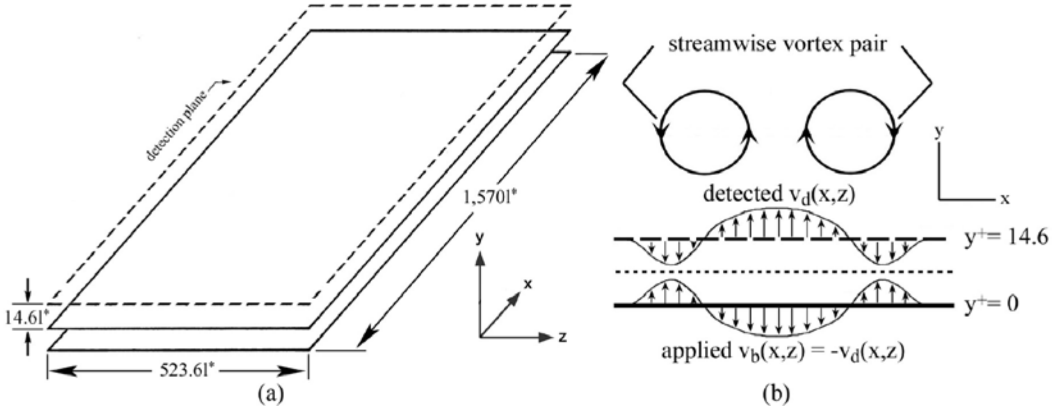

Figure 4.20: (a) Schematic of domain used with *VOC* method and (b) schematic of method being applied on a cutout of the surface.

In order to provide data for a comparison with discrete actuators, *VOC* was first applied to a simple geometry of a flat plate in a channel as seen in figure 4.20(a). This configuration is similar to the original Choi *et al.* [25] study. The flat plate consists of a single plane in the computational mesh located 12 gridcells above the lower boundary. The gap between the flat plate and the channel boundary is necessary to supply fluid through the plate for the *VOC* method. There are no mass flow issues since, for this strictly incompressible simulation, there is no net flow through the plate. Similar to the original Choi *et al.* [25] study, detection occurs at level 15 for a corresponding sensing height of $10.6l^*$ above the plate. As shown schematically in figure 4.20(b), the *VOC* method detects a value of v at a certain grid point on the sensing plane at time t. In this case, v is directed, for example, upward due to the upwash of a pair of counter-rotating streamwise vortices. At time $t + dt$, the inverse value of v is applied at a corresponding gridpoint on the surface as boundary suction to counter the fluctuation detected at the previous time step. For the full *VOC* method, this mechanism is applied at every grid point on the sensing plane and virtual surface resulting essentially in a 128×128 array of microjets.

Initially, the channel x and z dimensions were adjusted to match the width and length of the large domain used in Choi *et al.* [25]. The domain measured $1,575l^*$ in length with a width of $523.6l^*$. The corresponding $Re_{channel}$ and R^* were then $2,100$ and 116, respectively. Note that these vales are considerably lower than the original Choi *et al.* [25] runs, which had a $Re_{channel}$ and R^* of $3,300$ and 158, respectively. The impact of the *VOC* on boundary layer structures was immediately seen as demonstrated in figure 4.21. Figure 4.21 shows instantaneous contours of enstrophy and red/blue streamwise vorticity "worms" before and at a later time. As seen in the figure, at about $200t^*$ after control has been activated, a maximum instantaneous reduction in the number of boundary layer structures near the wall occurs. Subsequent runs showed a slight increase in the number of strcutures until a somewhat steady-state was reached. Continuous runs to $1,630t^*$ indicate an overall drag reduction on the one active channel wall of $18\% \pm 1.8\%$ with a 90% confidence interval assuming a normal distribution over 13 independent realizations. The drag reduction remained nearly unchanged when the actuated plate was placed at level 8 with detection at level 12 for a corresponding detection height of $10.5l^*$. This drag reduction was less than the 25% reduction on each wall obtained in the simulations by Choi *et al.* [25]. The different drag reduction values may be related to the form of drag calculation used here and outlined in Chapter 2. It should be noted once more that the calculated drag values here are on the actuated surface with respect to the opposing, un-actuated boundary – not the global drag reduction values of Choi *et al.*. In addition, the lower R^* of the present simulation and the geometry used for the modified VOC runs may also be affecting the calculated drag values. In this case, turbulence generated at the un-actuated boundary can be expected to constantly impinge on the actuated surface.

Similar results were obtained when the domain was reduced to the narrower domain width of $291.2l^*$ and length of $1,500l^*$ used in other slot jet and riblet simulations in this study. This narrower domain size resulted in a $Re_{channel}$ of $2,000$ and a R^* of 110. For the narrower domain, a parametric study was conducted by placing the actuated plate at levels 6, 8 and 12 with detection heights kept at around $10l^*$ above the plate. All simulations were

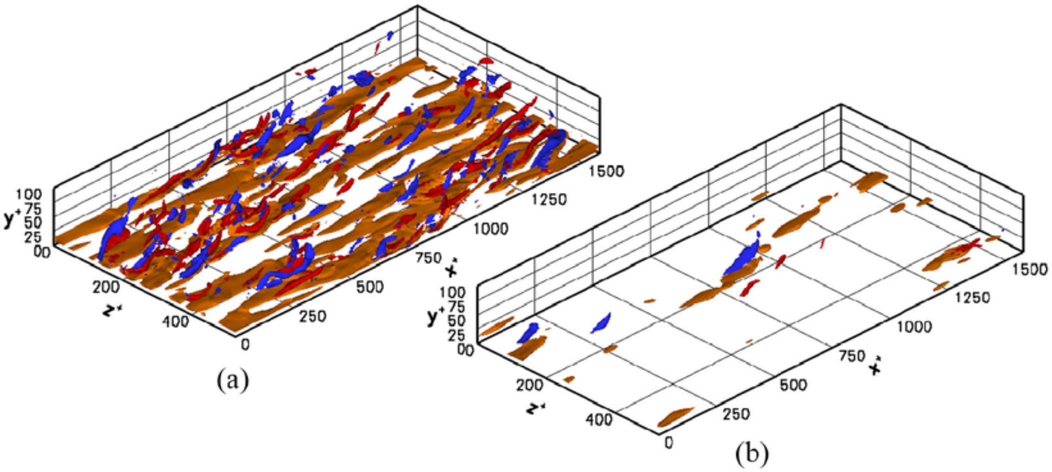

(a) (b)

Figure 4.21: Iso-surfaces of enstrophy and red/blue streamwise vorticity worms in large domain for (a) no *VOC* and (b) *VOC* after $200t^*$.

allowed to run for at least $5,100t^*$ after control was turned on and the data collapsed onto single 1-D profiles. For comparison purposes, profiles for an un-actuated case were also plotted. Mean velocity and Reynolds stress fluctuations are shown in figures 4.22 and 4.23, respectively. The results mirrored the findings of Choi *et al.* [25]. For the *VOC* plate at all three levels, figure 4.22 shows that the streamwise $\overline{u}_{rms}$ fluctuation shifts outward, away from the wall while the $\overline{v}_{rms}$ reaches a minimum value at around $y = 5^*$. This indicated the formation of a quasi-stagnation plane where fluid issued from the wall balanced fluctuations from the mean flow. A plot of $-\overline{u'v'}$ also shows an outward shift for the *VOC* at levels 8 and 12 but not at level 6. Instead, the $-\overline{u'v'}$ values seem to fluctuate near the actuated surface until eventually settling at levels comparable to the un-actuated case.

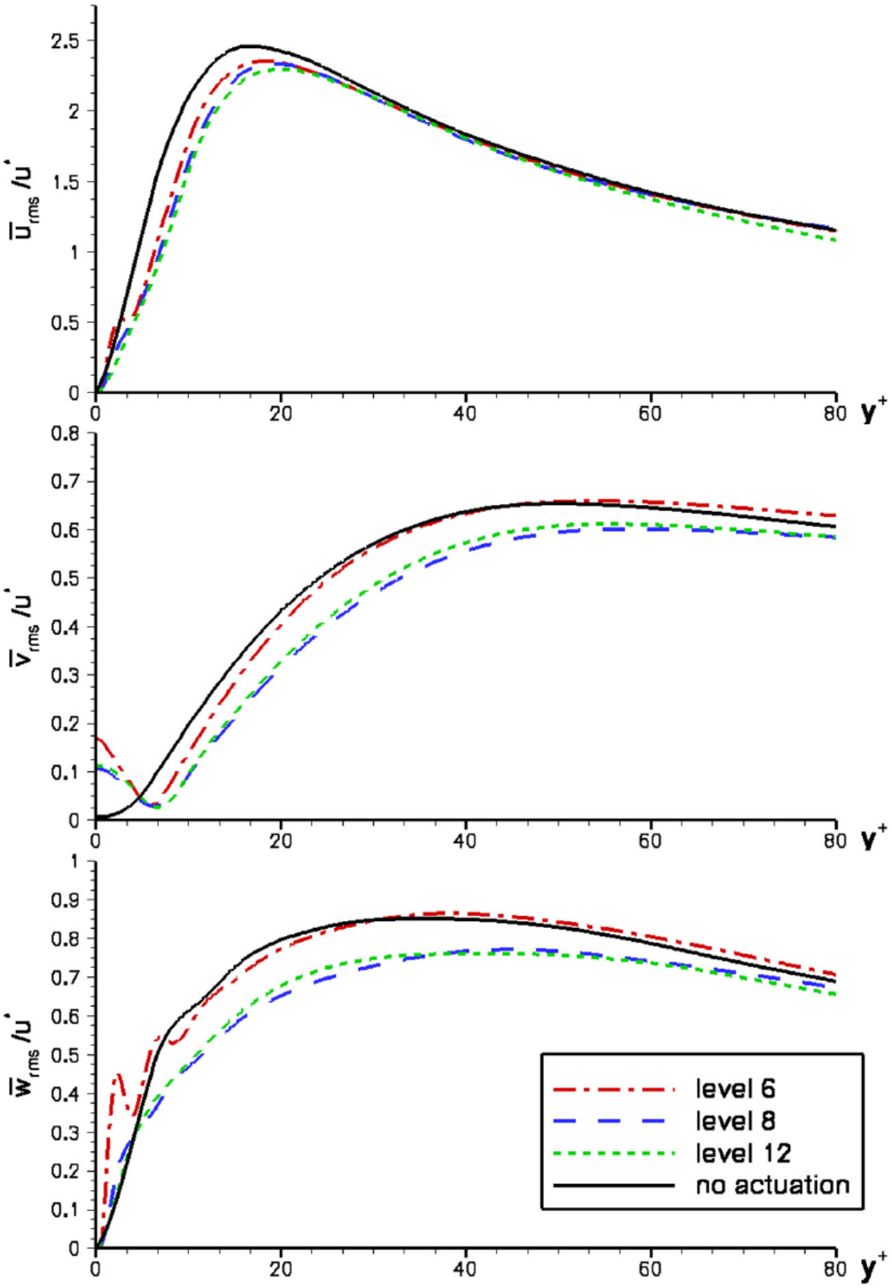

Figure 4.22: Averaged RMS fluctuations of velocity components across the channel for un-actuated plate at level 12 and *VOC* forcing plates at levels 6, 8 and 12.

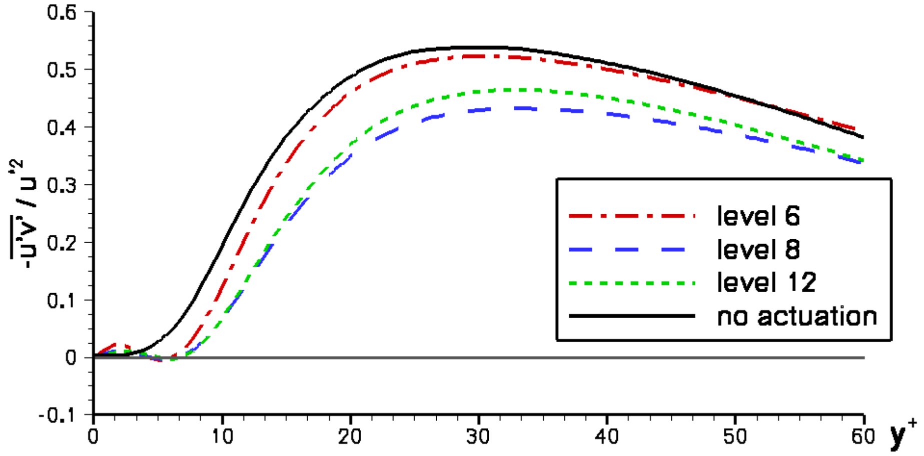

Figure 4.23: Reynolds stresses across the channel for un-actuated plate at level 12 and *VOC* forcing plates at levels 6, 8 and 12.

The averaged profile of the Reynolds shear stress is shown in figure 4.23 and the results also conform to the Choi *et al.* [25] study. There is an observable decrease in $-\overline{u'v'}$ for all *VOC* cases when compared to the un-actuated profile. There is also a region for $y^+ < 6$ in which very low Reynolds stresses are seen. These results conform to the findings of Choi *et al.* [25] in that the *VOC* control scheme reduces the strength of turbulence-generating events and effectively shifts the profiles away from the surface. In this manner, *VOC* appears to physically behave like an exceptionally effective riblet surface, as mentioned in Chapter 1. Near wall behavior of $-\overline{u'v'}$ is identical for the plate at levels 8 and 12. The slight variation between the two surfaces at $15 < y^+ < 60$ may be attributed to noise or the narrowing of the height of the channel as the plate is moved upward. However, similar to the velocity profiles of figure 4.22, the plate at level 6 diverges in behavior when compared to the other *VOC* surfaces. Instead, a local maximum is present in the region $y^+ < 6$ which shows values of $-\overline{u'v'}$ larger than for the the plate at levels 8 and 12. Away from the wall, $-\overline{u'v'}$ reductions were also not as large as observed with the other active surfaces and the overall trend is more similar to the un-actuated plate.

Clearly, when the *VOC* surface was placed at level 6, it performed differently from the other locations. It is likely that with the plate at level 6, the gap between the plate and the bottom of the channel was too narrow for fluid to move freely enough to supply each microjet with adequate mass flow. The result was higher shearing stresses below the plate and a resulting contamination of the flow above the plate by Gibbs oscillations – more clearly seen in the $\overline{w}_{rms}$ profile of figure 4.22. Once the plate was placed at level 8 or higher, the gap provided sufficient mass flow and the results were insensitive to the position of the plate.

The calculated drag for the plate at level 8 had an average reduction of 18% over $200,000$ iterations corresponding to 13 independent realizations. The error margin was of $\pm 2.6\%$ with a 90% confidence interval. This drag reduction was identical to the one obtained in the wider domain and the larger error bar is a reflection of the narrower domain used here.

4.7.2 ***VOC* Strips**

While the *VOC* control scheme had been shown to reduce drag over a surface, its application to discrete actuators required the consideration of other issues. One issue was related to the effectiveness of the *VOC* control scheme when applied to discrete patches since actual devices cannot match the spatially smooth, continuous blowing/suction distribution of the numerical method. Thus, several test cases were run in which the actively-controlled area of the plate varied in length in the x-direction while still spanning the width of the plate. In this case, the size of the detection zone was also adjusted to match the control region of the surface. The domain used in this series of studies is shown schematically in figure 4.24. *VOC* strips covering 10%, 30%, 60% and 80% of the total length of the domain were chosen and each case was run for at least $150,000$ time steps or $3,045t^*$. In order to analyze the results, the time averaged flow was span-averaged to a single $xy-$plane and then futher into single profiles. Results were then compared to an un-actuated wall and the the full *VOC*.

Contours of normalized $\overline{v}_{rms}$ are shown in figure 4.25 for all *VOC* strips tested and the full *VOC*. For comparison purposes, contours for the un-actuated surface are also shown on the right of each figure. Results indicate the presence of a quiet dark blue “bump” of reduced fluctuations immediately over the locations of the strips. This quiet region is a result of the formation of a local stagnation plane above regions where *VOC* is applied. This implies that, within the region covered by the *VOC* strips, a minimum value

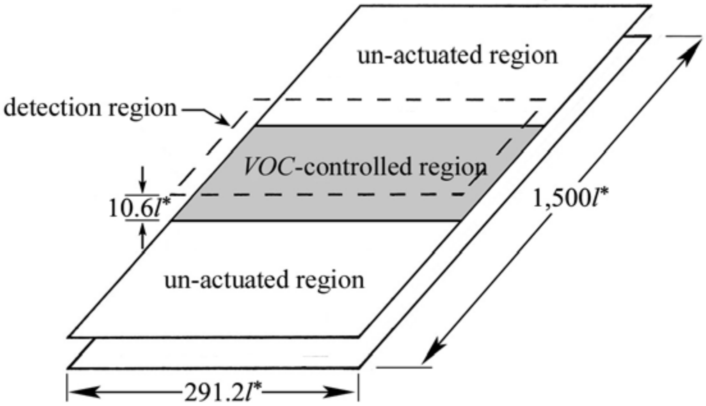

Figure 4.24: Schematic of domain used with *VOC* strips.

of $\overline{v}_{rms}$ is reached at a location away from the wall. The blue "bump" of reduced fluctuations does not extend far downstream or upstream of the strip location. However, a gradual increase in the thickness of the blue layer over the portions of the domain not covered by the strip is noticeable as the strip size increases when compared to the un-actuated wall. Away from the wall, fluctuation levels do not differ much between the un-actuated wall and both the 10% and the 30% strip. However, appreciable reductions in fluctuations in the outer region are noticeable for strips covering 60% or more. The dramatic reductions in fluctuations between a 30% strip and a 60% strip suggest there may be a critical coverage area limit for this particular type of control method and periodic domain to work.

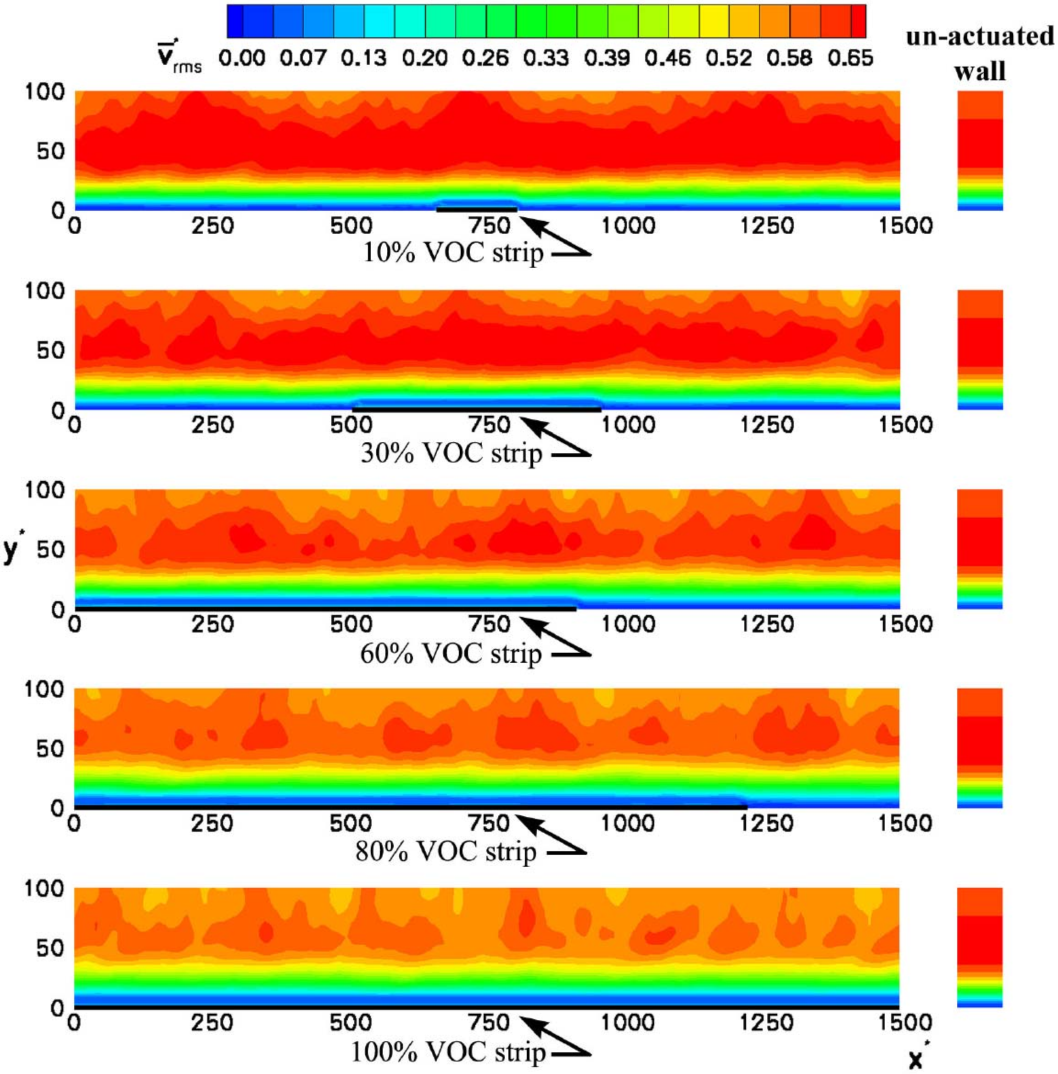

Figure 4.25: Span-averaged and time-averaged contours of v_{rms} on an $xy-$plane for several VOC strips.

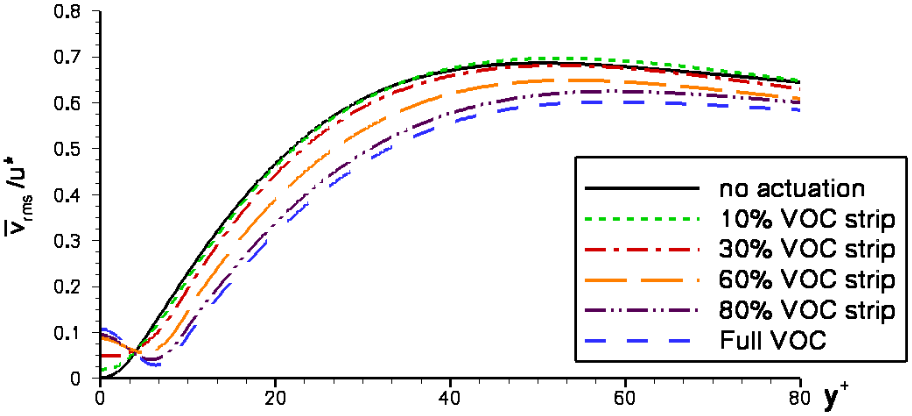

Figure 4.26: Averaged v_{rms} values across channel for several *VOC* strips.

The same results are reflected in the averaged normalized $\overline{v}_{rms}$ profile of figure 4.26. There is a gradual shift in the shape of the $\overline{v}_{rms}$ profile from the un-actuated wall to the full *VOC* as the size of the control region increases. From figure 4.26, it is clear that both the 10% and 30% strips do not form a mean stagnation plane and their profiles more closely resemble the un-actuated surface both near and away from the wall. Only for strips covering 60% of the domain did a minimum develop on the $\overline{v}_{rms}$ profile near the wall – suggesting the formation of a partial stagnation plane.

Normalized Reynold stresses contours are shown in figure 4.27 for all strips, the full *VOC* and the un-actuated wall. Similar to the $\overline{v}_{rms}$ contours, there is a noticeable thickening of the quiet blue layer of fluctuations directly above the control locations. Also similar to the $\overline{v}_{rms}$ contours, this quiet area does not extend far upstream or downstream of the control location. However, within the control region, the *VOC* method was able to extend its influence into the buffer layer by shifting successive contours of Reynolds stress away from the wall. This is particular noticeable for the 30% strip contour with the green layer directly above the blue “bump” being pushed into the red region of higher fluctuations. Further increases in the thickness of the blue and green layer are noticeable for the 60% and larger strips compared to the un-actuated wall. Further reductions in the red layer of fluctuations away from the wall are more prominent for strips covering 60% of the domain or more. This result was also noted for the $\overline{v}_{rms}$ contours with the most gain in terms of reduced fluctuations occurring when the strips were increased from 30% to a 60%.

The normalized Reynolds stress profiles of figure 4.28 show a similar pattern as the $\overline{v}_{rms}$ profile. Starting from the un-actuated wall, the profiles gradually shift towards the full VOC behavior as the strip size increased. Close examination of the near-wall behavior ($y^+ < 5$) indicates that all strip sizes induced slight local increases in Reynolds stress compared to the un-actuated surface. This effect was not necessarily considered detrimental since, despite introducing fluctuations at the wall, the full VOC method was able to produce a drag reduction. In the case of the full VOC method, the formation of the stagnation plane and the break-up of the near-wall cycle resulted both in a reduction in the impingement of incoming turbulence and the stabilization of the near wall flow - which combined to offset any potential small increases in Reynolds stress near the wall caused by actuation. However, no such stabilization effects effects were observed in figures 4.26 and 4.28 for the 10% and 30% strips due to their small coverage area.

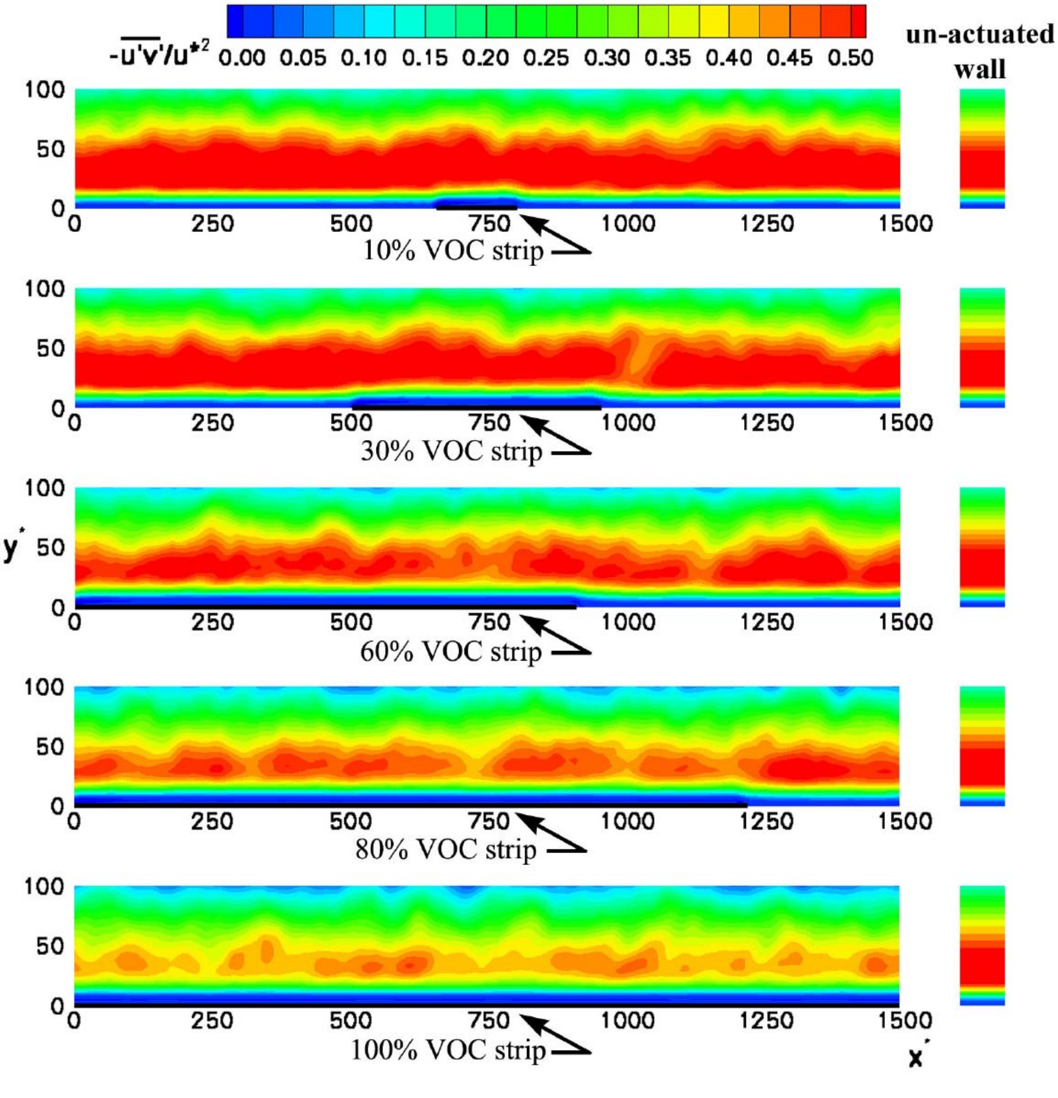

Figure 4.27: Span-averaged and time-averaged contours of Reynolds stress on an $xy-$plane for several VOC strips.

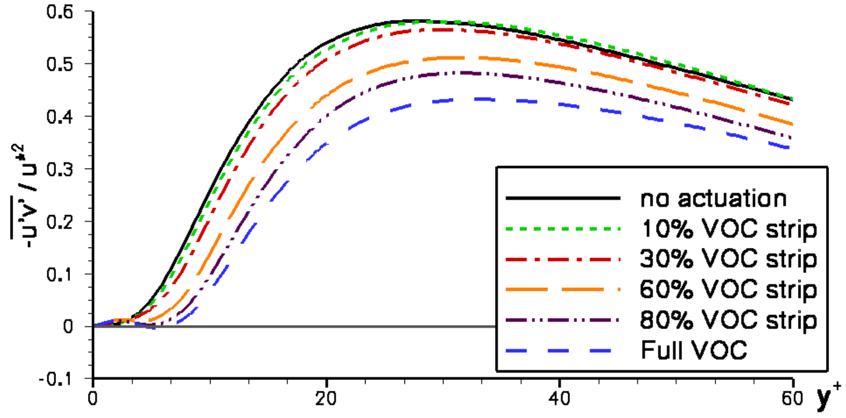

Figure 4.28: Reynolds stress values across channel for several *VOC* strips.

Figure 4.29 plots the instantaneous and average drag traces for all *VOC* strips tested with respect to the drag of the opposite, un-actuated boundary. The traces cover $200,000$ time steps from the moment control was turned on. The instantaneous drag traces (fig. 4.29(a)) contains a fairly high amount of noise. This reflects the relatively narrow width of the computational domain and the presence of the un-actuated top portion of the domain impinging new turbulence against the actuated surface. Despite the fluctuations in the instantaneous values, the running average drag ratios (fig. 4.29(b)) show that drag for all strips stabilized by $100,000$ time steps. Sample averages were computed for the $200,000$ time steps with a 90% confidence interval error bar and the results are shown in Table 5.1.

Table 5.1 shows that strips covering up to 30% of the total surface had similar small drag reductions of less than 4%. However, increasing the strip size to 60% of the total area or larger showed a substantial jump in the

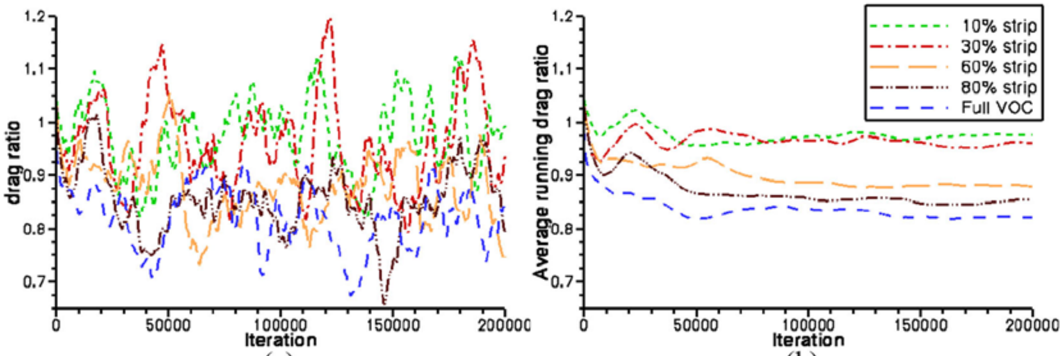

(a) (b)

Figure 4.29: (a) Instantaneous (b) and average running drag ratios for different size *VOC* strips and full *VOC* with respect to the opposing un-actuated boundary.

Table 4.1: Average drag reductions for different *VOC* strips.

Strip Size	Independent Realizations	Average Drag Reduction
10%	15	$3.1\% \pm 2.4\%$
30%	24	$3.2\% \pm 2.3\%$
60%	24	$12\% \pm 1.8\%$
80%	11	$13\% \pm 3.2\%$
full *VOC*	13	$18\% \pm 2.6\%$

drag reduction to over 10%. The large drag reductions with *VOC* covering 60% or more of the surface may be a result of partial re-laminarization of the flow. As seen in the instantaneous drag ratio of figure 4.29(a), the 60%, 80% and full *VOC* show periodic large dips in the drag ratio of 30% or larger, specially when compared to the average values. Partial re-laminarization may also explain the large drag decreases of 24% and 30% observed in the studies of Choi *et al.* [25] and Koumoutsakos *et al.* [26].

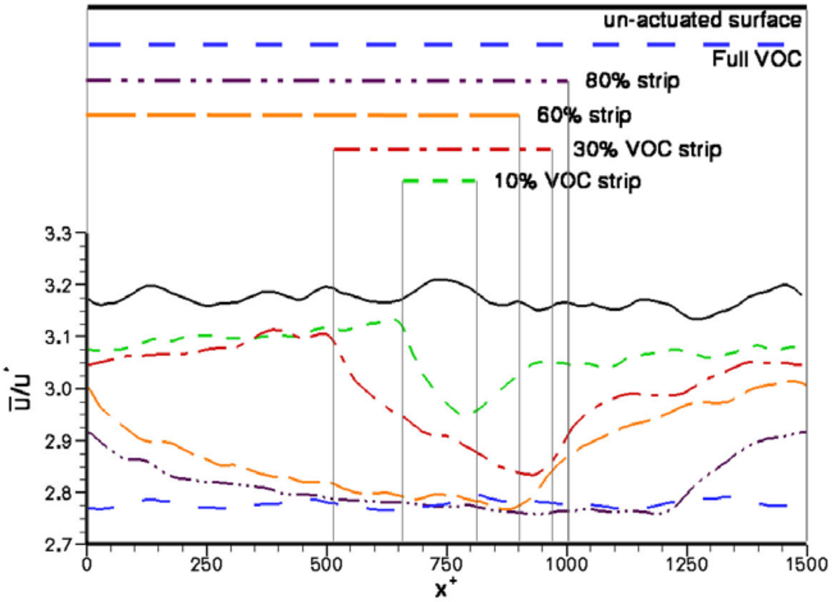

Figure 4.30: Time averaged and span averaged streamwise $\overline{u}$-velocity at $y = 3.6l^*$ above the plate for un-actuated boundary, *VOC* strips and full *VOC*. Legend at the top of the figure shows respective locations of active elements.

Figure 4.30 shows the time-averaged and span-averaged streamwise $\overline{u}$-velocity over the length of the domain for all *VOC* cases and the un-actuated wall. The $\overline{u}$ values were all sampled at a height of $3.6l^*$ above the plate for all cases. The figure legend shows each test case in color and patterns while the lengths of each legend line correspond to the locations at which *VOC* is being applied. As seen on the figure, $\overline{u}$, and by extension the local shear stress, decreases progressively over the location of the *VOC* strips. The $\overline{u}$ reduction extends downstream of the control locations before recovering. In the case of the 10% strip, this downstream zone of influence extends for a distance roughly equivalent to the strip length itself of $150l^*$. A similar recovery length can be observed for the 30% strip as well. As the size of the control region increases, the overall $\overline{u}$ values over the length of plate decreases reflecting the increasing drag reduction of each case.

The above results indicated that a substantial amount (as much as 60%) of the surface may have to be activelly controlled with the *VOC* method to produce substantial drag reductions. In this case, 60% represents a roughly critical size of actively-controlled surface necessary to form a partial stagnation plane capable of dampening $\overline{v}_{rms}$ and Reynolds stresses. This result is important in that, while a 100% coverage area may be desired to maximize drag reduction, it is not likely to be feasible with realistic actuators due to physical constraints. In this case, in order to induce sufficient changes to the flow to achieve some form of flow control, a scattered distribution of discrete actuators would then need to have a total amount of actively-controlled surface larger or at least equivalent to its own device-specific critical coverage area.

4.7.3 *VOC* Applied to a Single Actuator

The previous section indicated that *VOC* worked by dampening fluctuations near the surface and forming a vertical-flux stagnation plane roughly halfway between the surface and the detection height to dampen fluctuations. Results also indicated that a substantial amount of the surface had to be actively controlled to obtain a significant drag decrease. It was also noted that a critical coverage area is needed for substantial flow dampening to be achieved. However, the size of the critical area may or may not be dependent on the type of actuation used. For example, even if 60% of a surface is being controlled with discrete actuators, it might not result in the same effect as the *VOC* strip if the discrete actuator does not affect the flow in the same manner as the original *VOC*. Conversely, it is possible that a convenient combination of actuator type and placement may result in such an efficient control system that a critical area of would consist of less than 60% of the total surface. Although not dealing with discrete actuators, the numerical study by Koumoutsakos *et al.* [26] gave some encouragement that realistic devices may be able to perform at the same level as the *VOC* method. As reported by Koumoutsakos *et al.* [26], manipulation of the wall vorticity produced physical effects on incoming flow vorticity that were equivalent to the *VOC* method. Since the slot jets used in this study have been able to introduce considerable vorticity in the flow, it stands to reason that some form of flow control may be possible if this vorticity was directed to interact in a beneficial way with flow vorticity. As an initial step in answering those issues, the *VOC* method is applied here to a single discrete actuator to determine its performance characteristics.

The modified computational domain containing a single actuator and two slots was described in Section 2.3.3 and shown in figure 2.6. The same domain is used here, minus the streamwise riblet that was used in Section 4.6. Following the original *VOC* concept, a sensible control value for the feedback variable for a discrete actuator would be the average v-velocity over a region near or above the slot ($\overline{v}$). Using a $\overline{v}$ did have a caveat: because of the channel geometry and the incompressibility of the fluid, the net mass flow across each $xz-$plane has to be conserved. That is, the magnitude of $\overline{v}$ invariably decreases as the size of the detection region increases. In the limit of a detection area encompassing the entire $xz-$plane, $\overline{v}$ would be zero and there would be no actuation. While the size and location of the sensing region would be possible parameters for further studies, a control region of area equal to the slot and immediately over it at a height of $10.6l^*$ was chosen. While one slot was subjected to a *VOC* control loop, the other associated slot in the actuator design operated as a simple "breather" slot necessary for mass conservation. Two slot sizes were tested. The original geometry had a narrow slot slot measuring $18.2l^*$ wide and $226l^*$ long – a *length* comparable to that of a streamwise vortex. The second geometry had a wider slot measuring $40l^*$ in width and $103l^*$ in length – a *width* comparable to that of a streamwise vortex. If the devices worked to dampen fluctuations, a tear-drop like "quiet" zone should appear in the slot wake and perhaps to either side. Such information from both geometries would be useful in determining an optimum size and distribution of the slot jets.

Initial runs proved that the actuators were able to respond well to the fluctuations in the detected normal velocity. Figure 4.31 shows the area-averaged normal velocity both at the detection height ($\overline{v}_{detect}$) and at the slot exit plane ($\overline{v}_{slot}$) multiplied by (-1). Prior to actuation, $\overline{v}_{detect}$ shows variations in the order of $\pm 0.3u^*$ while $\overline{v}_{slot}$ values remained within $\pm 0.1u^*$. Once control is turned on, $\overline{v}_{slot}$ matched $\overline{v}_{detect}$ within a few hundred time steps to the point that the curves are almost identical. Overall, the magnitude of $\overline{v}_{detect}$ is about

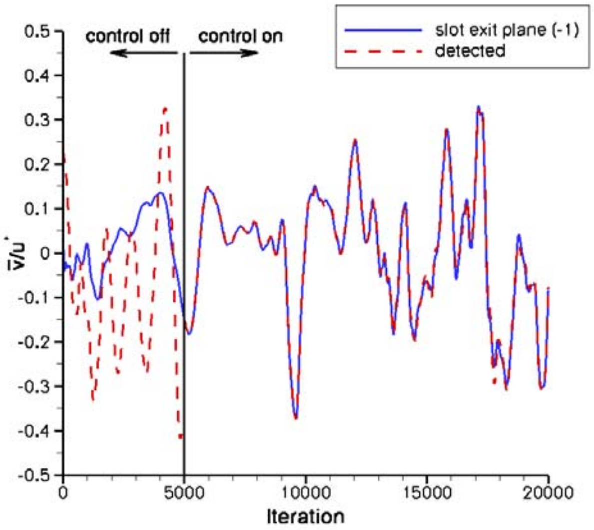

Figure 4.31: Comparison of area-averaged normal velocity at detection height and average velocity out of the slot (shown × -1) for single actuator case.

the same as the averaged $\overline{v}_{rms}$ of $0.34u^*$ at the detection height. As a result, the Reynolds number based on $\overline{v}_{rms}$ is $Re_{jet} = 3.1$ – on par with other flow control studies such as Rathnasingham [50].

Unlike the fairly strong jets seen in Sections 4.4 and 4.5, which produced a slug of fluid that rolled up into hairpins, the low Re_{jet} of the VOC slot jet produced a flow too weak to form a distinct jet. The result was of more of a local mild heaving of the boundary layer up or down. However, this prodding of the boundary layer still provided enough of a disturbance to affect the flow. Figure 4.32 shows contours of the streamwise velocity at a height $3.2l^*$ above the surface time-averaged over $1,630t^*$. The geometries plotted are: (a) the inactive original geometry of both passive slots; (b) the actuated

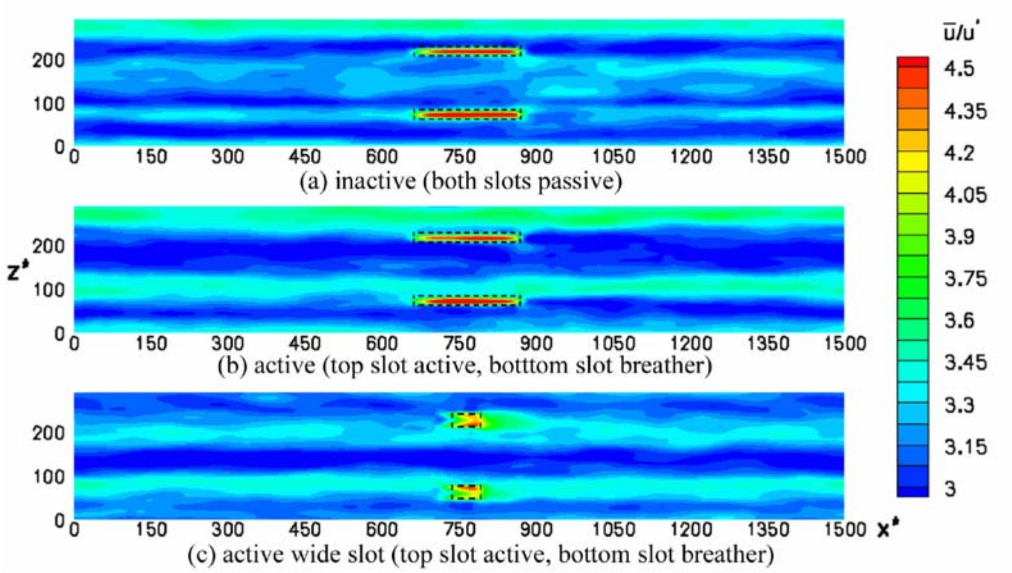

Figure 4.32: Time-averaged contours of streamwise velocity on an $xz-$plane $3.2l^*$ above the surface for: (a) inactive slots; (b) active narrow slot and (c) active wide slot.

narrow slot and (c) the actuated wide slot. Due to the narrowness of the domain, the time averaging was insufficient to eliminate evidence of some very persistent low speed streaks. However, the streak patterns give a quantitative measure of the effect of each configuration. Figure 4.32 (a) shows that the inactive case contains three low-speed streaks and three high speed streaks, each measuring approximately $40l^*$ wide. In contrast, the narrow control case (fig. 4.32(b)) indicates the formation of two asymmetrical pairs of low and high speed streaks, with the wider streak neighboring the control slot. Similar streak patterns are observable with the wide slot (fig. 4.32(c)).

For all test cases, the slots appeared as regions of high speed flow.

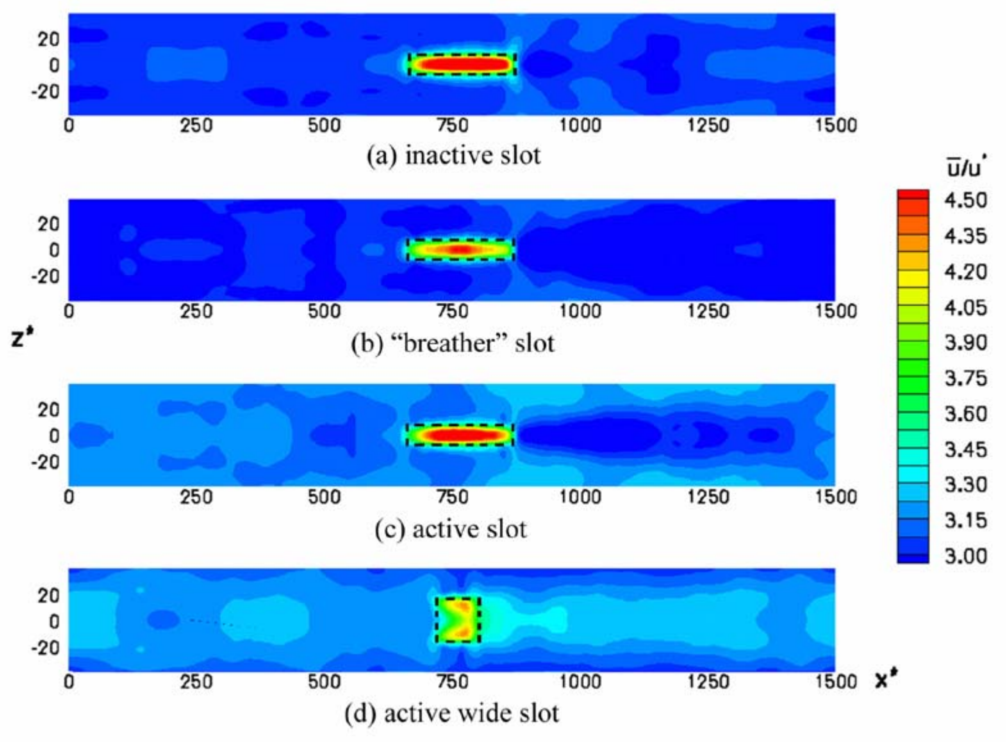

Figure 4.33: Time-averaged and span-averaged contours of streamwise velocity at $y = 3.2l^*$ above the surface for: (a) inactive slot; (b) "breather" slot; (c) active narrow slot and (d) active wide slot.

This was caused by the slots acting as low-shear regions, allowing the flow to accelerate over them like flow over a cavity. To better determine the effect of each slot, flow was time-averaged and span-averaged over the centerline of each slot. Figure 4.33 shows the resulting contours of streamwise velocity at $y^+ = 3.2$ for (a) the inactive slot, (b) passive breather slot, (c) active slot and (d) active wide slot. The inactive and passive breather slots show a nearly uniform level of streamwise velocity (fig. 4.33(a) and (b)). The active narrow slot (fig. 4.33(c)), however, shows a distinct low velocity (low shear) zone downstream of the actuator measuring approximately 2.5 slot lengths long and a slot width to either side of the centerline. Similar variations are found around the active wide slot (fig. 4.33(d)), except that a region of *increased* velocity develops downstream of the actuator location, indicating increased shear stress. Not surprisingly, no global drag reduction is observed for either case when compared to the inactive case: besides the obviously detrimental effects of a "breather" slot, the active slot is small, with an effective control area corresponding to less than 1% of the plate. However, the determination of a zone of effect for a single slot provides crucial information in the design of a control strip made up of multiple actuators, as described in the next section.

4.7.4 *VOC* Applied to a Row of Actuators

Despite having served its purpose well for several parametric studies so far, the actuator design used up to this point was not the most suitable for *VOC*. Due to the use of a pair of coupled slots, each actuator/sensor location was a relatively large device containing an active and a passive slot. Consequently, a more compact and flexible *VOC* design was created for a surface containing multiple, adjacent, controllable actuators. The basic geometry for the new configuration was described in Section 2.3.4 and shown in figure 2.7. The modified domains used in this section are shown in figure 4.34. As seen in the figure, the domains contain a single row of actuators spanning the spanwise $z-$direction mounted at the center of the plate. Similar to the actuators of figure 2.7, each slot is cut in a raised plate of thickness $5.8l^*$ and powered by its own membrane mounted flush at the bottom of the plate. However, unlike the devices of figure 2.7, the slots here have a straight throat instead of a tapered opening.

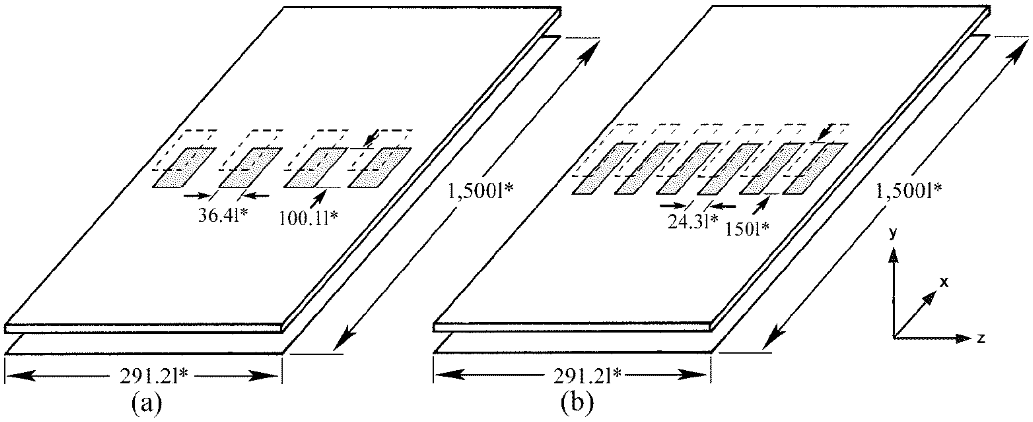

Figure 4.34: Schematic of single row of actuator domains: (a) *Case 1* (4 actuators) and (b) *Case 2* (6 actuators).

Results from the previous section were used to determine the spanwise spacing of the slots: an active slot was found to have a zone of influence of one slot width to either side of the centerline. Thus, for a downstream control zone spanning the width of the domain, the slots should be mounted with a spanwise spacing of, at most, one slot width ($1h$). For simplicity, this upper limit of $1h$ was used in designing a single row of actuators across the domain at the center of the channel. Two sets of actuators were tested:

- *Case 1* consisted of 4 actuators mounted equidistant from each other. Each slot had a width $h_1 = 36.4l^*$ and an aspect ratio of 2.75 for a length of $100l^*$. The slot width was such that $8 \times h_1$ corresponded to the width of the channel ($291.2l^*$).

- *Case 2* consisted of 6 actuators, each with a width $h_2 = 24.3l^*$ and an aspect ratio of 6.17 for a length of $150l^*$. Here, $12 \times h_2$ corresponded to the width of the channel.

The total amount of actively-controlled surface covered by each row of actuators was then 3.3% and 5.0% for *Case 1* and *Case 2*, respectively. It should be noted that such small coverage areas are almost guaranteed to fall below the critical coverage area. However, such study is still necessary to examine the interaction of the devices in close proximity to each other. As before, $\overline{v}$ was detected at a height $y = 10.6l^*$ and applied as a driving value at the membrane one time step later.

Figure 4.35 shows contours of time-averaged streamwise velocity on a $xz-$plane at $y = 3.2^*$ for the two actuator rows and a 10% *VOC* for comparison purposes. Each case was averaged over $2,030t^*$ and, as in the single actuator case, persistent streaks remain. Figure 4.35(a) shows that, for a 10% *VOC* strip two low and two high-speed streaks remain in the channel. The streak pattern is broken down within the control region and quickly recovers immediately downstream of the control region. Results for *Case 1* (fig. 4.35(b)) show a streak pattern composed mainly of two low speed streaks having a width of about the same size as the slot width h_1. Similar to the *VOC* strip, the streaks are disrupted over or alongside a slot but the effects do not extend

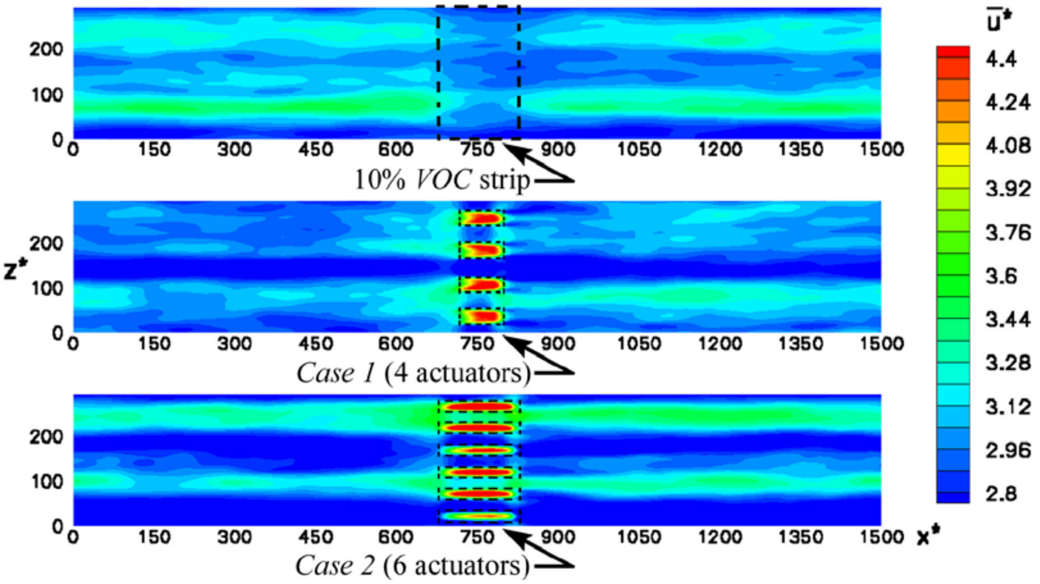

Figure 4.35: Time-averaged contours of streamwise velocity on an $xz-$plane $3.2l^*$ above the surface for: (a) 10% *VOC* strip; (b) *Case 1* (4 actuators) and (c) *Case 2* (6 actuators).

downstream of the location of the slots. Similar results are seen for *Case 2* (fig. 4.35(c)) with the low-speed streaks wider than for *Case 1*. Similar to the single actuator case, the slot locations for both cases are denoted by a higher streamwise velocity. The slots still seem to behave as a cavity despite the shallow depth at which the driving membranes were mounted.

Data for both cases were also time-averaged and span-averaged over the centerline of each slot and contours of the average streamwise velocity are shown in figure 4.36 compared against the 10% *VOC* strip. Figure 4.36 shows that flow starts to accelerate ahead of the control region of all three cases. In the case of the wide slot of *Case 1*, the acceleration zone extends

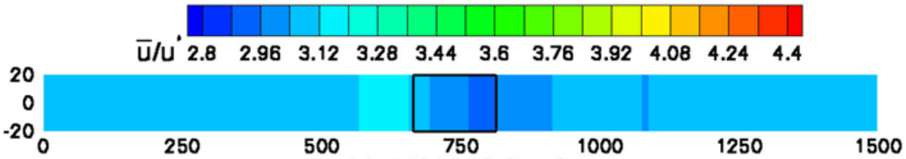

(a) 10% *VOC* strip

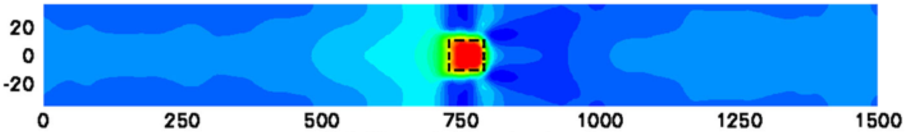

(b) *Case 1* (4 actuators)

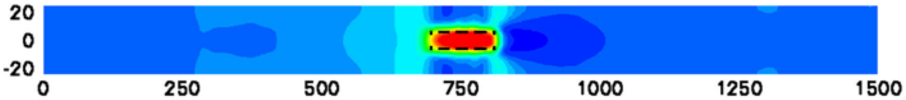

(c) *Case 2* (6 actuators)

Figure 4.36: Time-averaged and span-averaged contours of streamwise velocity at $y = 3.2l^*$ above the surface for: (a) 10% *VOC* strip; (b) *Case 1* (4 actuators) and (c) *Case 2* (6 actuators).

as far as 1.5 slot lengths ahead of the actuator (fig. 4.36(b)). A similar result was seen on figure 4.30 for the 10% *VOC* strip. In this case, the upstream acceleration can be attributed to the local reduction in shear stress provided by the control strip. However, no such acceleration zone was seen on the individual *VOC* actuators of figure 4.33 despite the actuators themselves being clearly identifiable as low shear-stress zones. The explanation lies in the fact that *Case 1* and *Case 2* each contain a row of closely spaced actuators, rather than near-isolated slots. Since the slots are seen as low shear stress regions and cover 50% of span of the control region, accelerating flow over the slots pulls along upstream fluid and its effect extends considerably upstream. By the same reasoning, it would be expected that similar high shear stress areas would form downstream of the actuators as the flow slows down to match the no-slip condition at the wall. Instead, for the wider slot of *Case 1* (fig. 4.36(b)), a narrow band of higher speed flow is present, surrounded by two bubbles of lower speed flow. In contrast, for the narrow slot of *Case 2* (fig. 4.36(c)), a region of low speed fluid measuring about one slot length long by one slot width wide appears downstream of the actuators. These results suggest that there may be a different mechanism for drag reduction over a discrete slot array than over a continuous *VOC* surface.

As noted above, the flow accelerated in the low shear zone over the slots. It is thus possible that, if a large portion of the surface was covered with holes, a net drag reduction might occur simply from the combined effect of replacing portions of the plate with low-shear zones. Of course this gain might be negated by the areas of high shear stress potentially forming upstream and downstream of each hole. Also, turbulent eddies mixing high speed flow into the holes and drawing low speed flow out could cause greatly increased Reynolds shear stress and pressure drag. But if the holes were small, such as in the current simulation, and were actively controlled, a *VOC*-type algorithm might be used to reduce the turbulent momentum exchange and reduce the high shear stress footprints to the point of a net drag reduction. This low shear stress concept appears to be a novel proposal for how to create an array of drag-reducing MEMS devices.

Contours of the time averaged $\overline{v}_{rms}$ averaged down to a single $xy-$plane are shown in figure 4.37 for the 10% *VOC* strip and both actuator cases.

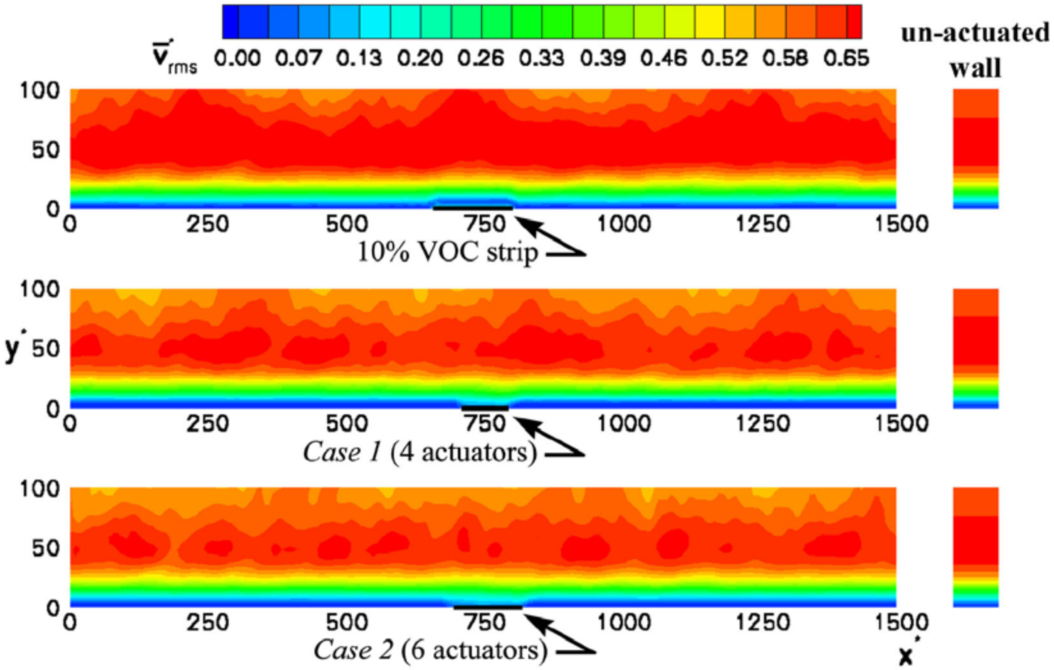

Figure 4.37: Span-averaged and time-averaged contours of v_{rms} on an $xy-$plane for 10% *VOC* strip and multiple actuator cases.

Figure 4.37 shows that unlike the *VOC* strips, a quiet layer of $\overline{v}_{rms}$ does not form over the slots for either discrete actuation case. Instead, the blue layer of reduced fluctuations near the surface is thinner over the slot locations indicating an *increase* in $\overline{v}_{rms}$ over the slot locations. This indicates that, unlike the 10% *VOC* method, discrete actuators are unable to form a localized stagnation plane above the control location. However, the blue layer of low fluctuations near the wall but not directly over the control locations appears thicker for the discrete actuators than for the 10% *VOC* strip. This apparent paradox is explained by further collapsing the data in the $x-$direction onto

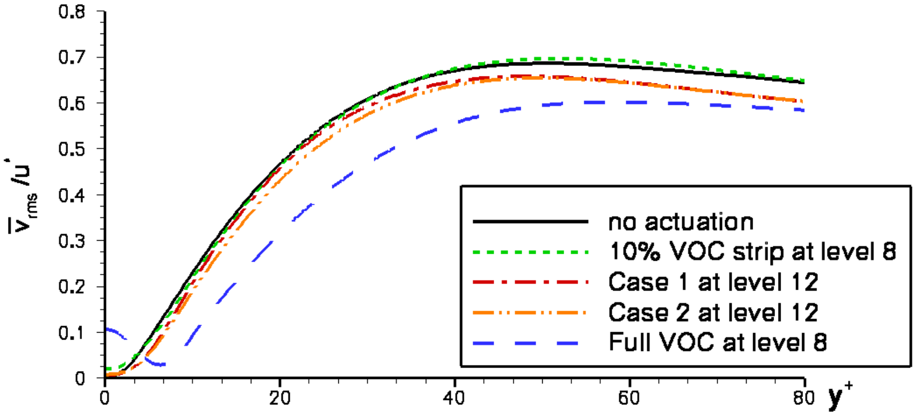

Figure 4.38: Average $\overline{v}_{rms}$ across channel for no actuation, full *VOC*, 10% *VOC* strip and multiple actuator cases.

a single profile across the channel, as seen in figure 4.38. Due to the small coverage area, neither the 10% *VOC* strip nor either multiple actuator case is able to form a stagnation plane similar to the full *VOC*. Instead, all $\overline{v}_{rms}$ profiles closely follow the shape of the un-actuated wall. At the wall, the un-actuated case has, obviously, zero $\overline{v}_{rms}$ due to the no slip boundary condition. The 10% *VOC* strip, however, starts with a non-zero $\overline{v}_{rms}$ at the wall and the profile remains above either *Case 1* or *Case 2* for a height of up to $y^+ \approx 7$. That is, near the wall, $\overline{v}_{rms}$ values are *larger* for the 10% *VOC* strip than for the multiple actuator cases, which translates in the contours of figure 4.37 as a thinner blue layer near the wall. Thus, the apparent quieting of the flow achieved by *Case 1* and *Case 2* with respect to the 10% *VOC* strip is a deceptive result. In the end, as seen in figure 4.38, like the 10% *VOC* strip, neither actuator case is able to form a partial stagnation plane and promote any significant flow control.

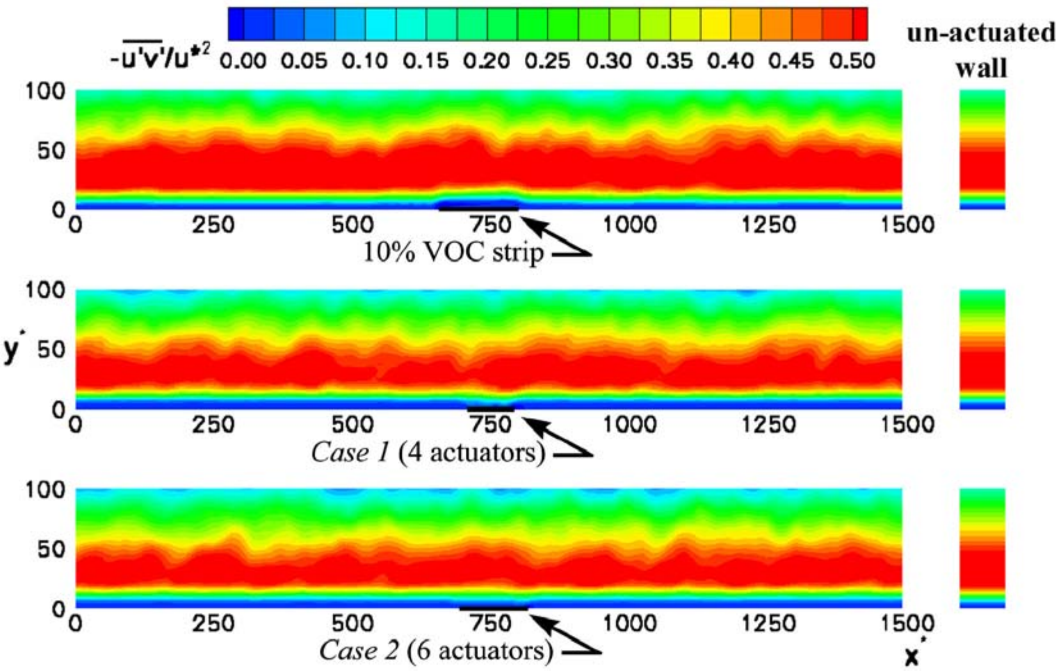

Figure 4.39: Span-averaged and time-averaged contours of Reynolds stress on an $xy-$plane for 10% *VOC* strip and multiple actuator cases.

Average contours of normalized Reynolds stress on an $xy-$plane are shown in figure 4.39. As seen before in figure 4.27, the 10% *VOC* strip has a thicker blue layer of reduced Reynold stresses directly above and extending slightly downstream of the control location. No such thickening of the blue layer is seen above the control location for both *Case 1* and *Case 2* slots. Similar to the $\overline{v}_{rms}$ contours, the near-wall blue layer outside the control location appears thicker for *Case 1* and *Case 2* than for the *VOC* strip and the un-actuated case. However, unlike the results from the $\overline{v}_{rms}$ profile, this near-wall

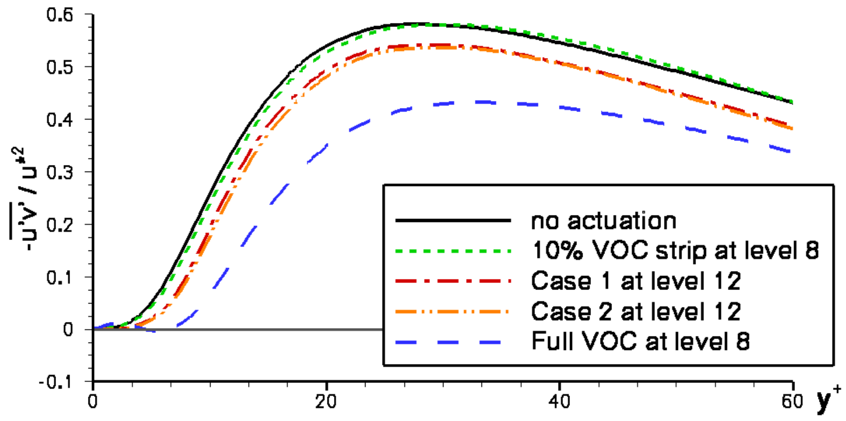

Figure 4.40: Reynolds stress across channel for no actuation, full *VOC*, 10% *VOC* strip and multiple actuator cases.

reduction in $-\overline{u'v'}$ fluctuations is real as proven by the profile of figure 4.40. The normalized $-\overline{u'v'}$ profile of figure 4.40 shows that the 10% *VOC* strip remains close to the un-actuated wall case. However, both *Case 1* and *Case 2* present a noticeable shift in the $-\overline{u'v'}$ profiles away form the wall which, while not as large as the full *VOC*, is more than what was achieved by the 10% *VOC* strip. This result is encouraging in that despite having less than half of the active control area of a 10% *VOC* strip, both of the more realistic actuator rows were able to out-perform the simple numerical *VOC* method in terms of Reynolds stress reductions.

Results on the drag ratio are shown in figure 4.41 as well as running drag averages for all cases. The running drag values show that neither actuator row was able to produce a drag decrease. Instead, averaged drag values with 90% confidence levels show small increases in drag for both *Case 1* and *Case*

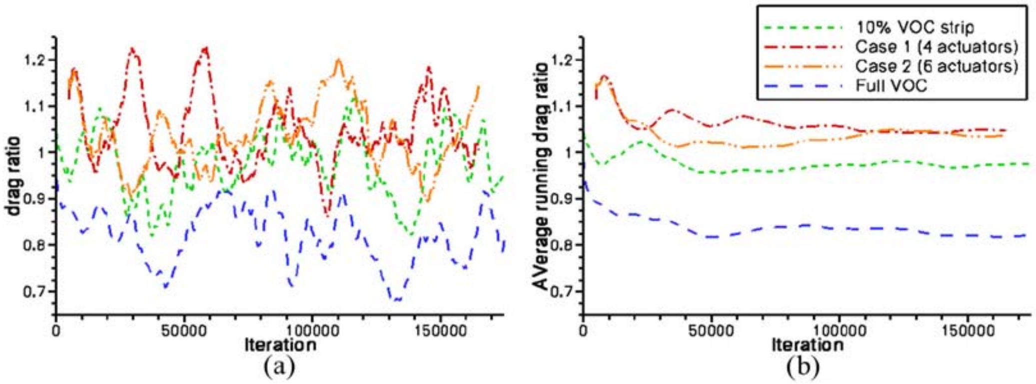

(a) (b)

Figure 4.41: (a) Instantaneous (b) and average running drag ratios for 10% *VOC* strip, *Case 1*, *Case 2* and full *VOC* with respect to the opposing un-actuated boundary.

2. The 4 actuators of *Case 1* had an average *increase* of $4.4\% \pm 2.1\%$ over 22 independent realizations while the 6 actuators of *Case 2* had a $2.6\% \pm 3.6\%$ *increase* over 9 independent realizations. The drag increases for the discrete actuators are in contrast with the $3.1\% \pm 2.4\%$ reduction in drag shown by the 10% *VOC* strip, specially considering the similarity of the $\overline{v}_{rms}$ contours and profile between the strips and slots. The drag increases are also in contrast to the slight reductions in $-\overline{u'v'}$ observed with both rows of discrete actuators throughout the channel. The inability of the actuator rows to reduce drag was likely a result of the small coverage area (3.3% for *Case 1* and 5.0% for *Case 2*) of each actuator row. As for the drag *increase*, it was likely a consequence of the acceleration zone upstream of the actuators. As seen in figure 4.36, high shear stress zones formed upstream of the slots while low shear stress zones formed downstream of the slots. In this case, it appears that the increase in local shear stress ahead of the slots was sufficient to overcome any potential local reductions past their location. Vertical mixing was unlikely to have had much effect on the drag ratio. Unlike the periodic actuation of Section 4.4, the actuator rows used here operated at such low device *Re* that little vorticity is produced from their operation. The contours of figure 4.37 and 4.40 show that fluctuations introduced over the actuator locations are essentially confined to the viscous sublayer. Furthermore, in Section 4.6.1, the full *VOC* method was shown to induce considerable vertical motion at the wall yet there was a substantial drag reduction in that case.

4.7.5 *VOC* Applied to an Array of Actuators

Results from the previous section did not invalidate the approach used in this study but stressed the need for further testing with this type of actuator design and control. If the lack of a drag decrease for single rows of actuators was a result of the small area that could be controlled by the actuators, then increasing the number of rows would be a logical next step. Therefore, two more rows, one upstream and the other downstream of the original row were added to the previous geometry to make up an array of actuators spanning the width but and the length of the domain. The *VOC*-based feedback-control method was kept unchanged so that each new slot had its own individual detection zone and actuation membrane. The geometry of the new configuration matched the one shown in figure 2.7. Unlike the single row domain of figure 4.34, the slots had tapered lips with the wider section at the membrane plane and the narrower section at the top of the plate. This change in geometry was made to ensure that a theoretical membrane deflection would remain inside the slot throat and to conform to more recent experimental studies of Breuer *et al.* [58].

Following the initial designs of *Case 1* and *Case 2*, the higher aspect ratio slot of *Case 2* was chosen as the base actuator unit to form two sets of arrays schematically shown in figure 4.42:

- $5 \times 6 \times 5$ *array* (fig. 4.42(a)) consists of 3 rows of actuators with the first and third rows containing 5 actuators while the middle row contained 6 actuators. The first and third row of actuators were placed so that their slots were aligned with the gaps of the middle row.

- $6 \times 6 \times 6$ *array* (fig. 4.42(b)) consists of 3 rows of actuators containing 6 actuators each. Row placement was such that the slots were aligned directly behind each other.

The control area provided by the $5 \times 6 \times 5$ array corresponded then to 13.3% of the total surface while the $6 \times 6 \times 6$ array covered 15% of the total surface.

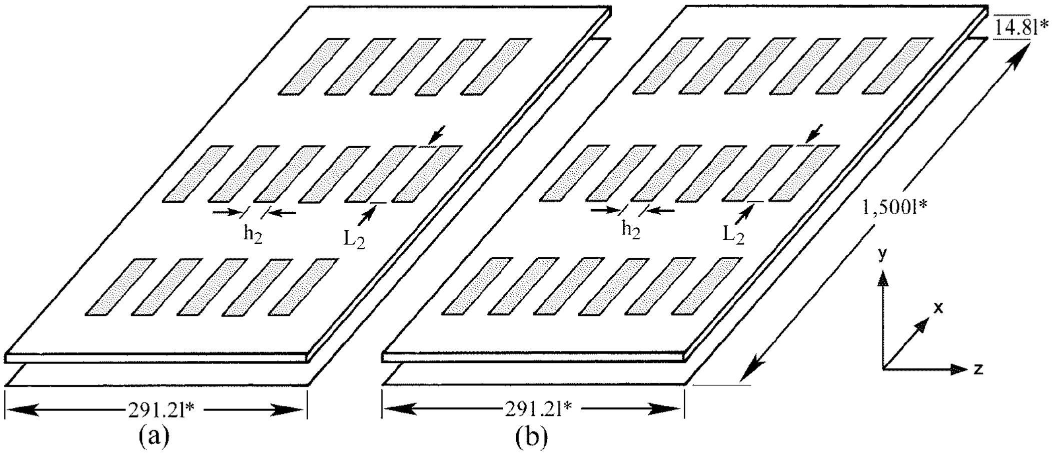

Figure 4.42: Schematic of (a) $5 \times 6 \times 5$ actuator array and (b) $6 \times 6 \times 6$ actuator array.

Figure 4.43 shows contours of time-averaged streamwise velocity on an $xz-$plane at height of $y = 3.6l^*$ above the actuated plate. Each case was averaged over 150,000 time steps or $3,045t^*$. Figure 4.43(b) shows that for the $6 \times 6 \times 6$ array, the streak pattern is similar to the earlier results of figure 4.35. Similar to the single actuator case of Section 4.7.3, there are two low and two high-speed streaks visible on the channel. In contrast, the $5 \times 6 \times 5$ array shown in figure 4.43(a), shows a slightly broken down streak structure throughout the channel with a single pronounced low speed streak at the bottom of the figure and three weaker low speed streaks in the remainder of the domain. For both actuator arrays, low speed streaks were disrupted up to 0.25 slot lengths ahead of each actuator from the flow accelerating over each slot. However, the streaks quickly re-formed downstream of each location.

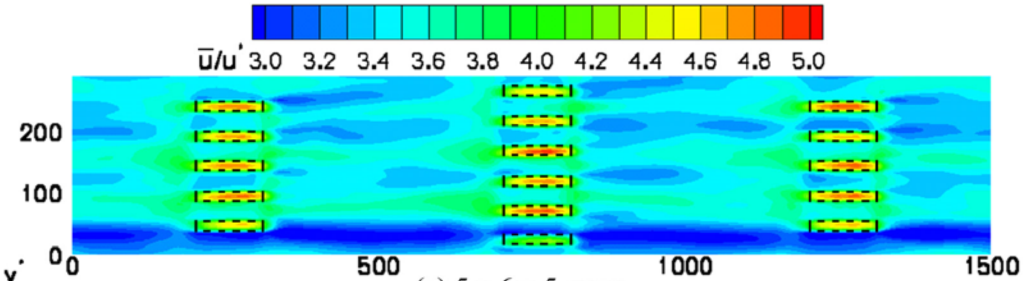

(a) 5 x 6 x 5 array

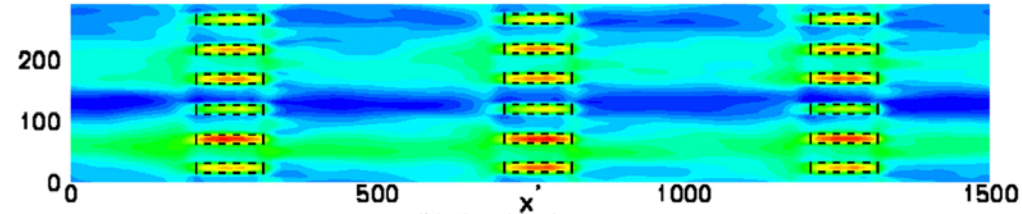

(b) 6 x 6 x 6 array

Figure 4.43: Time-averaged contours of streamwise velocity on an $xz-$plane $3.6l^*$ above the surface for: (a) $5 \times 6 \times 5$ actuator array and (b) $6 \times 6 \times 6$ actuator array.

Data were further span averaged over the centerline of the middle row of actuators and the results are shown as contours of streamwise velocity $3.6l^*$ above the actuated plate in figure 4.44. This allowed for the reduction of data down to a single row of actuators for the $6 \times 6 \times 6$ array. However, since the $5 \times 6 \times 5$ array lacked the same symmetry for the first and third row of actuators, these regions were improperly span-averaged and are marked with a grey box. Only the middle slots then were properly averaged and should be used in a comparative analysis with the $6 \times 6 \times 6$ array. For the $6 \times 6 \times 6$ array (fig. 4.44(b)), the slots have the previously observed upstream region of higher streamwise velocity resulting from accelerating flow over the row of actuators. A close-up of the middle slot shown with streamlines in figure 4.45 shows that the low shear-stress over the slot also causes a slight deflection of the surrounding streamlines towards the slow flow in the center of the slot and away from the gap between actuators. In addition, the slots also have trailing zones of lower streamwise velocity that extend downstream to the acceleration region of the subsequent slot. In particular, the upstream acceleration zone of the center row of figure 4.44(b) is distorted by the low-speed wake of the row preceding it. Similarly, the middle slots of the 5 × 6 × 5 array (fig. 4.44(a)) shows a similar pattern in which their acceleration zone is distorted by the previous row of actuators. Although it may not be possible to entirely suppress the formation of an acceleration zone ahead of an actuator, the above results suggest that their effect may be somewhat controllable with the placement of additional rows of actuators closer together.

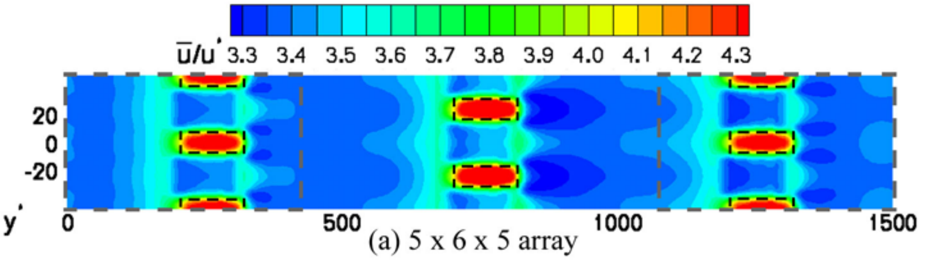

(a) 5 x 6 x 5 array

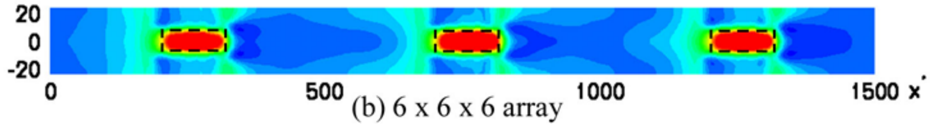

(b) 6 x 6 x 6 array

Figure 4.44: Time and span-averaged contours of streamwise velocity on an $xz-$plane $3.6l^*$ above the surface for: (a) 5×6×5 actuator array and (b) 6×6×6 actuator array. Dashed outline marks regions improperly span-averaged.

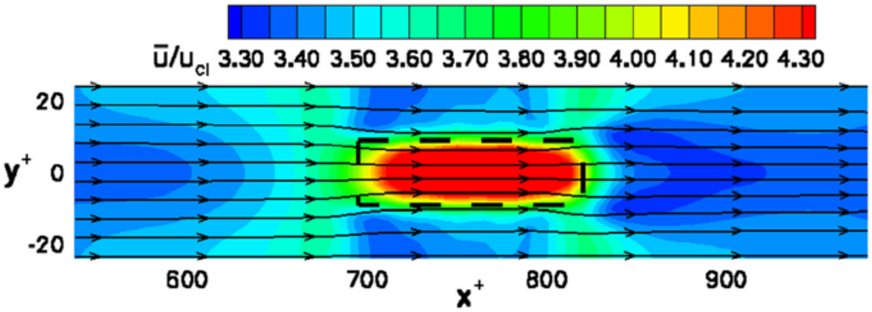

Figure 4.45: Time and span-averaged streamlines over the middle slot of the $6 \times 6 \times 6$ actuator array of figure 4.44(b).

To examine the effects of the actuator arrays across the height of the channel, data were time averaged and span averaged down to a single $xy-$plane. The results are shown in figure 4.46 as normalized contours of $\overline{v}_{rms}$. For comparison purposes, results from the 10% *VOC* strip and un-actuated boundary are also plotted. Similar to the results of figure 4.37 for a single actuator row, figure 4.46 shows a thinning of the blue layer of fluctuations over the location of each row of actuators. Outside of the control region, the height of the blue layer for both arrays of actuators is similar to the un-actuated wall and the 10% *VOC* strip. Fluctuation levels away from the wall ($y^* > 50$) were also similar between both arrays of actuators and the 10% *VOC* strip. The $\overline{v}_{rms}$ profile across the channel are shown in figure 4.47 along with data for the un-actuated plate, 10% strip and full *VOC*. The $\overline{v}_{rms}$ profiles for both the $5 \times 6 \times 5$ and the $6 \times 6 \times 6$ nearly overlap the 10% *VOC* strip. As a result, despite inducing some vertical mixing near the wall, neither actuator array formed a stagnation zone away from the wall. Relative differences between the profiles of both types of actuator arrays were minimal indicating little difference in whether the actuators are spaced aligned or offset. Overall, the performance of the arrays of actuators are similar to the approximately equivalent-sized *VOC* strip, in this case, the 10% strip.

Contours for the normalized Reynolds stress are shown in figure 4.48, again with the 10% strip and un-actuated boundary for comparison purposes. As previously observed with a single row of actuators (figure 4.39), there is no observable reduction in fluctuations over the actuators arrays themselves. Moreover, the relative thickness of both the blue layer in the near-wall region and the red layer in the overlap region are very similar between both actuator arrays and the 10% *VOC* strip. These results are also reflected in the Reynolds stress profiles of figure 4.49. The near wall region below $y^+ \approx 10$ shows a near overlapping of the actuator arrays and the 10% *VOC* strip. The profiles start to diverge slightly within the buffer region with the $6 \times 6 \times 6$ array indicating slightly reduced $-\overline{u'v'}$ fluctuations compared to the $5 \times 6 \times 5$ array.

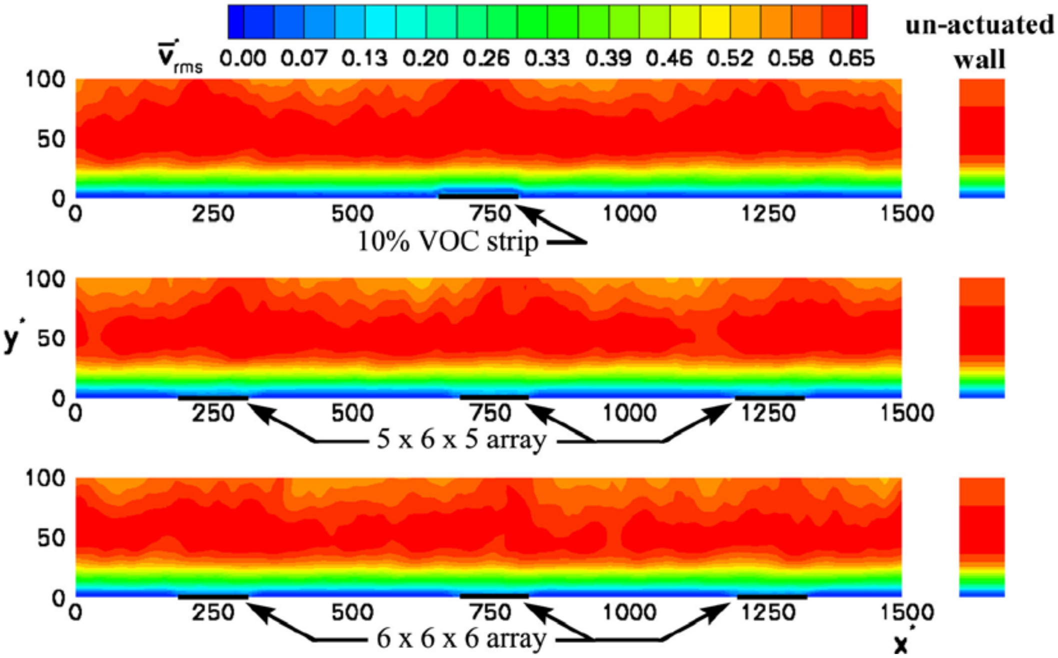

Figure 4.46: Span-averaged and time-averaged contours of v_{rms} on an $xy-$plane for full *VOC* and multiple arrays of actuators.

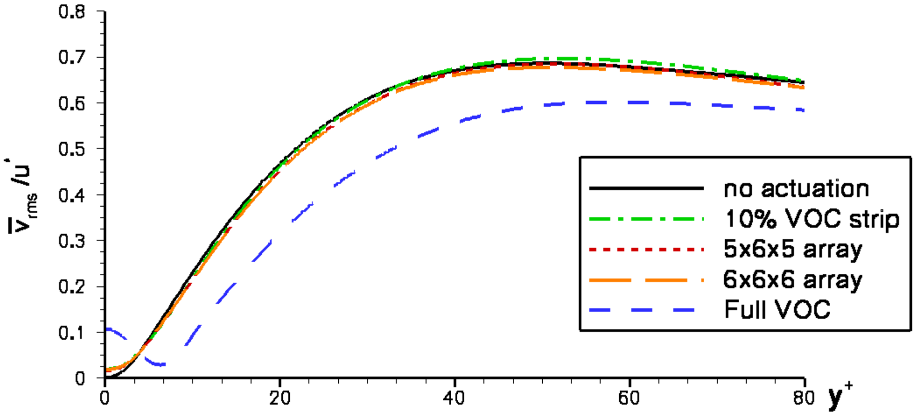

Figure 4.47: Average $\overline{v}_{rms}$ across channel for no actuation, full *VOC*, 10% *VOC* strip and multiple arrays of actuators.

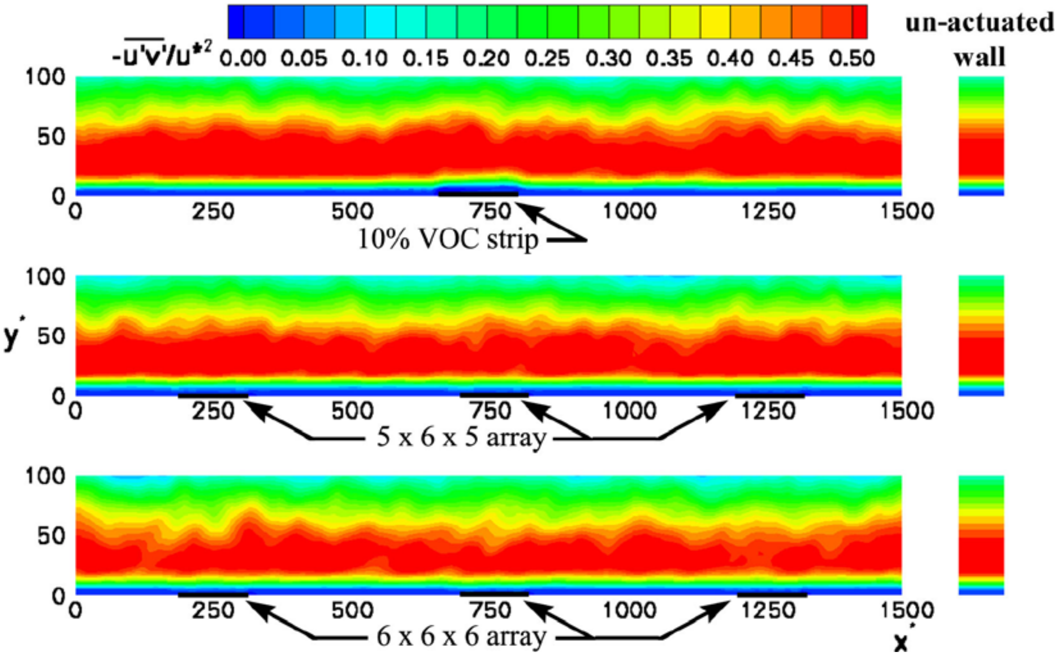

Figure 4.48: Span-averaged and time-averaged contours of Reynolds stress on an $xy-$plane for multiple arrays of actuators and full *VOC*.

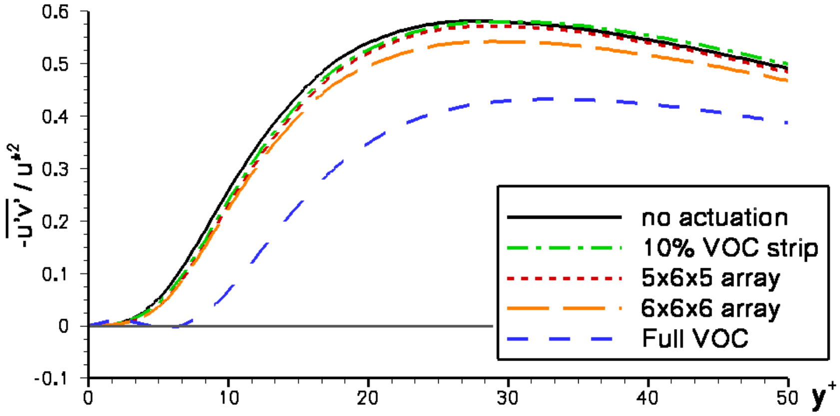

Figure 4.49: Reynolds stress across channel for no actuation, multiple arrays of actuators and full *VOC*.

Results on the instantaneous drag ratio are shown in figure 4.50(a) while the running averages are shown in figure 4.50(b). For comparison purposes, the drag for the full *VOC* method and the 10% *VOC* strip are shown as well. The results show an immediate improvement over the single row of actuators in that neither actuator array resulted in an increase in drag. Data for each array geometry were accumulated to $250,000$ iterations and the results were used to calculate drag averages and error bars with a 90% confidence interval. Both arrays had similar slight drag reduction values: the $5 \times 6 \times 5$ array had a reduction of $4.2\% \pm 1.4\%$ over 29 independent realizations while the $6 \times 6 \times 6$ array had a $4.6\% \pm 1.3\%$ drag reduction over 38 independent realizations. This represented a slight improvement over both the 10% and 30% *VOC* strips which had drag reductions of about 3%. Similar to the small *VOC* strips, this drag reduction was obtained despite the lack of a stagnation plane or substantial reductions of fluctuations within the channel. The relative insensitivity of the drag reductions to the array configurations may be a result of having such small coverage areas (13.3% and 15%). However, this result provides some encouragement in that discrete actuators over a small portion of the total surface area were able to not only provide a drag reduction but also out-perform *VOC* regions with up to twice their coverage area. However, it is also clear that an active control area of up to 15% of the surface was below the critical value necessary to substantially reduce fluctuations and drag.

As noted in the previous section, the low shear zone that develops over the slot locations suggests a different mechanism of drag reduction associated

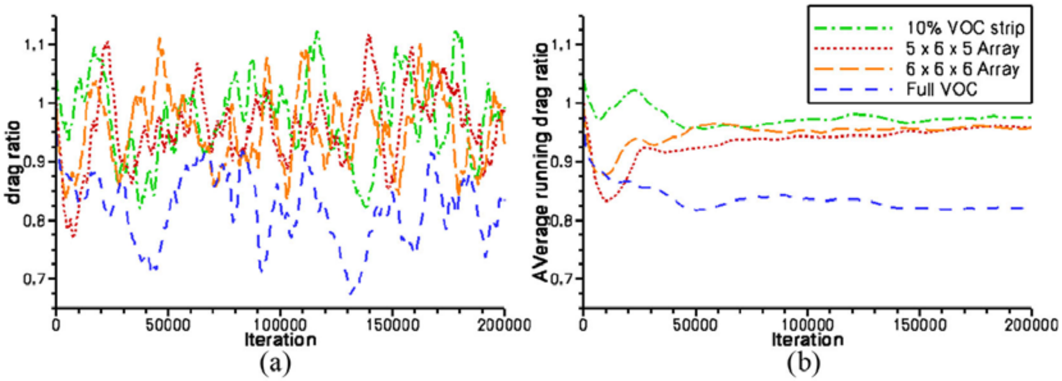

(a) (b)

Figure 4.50: Drag ratios for 10% *VOC* strip and actuator arrays with respect to the un-actuated opposing boundary.

with realistic actuators. Previously, Koumoutsakos *et al.* [26] demonstrated that drag reductions with the *VOC* method and its variants were related to reductions in flow fluctuations and stabilization of the boundary layer. However, the present results for arrays of actuators show a slight drag reduction, of about 4%, despite the apparent lack of such effects. Some explanations can be deduced from the time-averaged and span-averaged plot of the $\overline{u}$-velocity across the length of the channel shown in figure 4.51. Similar to figure 4.30, $\overline{u}$ was sampled at an identical height of $3.6l^*$ above the surface. Figure 4.51 shows that $\overline{u}$ rises significantly over the slots with acceleration zones extending approximately half of a slot length upstream of each row. However, the values of $\overline{u}$, and by extension the shear stress for the active array, consistently lie below the values for the 10% *VOC* strip in the region between actuator rows. To further test the concept of slots acting as low shear zones, simulations were conducted on the inactive 6×6×6 array. The actuation membrane were defined as no slip, stationary surfaces so that the slots behaved like shallow cavities. For this case, a slight drag reduction of 1.9% ± 2.4% was measured over 14 independent realizations in $150,000$ time steps. Time and span-averaged values $\overline{u}$ sampled $3.6l^*$ above the surface for the inactive $6 \times 6 \times 6$ array are also shown in figure 4.51. Similar to previous results, flow accelerates over the slot locations and, as seen in the figure, $\overline{u}$ over the inactive arrays peaks higher than the active slots. While this result may suggest even lower surface drag for the inactive array, it is a deceptive result since $\overline{u}$ values in the region between the slots are higher for the inactive compared to the active arrays. This result can be better understood by noting that the presence of the slots induces a near identical change in mean velocity between the slot and surface regions for the active and inactive cases. Therefore, since the active array has a lower drag associated with the lower $\overline{u}$ on the surface, it also has a lower peak $\overline{u}$ over the slot.

The question of whether cavities may induce decreases in shear stress was indirectly examined by Higdon [59] in 2-D Stokes flow simulations. Higdon [59] calculated the shear stress along a surface and walls of square and rounded cavities. Results showed that that reductions in shear stress occur along the cavity wall. Moreover, negative shear was possible for cavities deep enough to allow the development of a circulation cell. However, the high-viscosity characteristics of Stokes flow resulted in symmetric flow fields and shear stress profiles about the center of the cavities. Although it was not explicitly computed, this result suggested that the overall shear stress along the surface and

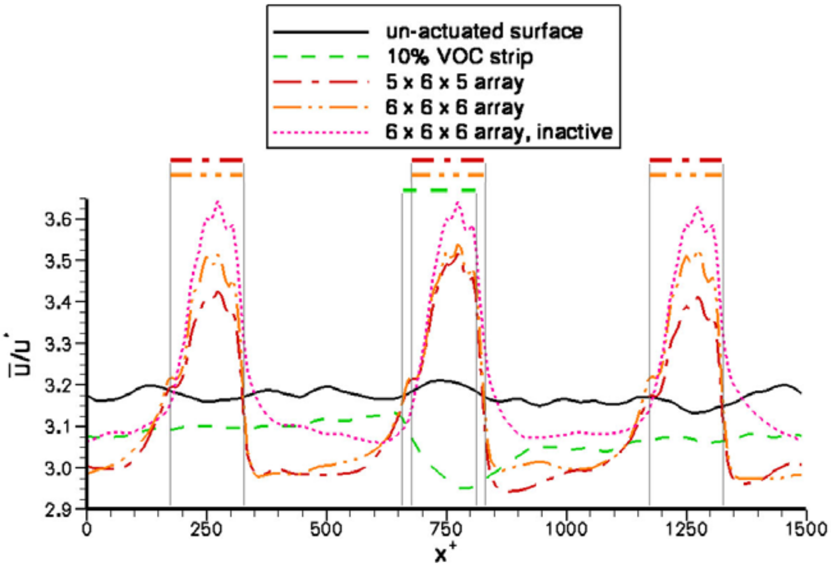

Figure 4.51: Time-averaged and span-averaged streamwise $\overline{u}$-velocity $3.6l^*$ above the surface for an un-actuated surface, 10% VOC strip and $6 \times 6 \times 6$ array.

cavity walls should remain unchanged. This does not, however, invalidate the concept of drag reduction brought about by low shear zones in a full, 3-D Navier-Stokes representation.

To further determine the potential activity of the slots as low shear-stress regions, a separate run was conducted with the inactive $6 \times 6 \times 6$ array geometry in a laminar flow at $Re_{channel}$ of 118. The corresponding slot Reynolds number based on the slot width and the peak streamwise velocity at the slot exit plane was $Re_{slot,lam} = 4.0$. Simulations were allowed to reach a virtually-steady state prior to sampling. Figure 4.52 shows contours of streamwise velocity over a slot on the middle row of actuators. Similar to the turbulent case, an upstream acceleration zone and a downstream deceleration zone of size similar to the slot length develop around the slot. Low speed flow also develops in the gaps between actuators and the streamlines are deflected towards the low shear stress region over the slot and away from the gaps. Additional laminar runs were performed, varying $Re_{channel}$ by a factor of 4 to 29.5 and 472. The corresponding $Re_{slot,lam}$ were then 0.6 and 22, respectively. Results for the span-averaged $\overline{u}$-velocity sampled at a height of $0.1h$ above the surface are shown in figure 4.53 for the arrays and a flat plate. Legends and vertical lines show the location of each row of actuators along the length of the domain. As seen in the figure, $\overline{u}$ rises over the slot locations for all tested laminar runs. Flow accelerates approximately half a slot length ahead of the actuators and decelerates over approximately one slot length downstream before being affected by the subsequent row of actuators. However, unlike the results of Higdon [59], $\overline{u}$ and by extension the shear stress are not symmetrical about the center of each slot. In more detail, starting from the low $Re_{slot,lam}$ of 0.6, the profiles grow increasingly asymmetrical with respect to the center of each slot with increasing Reynolds number. These results suggest that the integrated shear stress value over each slot may differ from a flat surface and may even cause a drag decrease. This was indeed the case: extended runs on the $Re_{slot,lam} = 4.0$ slot showed an asymptotic decrease on the drag ratio to 1.2% – a reduction that could only be attributed to the low-shear stress effect of the slots.

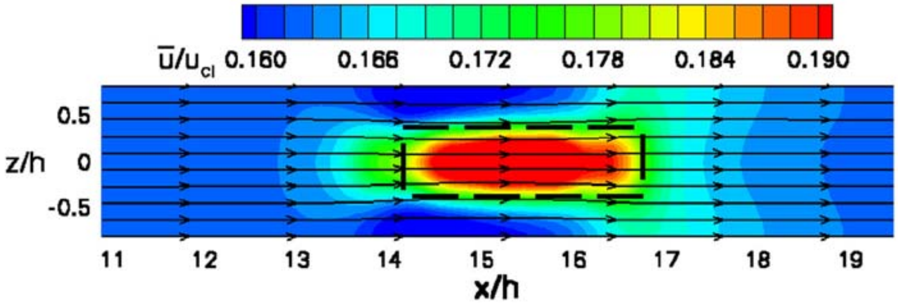

Figure 4.52: Streamwise velocity and streamlines at $0.1h$ above the plate over a slot in laminar flow for 3 different channel Reynolds number.

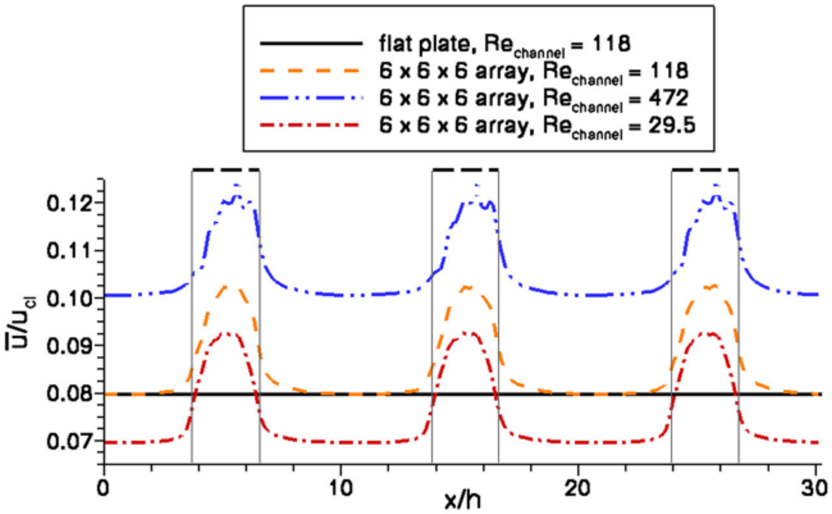

Figure 4.53: Time averaged and span averaged streamwise $\overline{u}$-velocity $y = 0.1h$ above the surface for flat plate and $6 \times 6 \times 6$ array in laminar flow.

Chapter 5

Conclusions

5.1 Introduction

The primary objective of this study was to apply the flexibility of numerical methods to investigate in detail the physics and capabilities of a discrete actuator for active flow control. The study was performed along a series of logical steps as outlined in the flowchart of figure 1.5 at the end of Chapter 1. The main results of this study are summarized over the following sections with a comprehensive list of results presented at the end.

5.2 Numerical Method

The numerical method chosen was initially developed by Kim *et al.* [6] to examine turbulent channel flow. Variations of this numerical method have been used in several other turbulent channel flow studies. The particular modified version in this study included the use of a force field method to drive the flow and to emulate the behavior of moderately complex geometries and moving surfaces within the domain. The force field method had been previously shown to accurately replicate solid boundaries and surface textures ([33], [32], [52]). However, this method had not been previously used to simulate the internal geometry of a synthetic jet. For 2-D simulations, the force field method was used to simulate a separating wall and a driving surface that would actuate the flow in a piston-like manner. In the case of full 3-D simulations, the force field method was used to create a raised plate with slot jets cut into it and sub-surface structures containing the driving mechanism. Eventually, the 3-D slot jets were constructed with actuating surfaces mounted at the bottom of the raised plate while maintaining a sub-surface gap to provide fluid for the slots. In the 3-D simulations, the magnitude of the velocity imposed along the driver surfaces was shaped with a sine-surface function to better represent a membrane motion.

5.2.1 Validation Issues

The numerical method was first tested in a 2-D domain simulating a partial internal structure and driving mechanism similar to a real synthetic jet. Runs were conducted on different grid sizes and the results were compared to other numerical studies and experimental data to establish their accuracy. Time convergence was maintained by selecting time steps within dictated stability parameters ([52], [54]) and monitoring the CFL number. The results were in good agreement with other numerical studies [47], [45], [46]), despite having a domain that was periodic and considerably narrower. Validation against experimental data ([42]) was only possible in the region near the jet exit due to the 2-D nature of the simulation. Experimentally, even high aspect ratio slot jets had strong 3-D effects that caused the quick breakdown of the synthetic jet into a standard turbulent jet within a few slot widths of the jet exit. Despite this limitation, results of the 2-D simulation were in good agreement with experimental data in the region near the slots.

Time convergence in the 3-D simulations was ensured in the same manner as the 2-D simulations. However, no strict grid convergence studies were performed on the 3-D grid. Instead, the grid resolution was kept at values that matched or surpassed those of previous numerical studies in which such resolution had been proved to be accurate. Thus grid spacing in the streamwise and spanwise direction and the critical direction cell Reynolds number were less than or at most equal to the values in other studies ([6], [25]). In the normal direction, convergence was ensured by mounting all geometries at or below the 12^{th} plane from the bottom of the domain. Previous numerical studies with the same simulation method ([32], [33]) had previously demonstrated convergence for geometries created by the virtual force method placed at heights of up to 15 levels. Convergence of the flow around the slots was ensured by using similar grid spacings to the 2-D study. Since the flow phenomena of interest to the 3-D study were restricted to the buffer layer, the previous near slot validation of the 2-D code was considered suitable here as well.

5.3 Summary of Results

5.3.1 2-D Slot Jets

Experimental studies at moderate to high device Reynolds numbers ([36]) showed that ejected fluid rolled up into a pair of counter-rotating vortices upon leaving the cavity. Continuous operation of the synthetic jets resulted in the quick breakdown of the jet structure within a few slot widths of the exit orifice so that the averaged jet structure behaved similar to a turbulent steady jet. Other detailed numerical studies ([47]) also showed that stable circulation cells tended to form within the pumping cavity under periodic actuation.

This study expanded on those previous results by further conducting parametric studies on flow and geometric properties. Variations in Reynolds number were achieved through changes in viscosity while the Strouhal number was modified by varying the period of actuation. At very low Re_{jet}, fluid ejected in the blowing cycles was unable to form an actual jet before dissipating. The high viscosity also prevented the formation of circulation cells within the cavity. At moderate Re_{jet}, the results were similar to [47] but with a distinct vortex pairing feature. Over time, continuous merging of ejected vortex pairs was established at a distance of approximately $x/h = 55$ from the aperture. At high Re_{jet}, individual pairing events were observed but there was no discernible pattern due to the complexity of the flow field. The low viscosity and closed nature of the domain allowed vortices to remain coherent even after impacting against the far boundary. In addition, the cavity flow did not form a stable circulation cell throughout the extent of the runs examined. The chaotic cavity flow occasionally caused blobs of internal vorticity to be ejected with the fluid, producing vortex pairs with increased translational speed and further affecting pairing events. Variations in device Strouhal number St_{jet} also produced variations in pairing events. Low St_{jet} resulted in long periods of actuation and vortex pairs spaced far apart so that no pairing events were observed. High St_{jet} resulted in the opposite effect with continuous vortex merging very near the exit plane into a vortex sheet.

Of the many geometric parameters available, two were chosen: domain size and lip thickness and shape. Due to the closed definition of the domain, studies had to be conducted on its potential effets on the resulting jets. Conversely, lip thickness and shape are experimental design considerations that also impact on the resulting jet. The jets were found to be very insensitive to the size of the external domain unless it was made to be as shallow as the cavity. Decreasing the size of the cavity produced two results: suppression of the circulation cell and changes to the translational speed of ejected vortices as more internal vorticity was ejected at each pulse. Increasing the lip thickness was also found to increase the translational speed of the resulting vortex. As boundary layers developed in the throat region, a constricting effect was produced that effectively made the slot width narrower than the actual size. However, shaped lips with sharp, pointed edges presented no such thickness effect probably due to the fact that flow separated on the sharp lips in a manner similar to the baseline geometry.

5.3.2 3-D Slot Jets

Slot jets were mounted aligned with the turbulent flow down a channel and determined to not substantially impact the flow when non-operational. Initial runs were performed in the absence of channel flow and the jet structure was found to conform to the 2-D results along the centerline of the slot. The 3-D structure of the jet was similar to [47] but with distorted edges on the blowing jet structure. This distortion was a result of the sub-surface design chosen for the actuators which promoted additional outflow near the edges of the slot.

The jets were combined with a channel flow and pulsed under quasi-steady actuation with a weak jet strength. Flow from the slots was found to create substantial vorticity as part of the sudden start process but vorticity production tapered off as the jets remained under steady operation. Different pulsing arrangements were capable of changing the streak pattern over the plate. These results conformed to the expectations that fluid injection at the surface, even by discrete actuators, would be able to alter the streak pattern ([11]). Furthermore, numerical experiments demonstrated that flow control could be obtained by manipulating the vorticity flux at the wall ([26]). Thus, if properly calibrated and timed, vorticity off the slots from the startup condition might be able of achieving some form of flow control.

Periodic pulsing applied by the slots at moderate to high jet strengths produced a constant injection of vorticity at each blowing pulse. Vorticity generated from the blowing jet structure was rolled into hairpin vortices by shearing of the mean flow. Drag increases were measured for this case due to increased mixing and destabilization of the wall layer from the pulsing jets. However, the results suggested that proper calibration of the strength of actuation and, by extension, the production of wall vorticity, could promote flow control.

5.3.3 Targeted Pulses and Hybrid Surfaces

Targeted pulses were tested by identifying particular flow structures and issuing single pulses from one or more slots so that the resulting hairpin could interact with the target. Two cases were tested. The first case attempted to disrupt a streamwise vortex by pulsing a single slot ahead of the target and allowing the approaching target vortex and blowing hairpin to merge. The second case involved pulsing two adjacent actuators underneath a high shear stress zone in an attempt to cancel it or lift it away from the surface. In both cases, the pulses eliminated the target structure but as the hairpins rose and dissipated, they spawned more vortical structures larger or on the same scale as the original target structures. Consequently, no drag reduction was observed.

Passive structures were combined with the slots in an attempt to reorganize the flow prior to actuation. Riblets of height $14.6l^*$ placed $100l^*$ apart were able to isolate surface structures between them, with occasional high shear structures sliding over the crests. Placing riblets closer together ($50l^*$ apart) lifted all high shear structures away from the wall and onto the riblet crests. Actuation from a slot next to the riblet was affected by the Coanda effect so that the resulting hairpin shifted in the spanwise direction, straddling the riblet. Despite this result, hairpins from moderate to high strength were unable to remove the high shear stress crest structures. Consequently, no drag reduction was obtained as well.

5.3.4 3-D Control Algorithms

Although of interest, the hairpin structure generated by moderate to strong jets was not effective in achieving useful flow control. Therefore, a different approach was chosen in which the strength of actuation was to be calibrated with a feed-back method. The chosen method was the *VOC* previously used in [25] and [26]. Prior to adapting the method to work with discrete actuators, a few parametric studies were conducted with the current numerical method.

A modified version of the *VOC* method was tested with a single plate placed at locations varying from level 12 to 6 while the detection plane was kept at approximately $10l^*$ above the plate. Results were on par with [25] but with less of a drag reduction. This was likely due to *VOC* being applied to only one of the walls of the domain and the lower R^* of the present simulation. The results, however, were useful for later baseline comparisons. The *VOC* method worked by creating a stagnation plane at a distance approximately halfway between the active surface and the detection plane. The stagnation plane represented the region in which flow fluctuations in the vertical direction were balanced by the suction/blowing off the wall. The reduction in fluctuations at the stagnation plane extended both towards the plate and into the mean flow leading to an overall quieting down of the flow.

The *VOC* method was also tested when applied to portions of the plate.

This was also done for later baseline comparisons since discrete actuators were unable to replicate the uniform coverage of the full *VOC* method. The *VOC* strips spanned the width of the domain but varied in length in the streamwise direction. Test cases were run with strips covering 10%, 30%, 60% and 80% of the domain. As the size of the control region increased, mean flow properties showed a shift from the un-actuated plate values to the full *VOC*. Substantial reductions in flow fluctuations and overall drag were observed when a clear stagnation plane began to form – between 30% and 60% coverage area.

5.3.5 3-D Control Algorithms Applied to Discrete Actuators

The *VOC* method was applied to discrete actuators by calculating the average normal velocity over an area of equal size to the slot and immediately above it at a height of approximately $10l^*$. While variations on the size and location of the detection zone were possible, they were not investigated as part of this study.

Initial studies were applied to a single active slot in order to determine the performance characteristics of the *VOC* method applied to a discrete actuator. Two configurations were tested: a narrow slot of length similar to a streamwise vortex and a wide slot of width similar to a streamwise vortex. Results showed that the slots behaved as a low-shear zones, allowing flow to accelerate over it. The slots were found to have downstream zones of influence measuring approximately 2.5 slot lengths long and a slot width to either side of the centerline. This result provided crucial information for the design of an array of actuators.

Based on the results of the single actuator slots, two configurations of a discrete control strip were were tested. The design of each configuration took into consideration the area of influence of each slot. Slots were then evenly spaced $1h$ apart spanning the width of the domain. – *Case 1* consisted of 4 wide actuators and – *Case 2* had 6 narrow actuators. The corresponding area actively controlled by the actuators corresponded to 3.3% and 5.0% of the total surface area, respectively. Results showed that, since each slot still behaved as a low-shear region, the combined area over the row of actuators allowed incoming flow to accelerate ahead of it. Downstream of the actuators, low speed zones of a size similar to the slots were observed for the narrow slots. A similar but less pronounced effect was observed for the wide actuators.

Further studies were performed with additional rows of narrow slots since this geometry seemed more suitable for flow control than the wide slots. Two additional rows were placed for a total of 3 rows of actuators in two configurations: one with the slots aligned with each other in a $6 \times 6 \times 6$ array and the other with the slots offset in a $5 \times 6 \times 5$ array. The corresponding active area controlled by the actuators were then 15% and 13.3% of the total area of the surface, respectively. Time averaged results show that neither actuator array was able to form a mean stagnation plane to dampen vertical flow fluctuations like the *VOC* studies. Consequently, there was no substantial reduction in fluctuations near the surface or into the mean flow and the velocity and vorticity profiles near the wall resembled those of an un-actuated surface.

However the additional rows caused further disruptions in the streak patterns near the actuated surface. In particular, the offset $5 \times 6 \times 5$ array was able to effectively breakdown long persistent streaks into scattered elements. Despite a lack of dampening fluctuations in the flow, both arrays were found to induce slight drag reductions of around 4% – more than similarly-sized 10% and 30% *VOC* strips.

5.4 Results and Discussion

The following list summarizes the main findings of this study:

- New application of spectral-DNS and force field method to moderately complex boundaries such as the internal driving mechanism of a synthetic jet.
- Accurate representation of the jet velocity and vorticity at the exit plane for a 2-D synthetic jet requires definition of the internal driving mechanism and throat area.
- Geometric parameters such as thickness and shape of the throat area and the cavity shape and depth can substantially affect the resulting synthetic jet.
- Pulsing adjacent jets in close proximity results in flow from blowing slots being drawn towards neighboring suctioning slots.

- Periodic blowing pulses are sheared by the mean channel flow to form hairpin vortices.

- Streamwise riblets spanning the length of the domain and placed $50l^*$ apart lift high shear stress elements from the surface and onto the riblet crests.

- Single pulses from slots placed adjacent to a streamwise riblet were shifted in the spanwise direction towards the riblet so that the resulting hairpin straddles the riblet.

- Despite the potential to alter structures in the boundary layer, hairpins from single blowing pulses introduce too much mixing to provide a drag reduction.

- The *VOC* method as defined in [25] requires a substantial portion of the surface (as much as 60%) to be activelly-controlled to provide a substantial drag reduction.

- Flow from a single, *VOC*-controlled slot is too weak to form an actual synthetic jet. The result is more of a mild pushing and tugging of the local flow.

- Single, actively-controlled slots behave as regions of reduced shear stress, allowing the flow to accelerate over them.

- A nearly-isolated active slot contains a downstream region of influence approximately 2.5 slot lengths long and 1 slot width wide to either side of the centerline.

- A row of actively-controlled slots allow flow to accelerate upstream from the combined area of reduced shear stress. Decreases in shear stress are present downstream of the actuators.

- Arrays of actively-controlled slots can provide a slight drag reduction that is superior to *VOC* strips of area equivalent to the total coverage area provided by the actuators.

- Drag reduction from an array of actuators seems to occur due to the net combined effect of the slots behaving as shallow cavities of reduced shear stress. The drag reductions were obtained despite of a lack of a substantial impact on the boundary layer structures.

Table 5.1 summarizes the effects on drag of the most relevant simulations conducted in this study. As described in Section 2.5 and applied throughout this study, the calculated drag ratio between the top boundary and the actuated surfaces may not be completely independent. However, as calcuated here, the drag ratio is still useful in determining the relative effect of a particular configuration with respect to the opposing un-actuated surface.

The drag reduction mechanism based on slots behaving as low-shear stress regions was further tested by leaving the actuator arrays inactive. Results for turbulent flow, as seen in Table 5.1, show a slight reduction for the

Table 5.1: Average drag reductions for different simulations.

Geometry	Ind. Realizations	Average Drag Reduction
4 slots, periodic actuation "-++-" mode	18	16.1% ± 2.0% increase
4 slots, periodic actuation "-+-+" mode	7	16.0% ± 5.0% increase
single tilted pulse	1	2.0% increase
strong pulse	1	1.2% increase
10% *VOC* strip	15	3.1% ± 2.4%
30% *VOC* strip	24	3.2% ± 2.3%
60% *VOC* strip	24	12% ± 1.8%
80% *VOC* strip	11	13% ± 3.2%
full *VOC*	13	18% ± 2.6%
4 actuator row	22	4.4% ± 2.1% increase
6 actuator row	9	2.6% ± 3.6% increase
$5 \times 6 \times 5$ array	29	4.2% ± 1.4%
$6 \times 6 \times 6$ array	38	4.6% ± 1.3%
$6 \times 6 \times 6$ array, inactive	14	1.9% ± 2.4%
$6 \times 6 \times 6$ array, laminar	NA	1.2%, $Re_{slot,lam} = 4.0$

$6 \times 6 \times 6$ array. Laminar runs with the inactive $6 \times 6 \times 6$ slot array also resulted in a definite but small drag reduction. Assuming that the drag reduction is indeed real, the laminar results indicated that the slots can reduce drag from their low-shear stress effect. However, the same could not be said for turbulent flow: flow mixing and interaction with the inactive slot geometry and the substantial acceleration and deceleration zones of influence created by the slots likely negated any potential gains. However, the small adjustment provided by each slot through the *VOC* method seemed to provide enough near-wall control to make the laminar low-shear stress zone concept work in turbulent flow.

5.5 Future Work

Much work can still be done with the numerical method and concepts mentioned here. As designed and used in this study, the arrays of actuators performed slightly better than equivalent-sized *VOC* strip. It was also suggested that the drag reduction mechanism associated with discrete actuators may be different than with the *VOC* method. In addition, the present study did not calculated the amount of power spent in the operation of the devices. Therefore, despite the small global reduction in drag, there are no current estimates on the net power savings of the actuators. Based on these conclusions, the following future studies are proposed:

Parametric studies on the actuators

Results indicated that further benefit may be reaped from the current configuration by simply increasing the amount of area covered by the actuators. Figure 5.1 shows the drag reduction (and increase) resulting from the application of the modified *VOC* method and *VOC* method applied to discrete actuators. For the modified *VOC* strip, the increase in drag reduction seems to be progressive as the strip sizes increased towards the full *VOC* case. Discrete actuators show slightly improved drag decreases with respect to the 10% and 30% *VOC* strips. However, it is also clear that there is insufficient data to draw any further conclusions regarding the efficiency of discrete actuators with respect to the amount of actively-controlled area. Consequently, further studies should be conducted in which the number of actuators would be gradually increased by adding additional rows of actuators. Results could establish whether the drag reduction with discrete actuators increases proportionally with coverage area towards the full *VOC* case or has a lower assymptotic limit. Results would also help determine an optimum coverage area of actuators beyond which increased coverage area would yield negligible improvement in drag reduction.

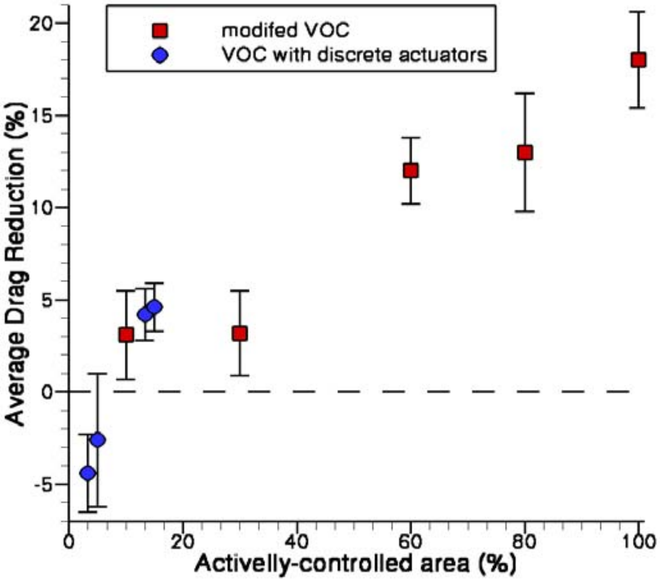

Figure 5.1: Average drag reductions (positive) and increases (negative) vs. coverage area for modified *VOC* method and *VOC* method applied to discrete actuators.

Another parameter to examine would be the size of the actuators. The slots used in the actuator array had a width of $24.3l^*$, considerably larger than initially proposed in the experiments of [50] and used earlier in Sections 4.1 through 4.5. Smaller actuators scattered over the surface can benefit from being more similar to an actual *VOC* distribution. Conversely, large actuators placed together would seem to benefit the low-shear region concept by clustering such zones together. In addition, more studies could be performed on the particular placement of individual actuators.

Results for the $5 \times 6 \times 5$ and $6 \times 6 \times 6$ arrays showed no particular differences between the configurations. Looking back, the particular placement of the slots may not have been important with only 3 rows of actuators and coverage areas of O(10%). However, additional arrays placed closer together should indicate some effect. Aligning slots head-to-tail would cause the downstream zone of influence of a preceding slot to be within the upstream zone of influence of the following one. Aligning slots offset would minimize this effect so that rows of actuators could be mounted even close together and still remain somewhat uncorrelated to each other.

Lastly, the power spent operating one individual slot should be calculated and extended to the array of actuators. This will allow the determinarion of whether the slot jets can induce net power savings in addtition to global reductions in drag.

Changes to *VOC* Detection

Another parametric issue of importance relates to the detection of flow properties for the feed-back loop. The present discrete actuators used an average normal velocity, $\overline{v}$, over a detection area of equal size to the slot and directly above it. The area averaging of velocity meant that both the detected property and the type of actuation performed by the discrete actuators were significantly different from the original *VOC* concept. This is illustrated in figure 5.2, which plots both the mean detected velocity and the velocity trace at a single gridpoint at the center of the detection area. For the velocity traces shown in the figure, mean detected velocities were of $O(0.1u^*)$ while pointwise velocity fluctuations were of $O(0.3u^*)$. As noted in Section 4.7.3, the dampening effect of area averaging is such that values of $\overline{v}$ decrease as the size of the detection area increases. Therefore, there might be an upper limit to the size of the detection region beyond which $\overline{v}$ values might be too low and/or uncorrelated with respect to flow fluctuations, thus negating the premise of the *VOC* method. Conversely, an overly small detection region might input $\overline{v}$ values that exceed the performance characteristics of the devices and numerical method, which would lead to erroneous results from the *VOC* method and numerical instabilities. In addition to size, the location of the detection region is another issue that could be addressed in future works. In this study, the detection regions were kept directly above the actuators. Given the size of the slots and the height of the detection region, flow structures were unlikely to convect beyond the area of effect of the actuators in either the streamwise or spanwise directions. However, flow convection may become a factor if smaller actuators or smaller detection regions are used. In this case, additional transfer functions similar to [50] would be needed. Those transfer functions would have to account for both the translation and evolution of the flow between the detected region and the actuation location.

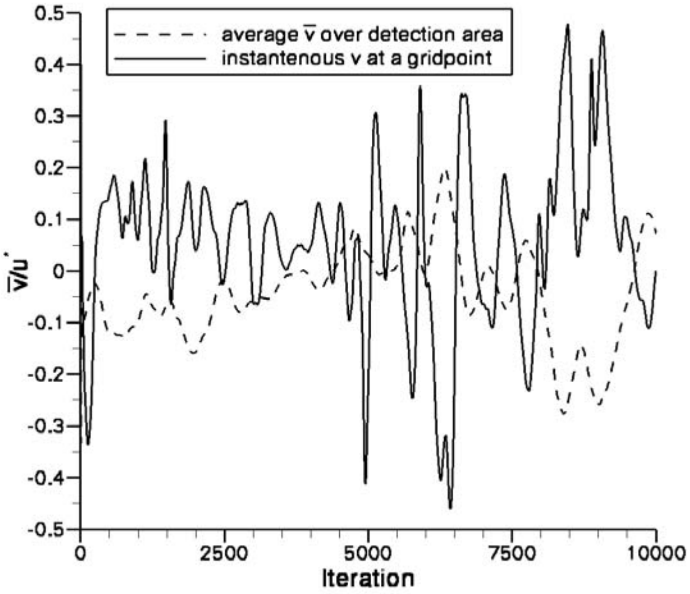

Figure 5.2: Trace of average velocity over the detection area of one slot and the instantaneous velocity at a single gridpoint at the center of the detection area.

While the size and location of the detection region above the surface may be worthwhile parameters to examine, the issue still remains that such sensing method is unfeasible with realistic actuators. In reality, external flow properties are seldom known without intrusive (i.e. probes) or non-practical detection methods (i.e. LDA). Therefore, realistic feed-back controlled devices must rely on detection of wall properties for their control loops. Surface-based detection has been tested numerically ([26]) and experimentally ([50], [24]) with positive results. These studies made use of transform functions to relate wall-measurable quantities such as pressure and shear stress to a certain strength of actuation. These transformation functions could be adapted to the current numerical method to simulate wall sensing. In this case, wall properties could be taken as the values one gridpoint away from the surface. Similarly, wall gradients may be measured directly from the difference between values at the wall and at one gridpoint away from it. Wall sensing may require extensive parametric studies on the location, size and number of sensors. Luckily, studies conducted so far have already provided considerable insight on this issues. For example, [24] determined the optimum location of wall mounted shear-stress sensors to be at the same streamwise location as the actuators.

Based on the above suggestions for future work, the bottom part of the flowchart of figure 1.5 in Chapter 1 is further expanded and shown in figure 5.3. The proposed future work fits within the body of work accumulated so far. It is the expectation that these additional steps may result in the final goal of manipulating fine-scale flow structures and achieving efficient and practical drag reduction.

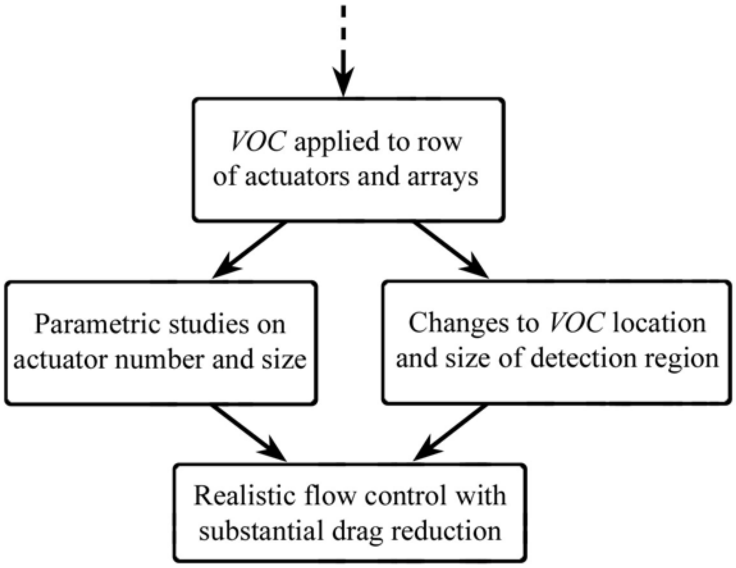

Figure 5.3: Proposed future work on this area.

Bibliography

[1] A.L. Braslow. A history of suction-type laminar-flow control with emphasis on flight testing. Monographs in Aerospace History 13, NASA History Division, Office of Policy and Plans, Washington, D.C., 1999.

[2] E. Coustols and A.M. Savill. Turbulent skin-friction drag reduction by active and passive means. In *Special Course on Skin-Friction Drag Reduction*, AGARD report 768, pages 8–1–8–55. Advisory Group for Aerospace Research and Development, 1992.

[3] S.J. Kline. A brief history of boundary layer structure research. In Ronald L. Panton, editor, *Self-Sustaining Mechanisms of Wall Turbulence*. Computational Mechanics Publications, 1997.

[4] C.R. Smith and J.D.A. Walker. Sustaning mechanisms of turbulent boundary layers: The role of vortex development and interactions. In Ronald L. Panton, editor, *Self-Sustaining Mechanisms of Wall Turbulence*. Computational Mechanics Publications, 1997.

[5] A.K. Praturi and R.S. Brodkey. A stereoscopic visual study of coherent structures i nturbulent shear flow. *Journal of Fluid Mechanics*, 89:251–273, 1978.

[6] J. Kim, P. Moin, and R. Moser. Turbulent statistics in fully developed channel flow at low reynolds number. *Journal of Fluid Mechanics*, 177:133–166, 1987.

[7] P.H. Alfredsson and A.V. Johansson. On the detection of turbulence-generating events. *Journal of Fluid Mechanics*, 139:325–345, 1984.

[8] J. Jiménez and A. Pinelli. Flow autonomous cycle of near-wall turbulence. *Journal of Fluid Mechanics*, 389:335–359, 1999.

[9] F. Wallefe. On a self-sustaining process in shear flows. *Physics of Fluids*, 9:883–900, 1997.

[10] J. Jiménez and M. P. Simens. Low-dimensional dynamics of a turbulent wall flow. *Journal of Fluid Mechanics*, 435:81–91, 2001.

[11] M. Gad-el-Hak. Flow control: the future. *Journal of Aircraft*, 38(3):402–418, 2001.

[12] R.A. Antonia, L. Fulachier, L.V. Krishnamoorthy, T. Benavid, and F. Anselmet. Influence of wall suction on the organized motion in a turbulent boundary layer. *Journal of Fluid Mechanics*, 190:217–240, 1988.

[13] M. Elena. Suction effects on turbulence statistics in a heated pipe flow. *Physics of Fluids*, 27(4):861–866, 1984.

[14] K. Kim, H.J. Sung, and M.K. Chung. Assesment of local blowing and suction in a turbulent boundary layer. *AIAA Journal*, 40(1):175–177, 2002.

[15] P. Bradshaw and N. Pontikos. Measurements in a turbulent boundary layer on an infinite swept wing. *Journal of Fluid Mechanics*, 159:105–130, 1985.

[16] P. Moin, T.-H. Shih, D. Driver, and N.N. Mansour. Direct numerical simulation of a three-dimensional turbulent boundary layer. *Physics of Fluids*, A2(1):1846–1853, 1990.

[17] F. Laadhari, L. Skandaji, and R. Morel. Turbulence reduction in a boundary layer by a local spanwise oscillating surface. *Physics of Fluids*, 6(10):3218–3220, 1994.

[18] S.M. Trujillo. *An Investigation of the Effects of Spanwise Wall Oscillation on the Structure of a Turbulent Boundary Layer*. PhD thesis, The University of Texas at Austin, Austin, TX, August 1999.

[19] Y. Du and G.E. Karniadakis. Supressing wall turbulence by means of a transverse travelling wave. *Science*, 288:1230–1234, 2000.

[20] O.K. Rediniotis, D. Lagoudas, R. Mani, L. Traub, R. Allen, and G. Karniadakis. Compuational and experimental studies of an active skin for turbulent drag reduction. Paper AIAA 2002-2830, 1^{st} Flow Control Conference, St. Louis, MO, June 2002.

[21] C. Lee, J. Kim, D. Babcock, and R. Goodman. Application of neural networks to turbulence control for drag reduction. *Physics of Fluids*, 9:1740–1747, 1997.

[22] C. Lee, J. Kim, and H. Choi. Suboptimal control of turbulent channel flow for turbulent drag reduction. *Journal of Fluid Mechanics*, 358:245–258, 1998.

[23] R. Rathnasingham and K. Breuer. System identification and control of a turbulent boundary layer. *Physics of Fluids*, 9:1867–1869, 1997.

[24] K. Amonlirdviman and K.S. Breuer. Linear predictive filtering in a numerically simulated turbulent flow. *Physics of Fluids*, 12(12):3221–3228, 2003.

[25] H. Choi, P. Moin, and J. Kim. Active turbulence control for drag reduction in wall-bounded flows. *Journal of Fluid Mechanics*, 262:75–110, 1994.

[26] P. Koumoutsakos, P. Bewley, E.P. Hammond, and P. Moin. Feedback algorithms for turbulence control - some recent developments. Paper AIAA 97-200, *28th* Fluid Dynamics Conference, Snowmass Village, CO, June 1997.

[27] C.K. Liu, S.J. Kline, and J.P. Johnston. An experimental study of turbulent boundary layers on rough walls. Report MD-15, Thermosciences Division, Mechanical Engineering Department, Stanford University, Stanford, CA, 1966.

[28] M.J. Walsh. Viscous drag reduction in boundary layers. *Progress in Astronautics and Aeronautics*, 363:203–259, 1990.

[29] D.W. Berchert, M. Bruse, W. Hage, J.G.T. van der Hoeven, and G. Hoppe. Experiments on drag-reducing surfaces and their optimization with an adjustable geometry. *Journal of Fluid Mechanics*, 338:59–87, 1997.

[30] K.-S. Choi. Near-wall structure of turbulent boundary layer with riblets. *Journal of Fluid Mechanics*, 208:417–458, 1989.

[31] H. Choi, P. Moin, and J. Kim. Direct numerical simulation of turbulent flow over riblets. *Journal of Fluid Mechanics*, 225:503–539, 1993.

[32] D.B. Goldstein and T.-C. Tuan. Secondary flow induced by riblets. *Journal of Fluid Mechanics*, 363:115–151, 1998.

[33] D.B. Goldstein, H. Handler, and L. Sirovich. Direct numerical simulation of turbulent flow over a modeled riblet covered surface. *Journal of Fluid Mechanics*, 302:333–376, 1995.

[34] F. Sherman, S. Tung, C.J. Kim, C.-M. Ho, and J. Woo. Flow control using high-aspect-ratio in-plane microactuators. *Sensors and Actuators*, 73:169–175, 1999.

[35] C.L. Liu, J.-B. Huang, A.Z. Zhu, F. Jiang, S. Tung abd Y.-C. Tai, and C.-M. Ho. A micromachined flow shear stress sensor based on thermal transfer principles. *Journal of MEMS*, 8(1):90–99, 1999.

[36] B.L. Smith and A. Glezer. The formation and evolution of synthetic jets. *Physics of Fluids*, 10(9):2281–2297, 1998.

[37] D. Smith, D. Amitay, M. Kibens, V. Parekh, and A. Glezer. Modification of lifting body aerodynamics using synthetic jet actuators. Paper AIAA 98-0209, *36th* Aerospace Sciences Meeting and Exhibit, Reno, NV, January 1998.

[38] A. Crook, A.M. Sadri, and N.J. Wood. The development and implementation of synthetic jets for the control of separated flow. Paper AIAA 99-3176, *17th* Applied Aerodynamics Conference, Norfolk, VA, June 1999.

[39] O.K. Rediniotis, J. Ko, X. Yue, and A.J. Kurdila. Synthetic jets, their reduced order modeling and applications to flow control. Paper AIAA 99-1000, *37th* AIAA Aerospace Sciences Meeting and Exhibit, Reno, NV, January 1999.

[40] F.J. Chen and G.B. Beeler. Virtual shaping of a two-dimensional naca 0015 airfoil using synthetic jet actuator. Paper AIAA 2002-3273, *1st* AIAA Flow Control Conference, St. Louis, MO, June 2002.

[41] F.S. Henry D.J. Peake and H.H. Pearcey. Viscous flow control with air-jet vortex generators. Paper AIAA 99-3175, *17th* AIAA Applied Aerodynamics Conference, Norfolk, VA, June 1999.

[42] B.L. Smith, M.A. Trautman, and A. Glezer. Controlled interactions of adjacent synthetic jets. Paper AIAA 99-0669, *37th* Aerospace Sciences Meeting and Exhibit, Reno, NV, January 1999.

[43] S.G. Mallinson, G. Hong, and J.A. Reizes. Some characteristics of synthetic jets. Paper AIAA 99-3651, *30th* AIAA Fluid Dynamics Conference, Norfolk, VA, June 1999.

[44] N.W. Schaeffler. The interaction of a synthetic jet and a turbulent boundary layer. Paper AIAA 2003-0643, *41st* AIAA Aerospace Sciences Meeting and Exhibit, Reno, NV, January 2003.

[45] L.D. Kral, J.F. Donovan, A.B. Cain, and A.W. Cary. Numerical simulation of synthetic jet actuators. Paper AIAA 97-1824, *28th* Fluid Dynamics Conference, Norfolk, VA, June 1997.

[46] D. Guo, L.D. Kral, and A.W. Cary. Numerical simulation of the interaction of adjacent synthetic jet actuators. Paper AIAA 2000-2565, *31th* Fluid Dynamics Conference, Denver, CO, June 2000.

[47] D.P. Rizzetta, M.R. Visbal, and M.J. Stanek. Numerical investigation of synthetic jet flowfields. *AIAA Journal*, 37(8):919–927, 1999.

[48] S. Tardu. Active control of near-wall turbulence by local oscillating blowing. *Journal of Fluid Mechanics*, 439:217–253, 2001.

[49] S.A. Jacobson and W.C. Reynolds. Active control of streamwise vortices and streaks in boundary layers. *Journal of Fluid Mechanics*, 360:179–211, 1998.

[50] R. Rathnasingham. *System Identification and Active Control of a Turbulent Boundary Layer*. PhD thesis, Massachusetts Institute of Technology, Cambridge, MA, June 1997.

[51] C.S. Peskin. Flow patterns around heart valves: A numerical method. *Journal of Computational Physics*, 10:252–271, 1972.

[52] D.B. Goldstein, H. Handler, and L. Sirovich. Modeling a no-slip boundary with an external force field. *Journal of Computational Physics*, 105:354–366, 1995.

[53] E.M. Saiki and S. Biringen. Numerical simulation of a cylinder in uniform flow: Application of a virtual bondary method. *Journal of Computational Physics*, 123:450–465, 1996.

[54] C. Lee. Stability characteristics of the virtual boundary method in three-dimensional applications. *Journal of Computational Physics*, 184:559–591, 2003.

[55] E.A. Fadlun, R. Verzicco, P. Orlandi, and J. Mohd-Yusof. Combined immersed-boundary finite-difference methods for three-dimensional complex flow simulations. *Journal of Computational Physics*, 161:35–60, 2000.

[56] J. Kim, D. Kim, and H. Choi. An immersed-boundary finite-volume method for simulations of flow in complex geometries. *Journal of Computational Physics*, 171:132–150, 2001.

[57] L.D. Kral and D. Guo. Characterization of jet actuators for active control. Paper AIAA 99-3573, *30th* Fluid Dynamics Conference, Norfolk, VA, June 1999.

[58] K.S. Breuer, J. Bae, and C.S. Tan. Active control of tip clearance flow in axial compressots. Paper GT2003-38661, Proceedings of ASME Turbo Expo 2003 - Power of Land Sea and Air, Atlanta, GA, June 2003.

[59] J.J.L. Higdon. Stokes flow in arbitrary two-dimensional domains: shear flow over ridges and cavities. *Journal of Fluid Mechanics*, 159:195–226, 1985.

Index

Vita

Conrad Yuan Yuen Lee was born in Porto Alegre, in the state of Rio Grande do Sul, Brazil on 23 April, 1973. The son of Chi Zen Lee and Suzy Tse Lee, he received a B.S. degree in Aerospace Engineering from the Virginia Polytechnic Institue - Virginia Tech in 1994. He entered the Aerospace Engineering and Engineering Mechanics department at The University of Texas at Austin in 1995 and received a M.S. degree in Engineering in 1997.

Permanent address: 7201 Wood Hollow Dr. 419
Austin, Texas 78731

This dissertation was typeset with LaTeX[†] by the author.

[†] LaTeX is a document preparation system developed by Leslie Lamport as a special version of Donald Knuth's TeX Program.